High-throughput imaging platform for 3-dimensional cell cultures using light-sheet microscopy

Ph.D. Thesis

Ákos Diósdi

Supervisor:
Péter Horváth, PhD, DSc

Doctoral School of Biology
Faculty of Science and Informatics, University of Szeged

Department of Biochemistry, HUN-REN Biological Research Centre, Szeged

Szeged

2025

1. Publications

MTMT ID: 10071366

The graduation procedure is based on the following publications:

Diosdi, A., Hirling, D., Kovacs, M., Toth, T., Harmati, M., Koos, K., Buzas, K., Piccinini, F., Horvath, P. (2021) A quantitative metric for the comparative evaluation of optical clearing protocols for 3D multicellular spheroids. Computational and Structural Biotechnology Journal 19, 1233-1243

IF: 6.155

Diosdi, A., Hirling, D., Kovacs, M., Toth, T., Harmati, M., Koos, K., Buzas, K., Piccinini, F., & Horvath, P. (2021) Cell lines and clearing approaches: a single-cell level 3D light-sheet fluorescence microscopy dataset of multicellular spheroids. Data in Brief 36, 107090

IF: 1.200

Grexa, I., Diosdi, A., Harmati, M., Kriston, A., Moshkov, N., Buzas, K., ... & Horvath, P. (2021). SpheroidPicker for automated 3D cell culture manipulation using deep learning. Scientific Reports, 11(1), 14813.

IF: 4.997

Diosdi, A., Toth, T., Harmati, M., Grexa, I., Schrettner, B., Hapek, N., Kovacs, F., Kriston, A., Buzas, K., Pampaloni, F., Piccinini, F., & Horváth, P. (2025) HCS-3DX: a next-generation AI-driven automated 3D-oid high-content screening system. Nature Communications.

IF: 15.700

Other publications related to the subject of this thesis:

Hollandi, R., Diósdi, Á., Hollandi, G., Moshkov, N., & Horváth, P. (2020). AnnotatorJ: an ImageJ plugin to ease hand annotation of cellular compartments. Molecular biology of the cell, 31(20), 2179-2186.

IF: 4.138

Piccinini, F., Balassa, T., Carbonaro, A., Diosdi, A., Toth, T., Moshkov, N., ... & Horvath, P. (2020). Software tools for 3D nuclei segmentation and quantitative

analysis in multicellular aggregates. Computational and structural biotechnology journal, 18, 1287-1300.

IF: 7.271

Tasnadi, E. A., Toth, T., Kovacs, M., Diosdi, A., Pampaloni, F., Molnar, J., ... & Horvath, P. (2020). 3D-Cell-Annotator: an open-source active surface tool for single-cell segmentation in 3D microscopy images. Bioinformatics, 36(9), 2948-2949.

IF: 6.937

Peirsman, A., Blondeel, E., Ahmed, T., Anckaert, J., Audenaert, D., Boterberg, T., ... Diosdi, A., ... & De Wever, O. (2021). MISpheroID: a knowledgebase and transparency tool for minimum information in spheroid identity. Nature methods, 18(11), 1294-1303.

IF: 47.990

Pietiäinen, V., Polso, M., Migh, E., Guckelsberger, C., Harmati, M., Diosdi, A., ... & Hepojoki, J. (2023). Image-based and machine learning-guided multiplexed serology test for SARS-CoV-2. Cell Reports Methods, 3(8).

IF: 3.900

Diosdi, A., Piccinini, F., Boroczky, T., Dobra, G., Castellani, G., Buzas, K., Horvath, P., & Harmati, M. (2025) Single-cell light-sheet fluorescence 3D images of tumour-stroma spheroid multicultures. Sci Data 12, 492.

IF: 5.800

Blondeel, E., Ernst, S., De Vuyst, F., Diósdi, Á., … & De Wever, O. (2025) Sequential orthogonal assays for longitudinal and endpoint characterization of three-dimensional spheroids. Nat Protoc.

IF: 13.100

Hollandi, R., Bauer, D., Diosdi, A., Schrettner, B., Toth, T., Hirling, D., Hollandi, G., Harmati, M., Molnár, J., & Horváth, P. (2024) When the pen is mightier than the sword: semi-automatic 2 and 3D image labelling. bioRxiv 2024.01.15.575658;

IF: not applicable

Cumulative IF: 117.188

Patents:

Diósdi, Á., & Horváth, P. (2022). Lemezösszeállítás minták gyors, automatikus, nagy behatolási mélységgel való vizsgálatára light-sheet mikroszkóppal (Hungarian Utility Model No. U2200088). Hungarian Intellectual Property Office.

Diósdi, Á., & Horváth, P. (2022). Plate assembly for rapid, automatic, high penetration depth examination of samples with a light-sheet microscope, and procedure for its application (Hungarian Patent Application No. P2200213). Hungarian Intellectual Property Office.

Table of contents

2. List of abbreviations

2D – Two-dimension(al)
3D – Three-dimension(al)
AI – Artificial Intelligence
ATCC – American Type Culture Collection
BABB – Benzyl alcohol/benzyl benzoate
CTCF – Corrected total cell fluorescence
DAPI – 4′,6-diamidino-2-phenylindole
DL – Deep learning
DMEM – Dulbecco's Modified Eagle Medium
DMEM/F12 – 1:1 mixture of DMEM and Ham's F-12 medium
DMEM HG – DMEM high glucose concentration (25 mM)
DMEM LG – DMEM low glucose concentration (5.6 mM)
DNN – deep neural network
DPBS – Dulbecco's Phosphate Buffered Saline (DPBS)
DSLM – Digital scanned laser light fluorescence microscope
ECACC – European Collection of Authenticated Cell Cultures
ECM – Extracellular matrix
EMEM – Eagle's Minimum Essential Medium
EthD-1 – Ethidium homodimer-1
FBS – Fetal Bovine Serum
GFP – Green Fluorescent Protein
GPU – Graphics processing unit
GUI – Graphical user interface
HE – Hematoxylin-eosin
LSFM – Light-sheet fluorescence microscopy
MEM – Minimal Essential Medium
Min – Minutes
MIP – Maximum Intensity Projection
MLP – Multilayer perceptron
MRC-5 – Medical Research Council cell strain 5
NCI – National Cancer Institute
P/S/A – Penicillin-Streptomycin-Amphotericin
PBS – Phosphate Buffered Saline
PFA – Paraformaldehyde
RI – Refractive index
RPMI1640 – Roswell Park Memorial Institute 1640
SDS – Sodium dodecyl sulfate
SeeDB – See Deep Brain
SNR – Signal-to-noise ratio
SNB – Signal-to-background ratio
SPIM – Selective plane illumination microscope
SQM – Spheroid Quality Measurement
TOC – Tissue optical clearing
TME – Tumour microenvironment

3. Introduction

3.1. 3D cell cultures

Traditional two-dimensional (2D) monolayer cell culture methods permit cells to grow only on flat surfaces, such as glass or polystyrene dishes where cells are adherent to each other and can spread into a single layer [1]. The use of 2D cell cultures in biology has helped to decrease the usage of laboratory animals whilst ensuring the rapid development of research and the discovery of new pharmaceuticals and medicines [2]. Indeed, the 2D cell culture techniques are cost-effective, easy to observe, and most importantly highly reproducible and compatible with automation (Table 1). Therefore, such models are broadly used in biological research because of their optimal high-throughput capabilities in drug testing [3]. However, 2D models have several limitations because they are unable to perfectly replicate physiological conditions and natural microenvironment, including the structure, biological signals of live tissues, and interactions between cells and the matrix [4], [5]. In fact, cell development, proliferation, and function are controlled by communication between cells and their extracellular matrix (ECM), which is lacking in two dimensions [6]. Also, 2D cell culture systems have been forced to alter a number of complex biological processes, including anti-apoptosis and cell proliferation [7], [8], transcriptional regulation, receptor expression, cell invasion, and apoptosis [9-11]. Nevertheless, one of the most significant drawbacks of the 2D models is the lack of capability to form 3D structures, therefore, they do not reflect the physiological features of the tumour microenvironment (TME) [12]. Furthermore, neither the tumour stromal heterogeneity nor the tumour-ECM components can be accurately simulated by these *in vitro* models. Additionally, the heterogeneous distributions and penetration of nutrients, oxygen, and signalling molecules within tissues cannot be replicated in homogenous conditions [13]. Despite these disadvantages, 2D monolayer cell cultures remain necessary for various areas of research including but not limited to cell biology, cancer and toxicity studies, and genetic research.

Over the past decade, there has been a remarkable increase in the number of potential anti-cancer agents being advanced for development. However, merely 10% of these agents are progressing through successfully in clinical development. The two main reasons for drug failures during development are insufficient clinical efficacy and/or

unacceptable toxicity [14]. Considering the substantial costs of drug approval and the high failure rates of oncology drugs during clinical testing, it is essential to identify and eliminate potentially inadequate compounds as early as possible. Ideally, this elimination should occur before clinical trials and, if possible, even before animal testing [15]. The limitations of 2D cell cultures highlight the need for more sophisticated and robust models in order to obtain relevant biological information on drug testing, cellular behaviour, and disease mechanisms.

3D cell culture models, the so-called “-oids” (e.g. spheroids, organoids, tumouroids, and assembloids), have captured the spotlight lately, as they provide an *in vivo* environment where cells can interact in 3D [16]. It is generally believed that 3D cell culture models can be a better approach to understand certain biological processes because cells growing in a 3D environment can give insight into complex biological processes.

In comparison to monolayer cell cultures, 3D cell culture systems allow cells to grow in all directions and provide cell-to-cell and cell-to-matrix interactions with the presence of ECM components. Therefore, 3D cell cultures are an *in vitro* reconstruction of the ECM and cells arranged in specific positions. In this way, the model retains the ECM's mechanical, geometric, and biological characteristics, whilst the morphology and cellular organisation shaped by the interactions of ECM and cells can then be studied [17]. Because of this, 3D models of *in vitro* tumours are crucial research instruments for examining the processes underlying cancer spread and growth [18-20]. This 3D environment allows for a more realistic modelling of organs and tissues. Although nutrients, oxygen, and pH are not equally distributed among the cells in a 3D environment, the multilayer structure allows more realistic penetration studies [21]. 2D cell cultures cannot maintain their natural morphology, therefore, they are more sensitive to the effects of drugs than 3D models. Multiple publications have claimed that 3D cell cultures show higher resistance to drugs and radiation than 2D cell cultures [3], [5], [22-24]. Such studies are essential for understanding tumour progression, drug resistance, metastasis, and the effectiveness of cancer treatments. Nevertheless, 3D models aid in the reduction of drug failure rates in clinical trials, the reduction of animal models, and the identification of more appropriate therapeutic targets.

Over the last few decades, many 3D-oid models have been established, each characterised by its unique functional complexity and shape (Fig. 1). To distinguish these models, each 3D cell culture was named accordingly:

- Multicellular aggregates are one of the simplest 3D cell culture models where cell clusters are free from a defined structural obligation. Easy to form, however, the lack of structural and functional complexity limits their potential [25], [26].

- Spheroid models are a special type of multicellular aggregates where cells are grouped in a nearly spherical shape. These commonly used models are perfect for validation since the symmetrical morphology allows us to estimate 3D features even from a 2D image. Furthermore, they provide the opportunity to examine the necrotic core formation and various penetration properties [25], [27].

- Tumouroids are spheroids composed of cancer cells [28].

- Co- and Tri-culture spheroids or multicellular spheroids refer to spheroids composed of multiple cell lines that do not accomplish a specific function together. They are often used to generate a more complex tumour model to understand the interaction between different cell lines in 3D [29], [30].

- Microtissue models are multicellular aggregates where multiple cell lines work together to accomplish specific functions [31].

- Organoids are self-renewing multicellular aggregates that mimic the structure and function of real organs. Stem and progenitor cells of an organoid can self-renew and differentiate into various cell types, and self-organise into *ex vivo* mini-organs [32], [33].

- Assembloids are self-organising 3D cultures formed by combining an organoid with an additional cell line or combining 2 or more distinctly patterned organoids together [34], [35]. Assembloid models are generally good for investigating the

interactions between different tissues that could give rise to new cellular properties.

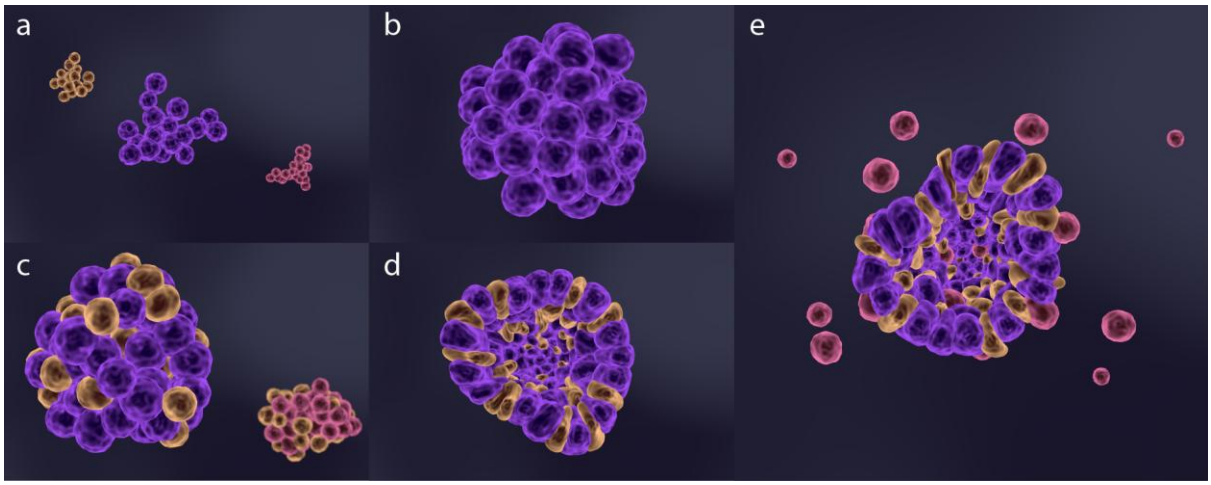

Figure 1. Representative images of 3D-oids illustrating various cellular organization models and highlighting their structural and functional diversity. (a) Cell aggregates with a loose structure, representing an early-stage assembly with non-uniform organization. (b) Spheroid culture derived from tumour cells exhibits a compact and structured form, characteristic of in vitro tumour modelling. (c) Co-culture spheroid integrates multiple cell types within a 3D environment, facilitating complex cellular interactions. (d) Organoid model replicates the architecture and functionality of actual organs, serving as an advanced tissue model. (e) An assembloid model consisting of an organoid combined with an additional cell culture introduced at a later stage, demonstrating multi-layered integration and cellular development.

Nowadays, generating and selecting the appropriate 3D cell culture model is not particularly difficult and there are many relevant but diverse methods for this purpose. However, selecting the perfect method for engineering such a model requires an understanding of the main principles. In particular, the nature of the cells (the selected, isolated, appropriate strain cell line, primary cells, and tissue origin), complexity (monoculture or multiculture), size (smaller for microscopy or bigger diameter for necrotic core formation), the microenvironment in which they are grown (scaffold free or imitation of ECM), type of the scaffold-based biomaterials (natural, synthetic, or hard), additional usage of signalling molecules (proteins and growth factors), and culturing time [5]. In general, the growing methods can be divided into scaffold based or scaffold-free methods.

Scaffold based methods involve the growth of the cells in the presence of a hard polymer material or hydrogel-based support, which can be either natural or synthetic,

either from plants or animals. Natural scaffolds, such as collagen, gelatine, fibrin, and hyaluronic acid, offer biocompatible support, whilst synthetic scaffolds, made from materials like polylactic acid, polyglycolic acid, and polycaprolactone, can be engineered for specific properties like controlled degradation and mechanical strength. These scaffolds in general provide an advantageous microenvironment for cells to grow. For instance, hydrogels have the primary benefit of having physico-chemical properties, making them a suitable substitute for the mechanical and biochemical characteristics of the real native extracellular matrix [36]. In a hydrogel environment cells have a hydrated network creating a large surface area to allow the adhesion, growth, proliferation, and movement of the cells, whilst this porous structure provides a better exchange of gas and nutrients. Furthermore, a relatively new tissue engineering technology called 3D bioprinting relies on the same hydrogel support as a bioink for precisely growing 3D models [37], [38]. However, scaffold based methods face numerous challenges: (1) identification of biodegradable and biomimetic supports; (2) maintaining long-term functionality and viability; (3) reproducibility; (4) expensive materials; (5) extensive handling and specific equipment; (6) automation [5], [39].

On the other hand, growing 3D models can be as a self-assembly process which is a natural phenomenon that occurs during embryogenesis, organogenesis and morphogenesis. One of the least complicated approaches to grow 3D cell cultures is the scaffold-free method. In this case, there is no scaffolding or fastening surface allowing cells to self-assemble and form aggregates of non-adherent 3D microtissues [40-43]. Whilst scaffold-free methods provide a less natural microenvironment for the cells to grow, these methods are designed to generate spheroids and organoids in high quantities [44].

Due to the simple and inexpensive applications and the spherical shape that provides even penetration, spheroid models have been widely used [42], [44]. Despite being less complex than an organoid model, tumour spheroids have numerous applications because they closely mimic the characteristics of solid tumours in various ways. When spheroids reach a certain size, they exhibit metabolic gradients and closely resemble non-vascularized or weakly vascularized tumours. An exterior layer of proliferating cells, a middle layer of quiescent cells, and an inner layer of hypoxic and necrotic cells make up the multilayered structure [45]. Tumour spheroids have characteristics that show radiation and anti-cancer treatment resistance, as shown in human cancers [45],

[46]. However, more and more studies are demonstrating the opposite effect to a particular drug component where spheroids are more sensitive [47], [48]. Tumour spheroids can be mixed with various cell types, which is a convenient method in the context of drug screening, as it can help to promote migration in tumours and reconstruct the heterogeneous multi-cellular environment for solid tumours [49]. By developing co-culture spheroids, the interactions between tumour cells and peripheral multicellular environments can be modelled. Furthermore, spheroid co-cultures can be employed for drug screening studies since normal host cells near tumour cells can affect the drug sensitivity of tumour cells. In the field of regenerative medicine, genetically modified spheroids have been developed for cell transplantation therapy [50].

Although spheroid models have many advantages, certain drawbacks need to be emphasised. First of all, the spherical shape has advantages, however, high variability can be seen in diameter and size when hundreds of spheroids are produced with the same condition [16]. In addition, large spheroids (>150 μm) can be difficult to observe using confocal microscopy, primarily because of limited light and antibody penetration and light scattering-induced fluorescent signal attenuation. Whilst smaller spheroids tend to be fragile and require special fixation [51]. Therefore, spheroids are typically sectioned or enzymatically broken down into single cell solutions and observed under a bright field microscope in order to calculate the total number of cells. Nevertheless, this approach cannot be used for endpoint analysis that needs viable, intact spheroids. A non-destructive high-content screening (HCS) live-cell imaging method is needed that enables simultaneous quantitative investigation of the nuclear mass, dimensions, growth dynamics, and density of live specimens [52].

3.2. Optical clearing of biological specimens

For several decades, histological techniques have been the standard for tissue investigation. Despite the benefits of large 3D samples, imaging and analysis only a thin section of a whole tissue sample is more convenient. However, examining only a selected tissue section limits the comprehensive understanding of the biological mechanisms and processes of an entire organism [53]. Optical sectioning, as an alternative solution, reduces time and human resources by distinguishing in-focus signals from out-of-focus backgrounds and allowing the creation of a 3D

representation of the tissue sample without harming it [54]. However, in 3D samples light scattering, caused by the refractive index (RI) discontinuities within and between the model severely limits imaging depth. In particular, fluorescence intensity and contrast are lost due to the scattering of both the excitation and emission lights due to the different refractive indices (Tyndall effect) and the non-uniform distribution of cells and extracellular components [55]. Hence, as imaging depth increases, the number of emitted photons able to arise from the scanned sample decreases exponentially, effectively only permitting cell screening in the outer layer of the sample. Therefore, as large-volume fluorescent imaging became accessible, many optical clearing techniques were developed to improve 3D imaging [56].

Optical clearing methods were developed for two main reasons: (a) to achieve the highest possible transparency whilst preserving the original size and structure of the sample; and (b) to maintain endogenous and exogenous fluorescence, such as immunofluorescence for the examination of target proteins. Therefore, clearing methods modify the optical properties of biological samples by removing, replacing, and altering certain components. Applying such a protocol helps to achieve uniform RI matching between the sample and the mounting media that enables the imaging of intact tissues, organs, and even entire organisms [57].

Optical clearing protocols can be categorised into 4 main groups based on their fundamental procedures [57], [58]:

- Simple immersion in an aqueous solution with high RI: This method is suitable to passively replace the water content in the sample (*e.g.* SeeDB, Clear^{T}, Clear^{T2}). The aim is to homogenise the RI of the sample to the value of 1.4-1.5, which is typically observed in proteins (~ 1.43) and lipids (~ 1.44). Such immersion methods are commonly used due to the simple, inexpensive components and straightforward protocols [59]. Since these approaches do not rely on using detergents, the lipidic content of the samples can be preserved, enabling the imaging with lipophilic dyes [60]. However, aqueous clearing solution could alter the original structure of samples causing the sample's volume to increase. Considering the samples' size and shape, the optical clearing process may require extensive incubation time [61].

- Delipidation and dehydration followed by RI matching: For the next category, two major steps are needed, including delipidation with organic solvents and dehydration followed by RI matching (*e.g.* benzyl alcohol/benzyl benzoate). For dehydration, either ethanol or methanol is usually used, which can also clear away some lipids. However, after removing the water from the sample, the dehydrated proteins will increase RI value. Therefore, to match the overall RI, samples are immersed in organic solvent that also promotes the removal of the remaining lipid components. These methods are well known for their impressive efficacy since they produce proper transparencies in large samples in shorter amounts of time. However, the usage of fixatives (e.g. ethanol, methanol, and acetone) and organic solvents cause structural changes in the proteins resulting in partial or total loss of fluorescence signal (*e.g.* GFP) [61]. As a result of the dehydration, samples may shrink because the dehydrating agents are unable to completely replicate the interaction that occurs between the water and the remaining intracellular constituents [62]. Due to the detrimental effects of organic solvents, special types of equipment are recommended.

- Delipidation and hyperhydration followed by RI matching: As an RI matching method, delipidation and hyperhydration (*e.g.* Sca*l*e, CUBIC) which uses denaturing agents and non-ionic detergents, are commonly used. During the clearing process, detergents such as Triton X-100 will remove the lipid components which reduces the RI. Urea as a denaturing agent can be used to further reduce the RI whilst penetrating and denaturing the folded proteins. Due to the high urea concentration, the osmotic gradient will enable the hydration of the sample. These simple-to-use methods that can remove lipids from the sample have a high clearing capacity without causing toxicity issues or fluorescence quenching [58]. Due to the removal of the lipid components, the cellular membrane becomes permeable to antibodies allowing immunofluorescent labelling with antibodies [63]. Nevertheless, the hydration-induced expansion of the sample is an undesirable effect that may increase image acquisition time [58].

- Hydrogel embedding followed by delipidation and RI matching: To perform hydrogel embedding optical clearing followed by delipidation and RI matching

(*e.g.* CLARITY), three major steps are required. The first step includes the formation of a polyacrylamide gel in the sample using a mixture of paraformaldehyde (or formaldehyde), acrylamide, and bisacrylamide monomers. After polymerization, the lipid components will be removed from the sample-gel-hybrid by using ionic detergent (*e.g.* SDS). Finally, to make the samples transparent, the hydrogel-embedded samples are placed into an RI-matching solution. The gel can stabilise proteins, nucleic acids, and other small molecules by cross-linking with the gel's mesh, preserving the original integrity of the sample [64]. Furthermore, the porous nature of the hydrogel allows the penetration and diffusion of exogenous macromolecules, such as fluorochromes and immunolabeling dyes [65]. Instead of using organic solvents, delipidation of the sample is possible with SDS, therefore, the fluorescence is preserved [66].

Many modern tissue-clearing techniques provide great optical access even at the subcellular level to intact tissues from single organs or whole mammals. This explains the increasing trends of applying optical clearing protocols for cellular phenotyping assays for 3D-oids as well. Whilst optical clearing methods have been increasingly adopted for cellular phenotyping assays in 3D cell cultures (Fig. 2), quantifying the efficacy of these techniques remains challenging. For the newly developed methods, the majority of studies used diverse qualitative and quantitative methods to measure the clearings' efficacy. However, due to the lack of gold standard metrics and the subjective aspects of human perception, several optical clearing protocols are accessible and utilised without an adequate assessment of their efficiency [67].

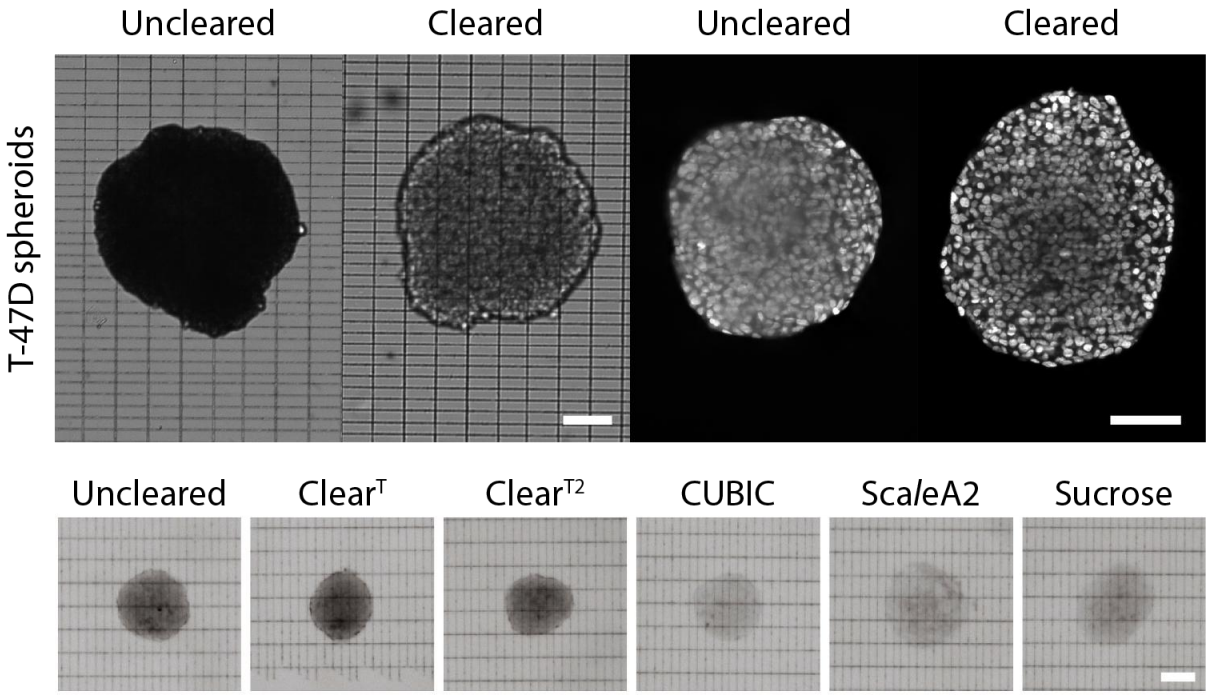

Figure 2. Qualitative analysis of cleared T-47D spheroids using various optical clearing protocols. The top row features brightfield and fluorescence images of uncleared and cleared T-47D spheroids (with an approximate size of 350 µm). Spheroids were cleared using Sucrose protocol. Scale bar represents 100 µm. In the bottom row, brightfield images of T-47D spheroids with a size range of 180-220 µm were cleared with Clear^{T}, Clear^{T2}, CUBIC, ScaleA2, and Sucrose. Scale bar represents 50 µm. All images were captured using a Leica SP8 microscope. Figure is adapted from [68] and [69].

3.3. Imaging of biological samples in 3D

For the accurate evaluation of physiologic and phenotypic details of 3D specimens, spatial awareness is essential. 2D images produced by low-throughput methods are not sufficient to understand complex interactions and processes in 3D. Nevertheless, 3D imaging has proven advantageous in diagnostic, prognostic, and therapeutic decision-making [70]. Recent 3D microscopy technologies aim to reach either true high-throughput 3D imaging or high-penetration depth. However, there are many options and challenges for selecting the most convenient method. The next section is a summary of the most impactful imaging techniques used today to facilitate the best possible 3D reconstruction for -oids.

Wide-field fluorescence microscopy is often used to acquire 2D images whilst illuminating the entire sample that unnecessarily excites fluorophores outside the

depth-of-focus of the objective. Since it is not able to discriminate between out-of-focus signals, decreased signal-to-noise ratio (SNR), photobleaching, and phototoxicity occur. Therefore, imaging large specimens generally results in a blurry projection of the whole sample regardless of the position of the focal volume.

Whilst confocal fluorescence microscopy also illuminates the entire sample, it uses a pinhole to block photons originating outside of the focal plane and separate out-of-focus signals. As a result, 2D optical sections are obtained that illuminate the region within the focal volume of the objective. To acquire a 3D image, the sample is moved through the focal volume to create a stack of optical sections. Since the entire sample is fully illuminated for every optical section of a 3D image, a strong photobleaching and phototoxicity effect is expected, especially for large samples which require more frequent irradiation [71]. Since both the emission and excitation lights experience significant scattering when they pass through the spheroid perpendicular to the image plane, the image resolution is typically limited to depth distances of 60–80 μm [55].

Although conventional linear optical microscopes are powerful instruments, light scattering is the main issue that prevents optical sectioning in thick and complex samples [72], [73]. Nonlinear optical microscopy has become an alternative solution to overcome most of the disadvantages of conventional linear optical microscopes. Modalities such as Second Harmonic Generation, Third Harmonic Generation, and two-photon excitation fluorescence utilize nonlinear light-matter interactions that allow improved contrast and, hence, better penetration depth for imaging cellular and tissue samples in general [74]. Although nonlinear optical microscopy has been favoured in the investigation of dynamic physiological processes deep within live preparations, the energy of the excitation light during the imaging causes significant photobleaching and phototoxic effects that prevent extensive usage [75-77].

All of the above-mentioned and many more detailed approaches have already been demonstrated and proven in multiple 3D biomedical science applications. Despite the advantages of these methods, slow image acquisition, low contrast, thermal damage, high photodamage effects, and expensive prices are some of the limitation factors that need also to be considered. These limitations do not occur with the same magnitude in every case, and there are imaging methods and alternative modifications which can overcome some of these challenges.

Light-sheet fluorescence microscopy (LSFM) is capable of true optical sectioning by illuminating a thin slice of the sample on the image plane (Fig. 3). In 2014, *Nature methods* dedicated a collection and announced LSFM as a Method of the Year [78]. Although the first concept of light-sheet microscopy was established more than a century ago (Siedentopf and Zsigmondy et al., 1903), the modern concept of the selective plane illumination microscope (SPIM) was introduced only in 1993 [79]. SPIM uses a cylindrical lens to focus a collimated illumination laser source into a plane, allowing a significantly thinner plane resulting in a higher SNR with low phototoxicity and photobleaching. However, the ineffectiveness of cylindrical lenses to focus a sheet of light thinner than a few microns is the reason for the development of digital scanned laser light-sheet fluorescence microscopes (DSLM). DSLM replaced the cylindrical lens with a low NA objective lens that reached significantly better Z spatial resolution (~ 1µm). The high-speed galvo mirrors combined with the improved optical sectioning create a virtual light sheet that allows for better control of laser characteristics (e.g. reduced exposure time, reduced time per volume, peak power, sheet thickness, and scan size) whilst also enabling higher SNR with lower photobleaching [80]. Over the past ten years, significant technological advancements have allowed LSFM to be widely used in practically every biological discipline resulting in many different types of light sheet microscopy, frequently designed with a particular use in mind [81]. However, the fundamental idea stays the same: the basic components of a LSFM include an illumination objective, a minimum of one laser, motorised stages for translating and positioning samples through the light sheet, a detection objective oriented perpendicular to the illumination objective, and a computer for controlling the device and storing data. However, LSFM has a true optical sectioning capability due to the selective illumination that generates almost no out-of-focus signal (Fig. 3). The illumination of the sample is limited only to the focal volume, allowing the irradiation of the entire sample once per 3D image. Compared to confocal microscopy, the sample is exposed to three to five orders of magnitude less irradiation [71]. Hence, the reduced phototoxicity and photobleaching are significant advantages that allow long-term imaging of live specimens at high temporal resolution. The LSFM's ability to record tens to thousands of images in a matter of seconds is another one of its best features that acquire millions of voxels in parallel. Because of this, raw data sets of an experiment could result in many terabytes, far more than the data produced by traditional fluorescence microscopes.

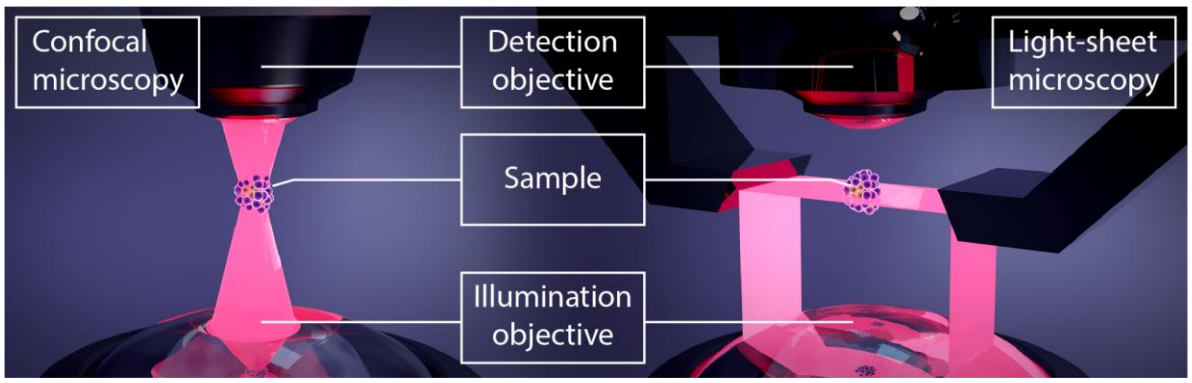

Figure 3. Comparison of confocal and light-sheet fluorescence microscopy (LSFM) setups. The left panel illustrates a confocal microscopy setup where the laser illuminates the entire sample. In contrast, the right panel demonstrates a specific LSFM configuration, where mirrors focus a thin sheet of light on the sample from both sides. Both setups show the illumination and detection objectives along with the sample.

Although many advantages can be listed for LSFM, there is one challenging part, the sample mounting that greatly limits all the versatile setups [71]. Indeed, it can be difficult to mount samples for live imaging assays whilst maintaining the specimens' viability and 3D integrity. Since there are countless different light-sheet setups, the sample mounting related to LSFM has become a broad topic. HCS sample chamber instruments cannot be simply mounted using standard techniques, therefore, plenty of unique mounting and imaging protocols have been produced by the community for specialised cases. Even though these methods offer relatively good compromise solutions, they often do not apply to another LSFM system. There are several light-sheet based microscopes on the market with mostly unique features; however, the lack of standardisation has a great impact on the speed of development [71], [82].

3.4. 3D Image analysis

Once the image acquisition is complete, the vast amount of generated raw data needs to be properly processed and prepared for visualisation, storage, and analysis. However, different experiments require specific approaches that impact the image-processing steps. Whilst every voxel is precious for analysis, the acquired image must be of the best quality, otherwise, we lose storage space, time, and accuracy. Volumetric analysis holds many challenges due to memory issues, 3D

rendering, limited know-how, unintuitive software options, and the computationally demanding processes [83]. Thus, to fully utilise information-rich volumetric data, 3D image analysis calls for additional planning.

The hypothesis, the experimental setup, and a few systemic demands are the key factors determining which downstream processing steps are required. For instance, in 3D pre-processing steps like cropping, resampling, interpolation, and image compression are commonly used, whilst stitching, intensity adjustment, 3D drift correction, deconvolution, segmentation, classification, and feature extraction are less frequently applied. To work with 3D cell cultures, two methods are often applied: either use a single-plane 2D image (mostly brightfield images) [84], [85] or reduce the dimension from 3D to 2D (maximum intensity projection) [86], [87]. Although screening in 2D results in much faster imaging and discarding the third dimension allows faster processing, the less accurate information and the lack of single-cell information may alter the conclusion.

Biological samples are often analysed at a single-cell level in biological research to make conclusions and recommend diagnosis or treatment. Thus, validating efficacy on target cell types is crucial [88]. Single-cell phenotyping assays are essential tools to provide accurate and trustworthy results [89]. Especially since the cell's phenotype is the outcome of multiple cellular processes that combine environmental stimuli and the genetic code of the organism to create unique morphological characteristics. The cellular characteristics are defined and quantified in image analysis through visual cell phenotyping (Fig. 4).

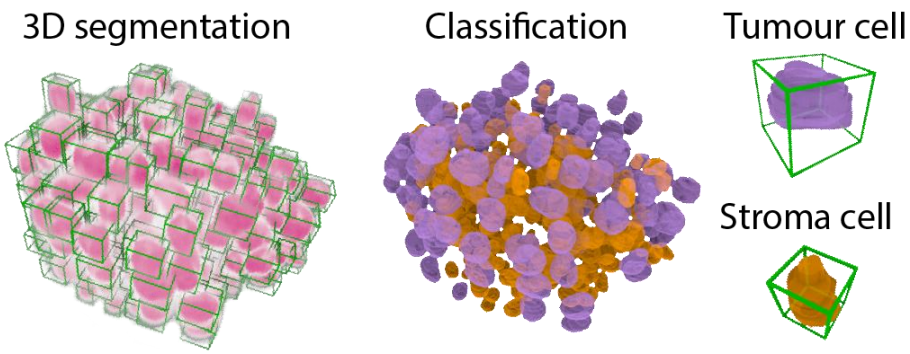

Figure 4. Visualisation of a co-culture spheroid using 3D segmentation and classification based on nuclei information. For the 3D segmentation, each bounding box labelled with green represents an individual nucleus. For the classification, tumour cells are labelled with purple, whilst stroma cells are labelled with orange colour. Figure is adapted from [16].

In medical image analysis and cell biology, machine learning and deep learning (DL) have become essential for image-based object detection and phenotypic classifications [90]. Within the field of artificial intelligence, machine learning is a subfield that focuses on creating models that learn from data and make decisions or predictions without explicit programming. It entails creating mathematical models through the use of statistical methods, enabling the analysis and pattern recognition of sizable datasets [91]. Even though machine learning algorithms provide outstanding results, there are still a lot of issues that need to be resolved [92], [93]. Deep learning, as a sub-field of machine learning, has proven beneficial in numerous visual identification tasks. In particular, DL has emerged as a common standard for phenotypic image analysis, thriving in tasks like object detection, semantic segmentation, feature extraction, and image augmentation [94]. Whilst Deep Neural Networks (DNNs) consist of multiple layers of artificial neurons, it can also learn directly from raw data to produce the desired output. Modern DNNs can have hundreds of layers and can perform multiple tasks using the same network [95]. Because of their flexibility in training and ability to model extraordinarily complex functions that are outside of the reach of traditional techniques, DL algorithms have surpassed traditional machine learning techniques [96], [97].

Due to the increasing accessibility of huge data sets and the development of powerful computational resources, artificial intelligence has been extremely powerful for single-cell level analysis of tissue sections or cell cultures. The overall amount of data generated by HCS microscopes led to millions of images per study, which is usually impressive and shows a high degree of variety. Thus, data analysis is both a computationally heavy and time-consuming process that needs to be automated. Whilst many open-source algorithms are available, new pipelines and tools are emerging all the time for the direct management of 3D data. However, most computational tasks lack a standard methodology, particularly when it comes to single-cell data which often require an advanced degree of expertise. Nevertheless, efficient computational approaches are also required to address the challenges associated with large-scale data management and analysis due to the generation of terabyte-scale imaging data [83]. This provides a significant difficulty in the research, development, validation, and adoption of advanced 3D model systems.

3.5. Comparison of 2D and 3D

To truly show the differences between 2D and 3D models, Table 1 compares their features divided into 4 main categories. The first category, *Models and Treatments*, highlights the structural differences and how these models influence cell behaviour and response to treatments. The next category, *Microscopy* addresses the opportunities and challenges brought by the dimensionality of these models by concentrating on the visualisation methods used for analysis. The *Data* section emphasises key image analysis related aspects, such as software tools, features, and data size. Finally, the *Management* category consists of the practical factors, such as operational expenses, the degree of automation, time requirements, the availability of experts, and initial setup costs, all of which play important roles in determining not only the choice of the model but also the design and setup of the laboratory. This table highlights each model's distinctive qualities (Table 1).

Categories	Features	2D	3D	REF
Models and treatments	Shape of cells	Elongated shape formed on a flat surface.	More rounded, natural shapes	[4]
		Cells are forming monolayers where cells grow and expand two-dimensionally, loss of diverse phenotype and polarity	Cells forming multilayer aggregates in 3D, preserving morphology and way of divisions, diverse phenotype and polarity	[4]
	Cells' interaction with the medium	Cells receive the same amount of nutrients and growth factors	Nutrients are not equally distributed among all cells	[4]
		This results in a higher number of cells being at the same stage of the cell cycle	Cells at the core of the aggregate receive less oxygen and growth factors from the medium that can induce the quiescent state in cells	[4]
	Cell junction	Decreased surface junctions that are less accurate	More junctions that allow precise cell-to-cell communication	[4]
	Drug sensitivity	Cells often show little resistance to drugs, giving the impression that the administered drugs were a successful treatment	Cells often exhibit greater resistance to drug treatment, providing a more accurate representation of the drug's effects	[23]
	Apoptosis	Drugs can trigger apoptosis in cells	Higher rates of resistance to drug-induced apoptosis	[4]
	Cell proliferation	More rapid proliferation	Proliferation rates are more realistic and can vary, depending on the technique and types of cells	[23]
	General understanding	Validated protocols, commercially available tests	High variability in methodology and guidelines, less commercially available tests	[98], [99]
	Penetration	Dyes and antibodies penetrate easily, enabling uniform staining	Molecules are hindered by the dense extracellular matrix and the cellular barriers, uneven distribution and incomplete labelling of cells	[100]

	Consistency	Highly reproducible	Replicating experiments can be challenging due to high variability	[98]
	Pre/ post-selection	Usually, samples are removed after processing	Not commonly used but pre-selection is highly recommended for reproducibility	[101]
	Radiation sensitivity	Shows lower radioresistance	Shows higher radioresistance	[22]
Microscopy	Sample preparation	Mostly easy to execute	Can be complicated, hard to automate	[83]
	Imaging	Easy to automate, simple spatial complexity	Automating for higher imaging penetration is challenging, complex spatial arrangements	[83]
	Depth of field	single plane with a few focus points	Multiple focal planes to visualise the depth of the structure	[71]
	Imaging plate	High variety of options	No commercially validated imaging plate for HCS and high penetration depth	[16], [24]
Data	Software for evaluation	Plenty of free and commercially available, user-friendly software	Mostly specialised commercially available software with limited options	[83]
	Quality measurements/ Analysis	More 2D features, easy to interpret the results	Less 3D features, interpreting 3D data can be challenging	[98]
	Size of data	Due to the single focal plane, the amount of data generated is relatively smaller in size	Can be significantly larger due to the multiple focal planes, the generated volumetric datasets resulting in larger file sizes that encompass spatial dimensions	[83]
Management	Operational Expenses	For large-scale studies, it is significantly more cost-effective than employing 3D culture	Typically incur higher costs compared to 2D cell culture techniques and require more time	[4]
	Automatisation	Extensively used for cell seeding, media changes, and assay plate handling	Usually requires specialised expensive platforms that are capable of precise manipulation or monitoring, fewer options	[83], [102]

	Time	Within minutes to a few hours	From a few hours to a few days (generation, treatment, imaging, data)	[98]
	Experts	Easy to find	Labour shortage on the market	
	Initial Setup Costs	Generally lower	Typically higher than 2D's costs	

Table 1. Comparison of 2D and 3D cell culture models. The table is divided into four main categories: (I) Models and Treatments, (II) Microscopy, (III) Data, and (IV) Management. Each main category was subdivided into multiple features considering the most important aspects.

4. Aims

In this work, our objective was to propose HCS-3D*X*, a high-throughput LSFM-based imaging and single-cell level analysis platform for 3D-oids (Fig. 5).

It includes:

(I) generation of multicellular spheroid tumour models;

(II) application of optical clearings, commercial stainings, and/or chemical drugs;

(III) automated selection and transferring of morphologically homogeneous 3D spheroids;

(IV) developing a custom multiwell plate for LSFM imaging of 3D-oids;

(V) developing 3D data analysis tools for extracting single-cell information.

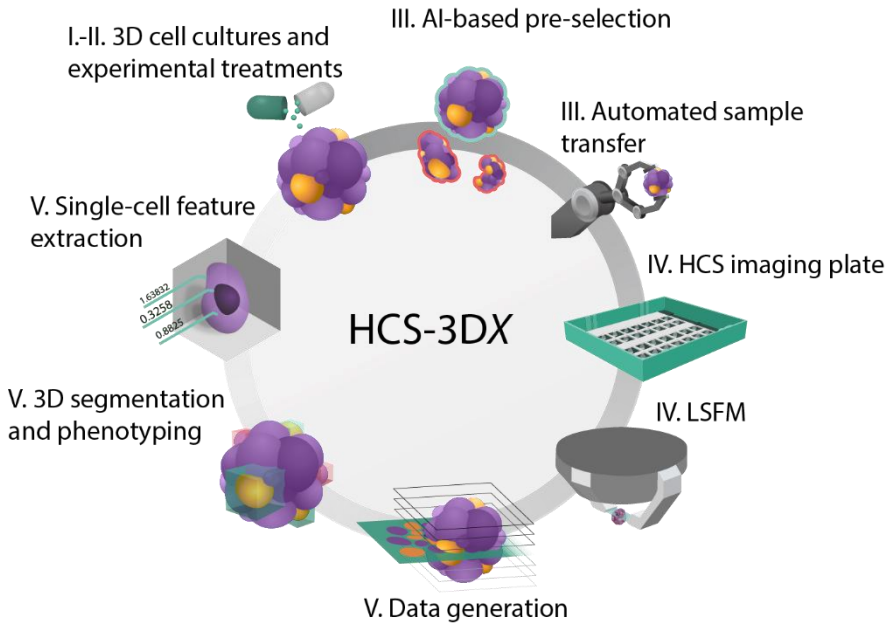

Figure 5. Visual representation of the concept of HCS-3DX. The workflow consists of 5 steps for single-cell analysis of 3D-oids: (I) the generation of 3D cell culture models; (II) the usage of optical clearing protocols, treatments, or staining; (III) AI-driven pre-selection and transferring of 3D-oids; (IV) imaging of 3D-oids with LSFM using a custom made HCS imaging plate; (V) 3D image analysis. Figure is adapted from [16].

Our aim was to provide a detailed guideline that enables fast and automatic screening of 3D-oids with a high penetration depth combined with 3D image analysis. The HCS-3D*X* platform consists individual projects that were published separately in different time points. Therefore, the thesis is constructed based on the previously described step-by-step structure rather than chronological order to make it

comprehensible. To validate the system, we used different kind of tumour spheroids, including co-culture ones as well.

The main aims of this thesis are as follows:

1) To raise attention to the biological significance of the spheroid generation and the increased heterogeneity. Together with the MISpheroID consortium, we aimed to highlight the need for more consistent reporting of spheroid related experiments and to increase reproducibility and transparency in 3D spheroid-based cancer research.
2) To establish a quantitative framework for assessing the effectiveness of optical clearing methods in 3D spheroid imaging. An optimal approach would enable reproducible, single-cell visualisation of spheroid interiors that is crucial for studying cellular heterogeneity.
3) Automating the selection and transfer of spheroids according to morphological characteristics was the aim of the SpheroidPicker project. One of the most time-consuming steps in 3D-oid workflow could be sped up by combining deep learning with a micromanipulator system to enable precise, repeatable manipulation of spheroids, removing human bias and variability in sample preparation.
4) Achieving high-quality, single-cell resolution images of 3D cell cultures is possible with LSFM. Thus, our next aim was to develop a custom HCS multiwell plate for LSFM. The combination of LSFM and HCS multiwell plate is essential for the quantitative, automated, and large-scale imaging of diverse tumour spheroids to examine complex cell-cell interactions.
5) Our final aim was to develop an AI-based image analysis pipeline that can process 2D and 3D microscopy data of 3D-oids. We aimed to overcome the drawbacks of conventional 2D analysis and enable a more accurate representation of the spheroid models using 3D features.

5. Results

5.1. Background

3D cell cultures indeed proved to be an exciting new approach. Over the years, hundreds of publications claimed that 3D-oids are the next-generation models for drug testing, toxicology, or development studies and eventually these models will reduce the number of animal experiments. Such popularity shortly increased the number of publications allowing the formation of big consortia, dedicated conferences, and drawing substantial investment for this field. Although there are many publications discussing their potential, we wanted to see the numbers behind the interest. Using PubMed – provided by the National Library of Medicine (NLM) at the National Institutes of Health (NIH), – we collected and summarised publications starting from 2010 to 2024. Based on a literature search using specified queries, we found about 40,000 articles about 3D cell cultures (based on the search terms “spheroid, organoid, tumoroid, and assembloid”) [103]. To give it a context, during the same period, there have been more than 168,000 publications on HCS but only 1% is related to imaging. Since our aim was to develop an HCS system dedicated to 3D-oids, we could only collect 76 publications mentioning HCS imaging of 3D cell cultures. Our investigation confirmed that most of the publications are only talking about the urgent need for such a system, more specifically talking about the challenges and hindering factors. The most common obstacles mentioned are the standardisation issues of model generation in high quantity, the manual staining and transferring processes, high light scattering during imaging, and the lack of automated analysis [83], [99], [104-106]. Meanwhile, there were only a few outstanding methods that tried to overcome different aspects of these challenges [107-111]. Since working with 3D-oids has led to a great deal of variability, developments intended to evaluate the samples must also be adaptable. Systems for imaging and image analysis that guarantee code accessibility, data transparency, and component interchangeability are required.

5.2. Generation of spheroid models

One of the first challenges to overcome at the beginning of the work with 3D-oids is the variability of hundreds of different models and countless versions of protocols. Such excess information not only greatly slows down research but also requires a huge investment in both time and money. Despite the great number of publications, there were no minimum information guidelines for 3D cell cultures.
To address heterogeneity and promote transparency, as a part of the MISpheroID consortium, we created a crowdsourcing knowledgebase and defined a minimum set of experimental parameters to improve reproducibility [99]. Based on the evaluation of more than 3000 published experiments, a surprisingly high percentage of the publications missed key information. Important details like size or culturing method were left out, and only a small number of cases did not mention the cell line used for spheroid generation. Using the website dedicated to MISpheroID (https://mispheroid.org/), users can upload experiments with the suggested minimum information guideline that includes the cell line, the composition of the culture medium, the formation method, and the size of the spheroid.
To emphasise the importance of these parameters, especially the effect of medium, an interlaboratory study with 7 sites were included, where each site used their own batch of HCT116 cell line to generate spheroids using 6 types of culture medium (Fig. 6). As one of the sites, we generated and evaluated the spheroids (Fig. 6a) and compared our results with the outcome of the other sites. Indeed, the type of medium significantly changed the phenotypic landscape of spheroids (such as the spheroids' size and the formation of necrotic core) (Fig. 6b).
Since the different sites have similar conclusions, the results proved the general importance of the culture medium in terms of reproducibility. It is important to note that this work only discussed monoculture spheroids and revealed crucial inconsistencies. Therefore, in the near future more dedicated work is needed to investigate and reveal the lack of knowledge regarding more complex 3D models such as organoids and assembloids. However, nothing shows the exceptional effort of the community more than the fact that after 4 years of its publication, MISpheroID has more than 4500 documented experiments with spheroids generated from 544 different cell lines (*mispheroid.org*).

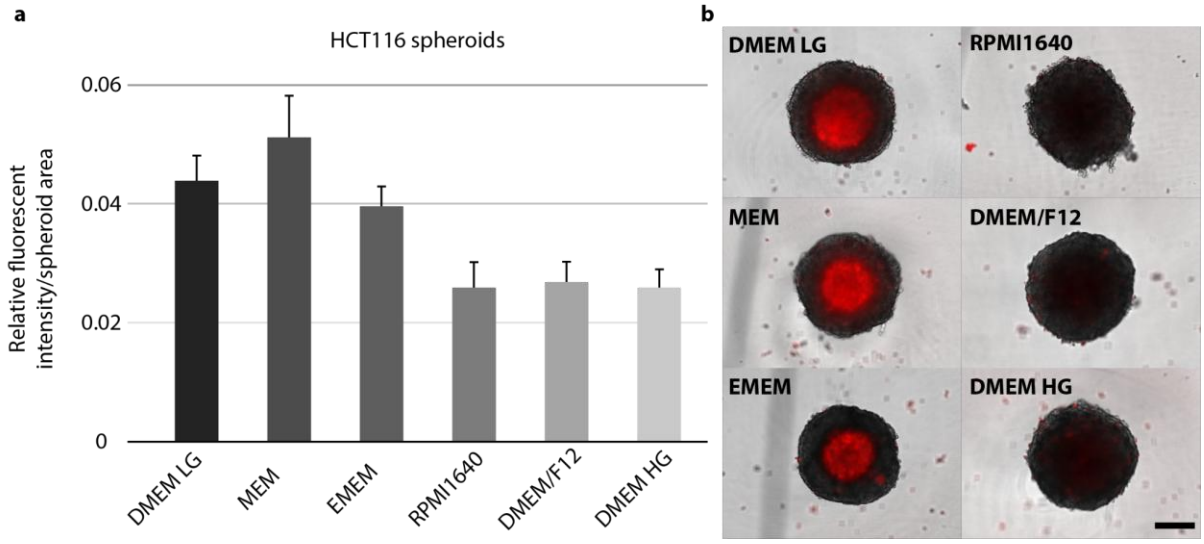

Figure 6. Evaluation of the necrotic core formation in tumour spheroids. (a) Spheroids were generated in a 384-well ultra-low attachment (ULA) plate, 2000 cells/well using 6 different media types (DMEM Low Glucose, MEM, EMEM, RPMI1640, DMEM/F12, DMEM High Glucose) and the same supplements (10% FBS, penicillin and streptomycin). After 5 days, samples were stained with ethidium homodimer-1 (EthD-1) and imaged using the Leica TCS SP8 microscope. Bar plot represents the relative fluorescent intensity that was acquired by annotating the area of each spheroid and measuring the mean EthD-1 intensity. The Fiji software was used to evaluate the images. (n=8) (b) EthD-1 labelled HCT116 spheroids cultured in six different cell culture media are shown in representative microscopy images. Scale bar represents 200 µm. Results and images are adapted from [99].

5.3. Optical clearing methods for single-cell analysis

Whilst there is a huge heterogeneity in the generation of spheroids, several other fields have similar problems. Considering the imaging of any 3D object with a microscope (*e.g.* 3D cell cultures, tissues, organs, embryos), the imaging depth is greatly restricted by light scattering. Strong light scattering causes a loss of contrast and fluorescence intensity when both the emission and excitation light are scattered throughout the sample. Consequently, this limits the imaging depth and effectively only permits cell screening in the samples' outer layer. To reduce the effect of light scattering, tissue optical clearing (TOC) methods aim to chemically increase spheroids' transparency by equilibrating RI throughout the sample. Although TOC methods have been published even before the discovery of 3D cell cultures, due to the popularity and accessibility of the 3D-oids, numerous specific optical clearing procedures have been developed and tested lately [56], [57].

Although optical clearing protocols are increasingly being used in 3D-oids in cellular phenotyping studies [62], [112], it can be challenging to qualitatively evaluate these protocols. The effectiveness of the newly developed clearing process was assessed through a wide range of qualitative and quantitative techniques. For instance, one of the most commonly applied comparisons requires only brightfield images taken both before and after optical clearing. The majority of publications used such a metric which often resulted in a subjective scoring. Therefore, such evaluation is typically based on the transparency changes within the sample and often quantified by measuring the average intensity values [113]. However, when evaluating hundreds of 3D images, these measurements are time-consuming and impractical.

Some of the qualitative metrics are designed to assess the differences in various fluorescence intensity profiles. These techniques were developed on the basis of the observation that intensity and contrast values increase in both lateral and axial dimensions when a clearing protocol is effective and enhances tissue transparency. In this case, the signal-to-background (SNB) ratio, which is the ratio of the intensity profile's mean signal to the background signal's standard deviation, can be used to quantify the changes [114]. As another approach, the differences in mean fluorescence intensity of a 3D sample across various imaging depths can also be calculated [115], [116]. Meanwhile corrected total cell fluorescence (CTCF) was also introduced to measure the changes in the fluorescence signal in response to optical clearing [117-119]. In the literature, using the images' intensity values are often utilised due to the well-known link between improvements in image quality and changes in fluorescence intensity. However, it is important to note that staining quality and imaging parameters that affect intensity values have a significant impact on the results. Additionally, in situations where the analysis requires a manually determined threshold level, the outcomes may be significantly reliant on that particular value. This could easily lead to a misinterpretation of the overall intensity changes.

Segmentation of single cells is another way to assess the performance of an optical clearing protocol. In this particular case, the overall number of well-segmented regions (*e.g.* nuclei, nucleoli, or spot detection) should increase as image quality improves [120]. Despite recent significant advancements in segmentation techniques, no flawless approach has yet been published. Thus, when comparing different clearings, the segmentation-based techniques' results are clearly limited by their dependence on the segmentation method's accuracy.

Given all the aforementioned approaches' limitations, we chose to go with conventional techniques. The first difficulty was finding a simple but effective method to measure the variations among different clearing techniques. Here, we specifically looked for a fast and reliable tool that could assess optical clearing techniques without the need for extra settings, coding, or training a DL model.

5.3.1. Results

In this project our aim was to find an optimal approach for the quantitative assessment of optical clearing protocols. Thus, we implemented and compared 7 metrics and tested them on 3D fluorescence microscopy images (Fig. 7). Additionally, we wanted to compare the efficacy of optical clearing protocols, so we decided to compare publicly available and easy to apply tissue and 3D cell culture clearing protocols. Furthermore, we looked for the most advantageous optical clearing treatments that would enable us to achieve single-cell resolution in the deepest layers of tumour spheroids.

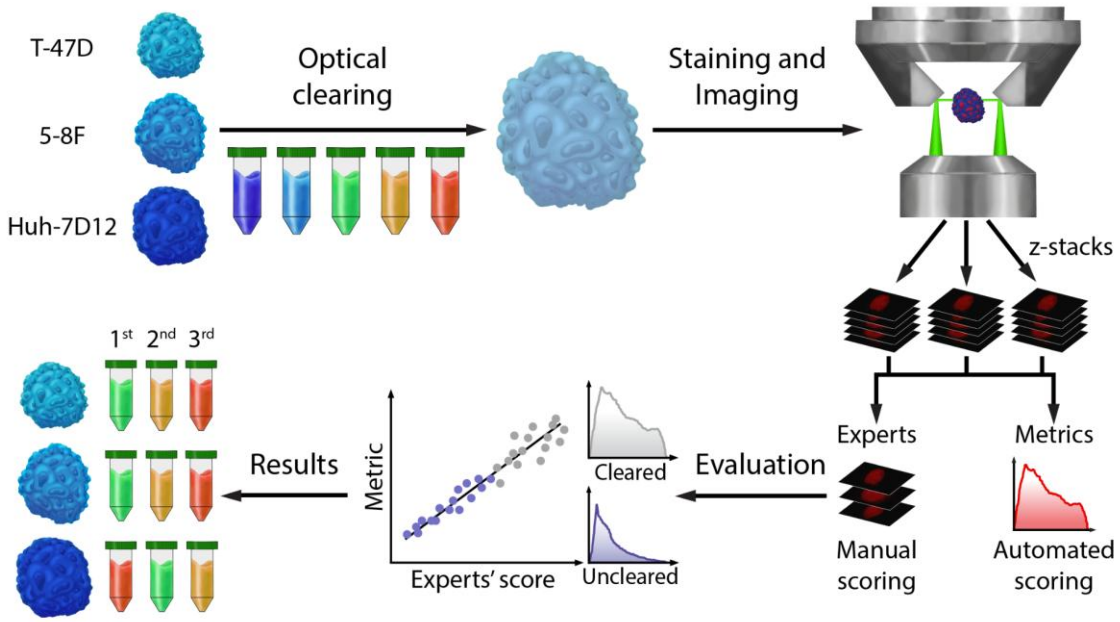

Figure 7. An illustration of the pipeline that summarises our approach for the quantitative assessment of optical clearing protocols. Using various cell lines (T-47D, 5-8F, and Huh-7D12), spheroids were generated. Then, spheroids with a similar size and morphology (about 250 µm) were pre-selected manually and stained with DRAQ5 (nuclei). Five optical clearing protocols were selected (Clear^{T}, Clear^{T2}, CUBIC, ScaleA2, and Sucrose) and applied on each sample. Using a Leica SP8 digital

light-sheet microscope, z-stack images were obtained. For the ground truth dataset, 10 microscopy experts evaluated the quality of fluorescence images, and the experts' scores were compared with 7 no-reference sharpness metrics. Finally, the effectiveness of the optical clearing protocols was compared using the metric with the highest correlation. The figure is adapted from [67].

5.3.1.1. 3D dataset

First, a reliable fluorescence image collection of spheroids was needed for creating a ground truth dataset. In particular, we wanted to use this dataset to compare the performance of the metrics. Thus, spheroids were generated using 3 different human carcinoma cell lines (Fig. 8). Instead of using complex 3D models that could easily include bias in the evaluation, simple monoculture spheroids were used but with different origin (T47-D - human breast cancer cell line, 5-8F - human nasopharyngeal carcinoma, and Huh-7D12 - human hepatocellular carcinoma). Sample variety was also planned to compare the efficacy of the clearing approaches on different types of spheroids. Although the different tumour cells used in this study have unalike behaviours whilst growing into spheroids, we used the same scaffold-free generation method and seeding number, but different incubation times to reach nearly identical diameters (~ 250 µm). Before imaging, spheroids were manually selected with similar size and shape morphology and treated with 5 regularly used optical clearing methods (Clear^{T}, Clear^{T2}, CUBIC, Sca*l*eA2, and Sucrose). Therefore, the overall dataset included 90 spheroids imaged with LSFM (n=5 for each cleared and uncleared groups/cell line) [68].

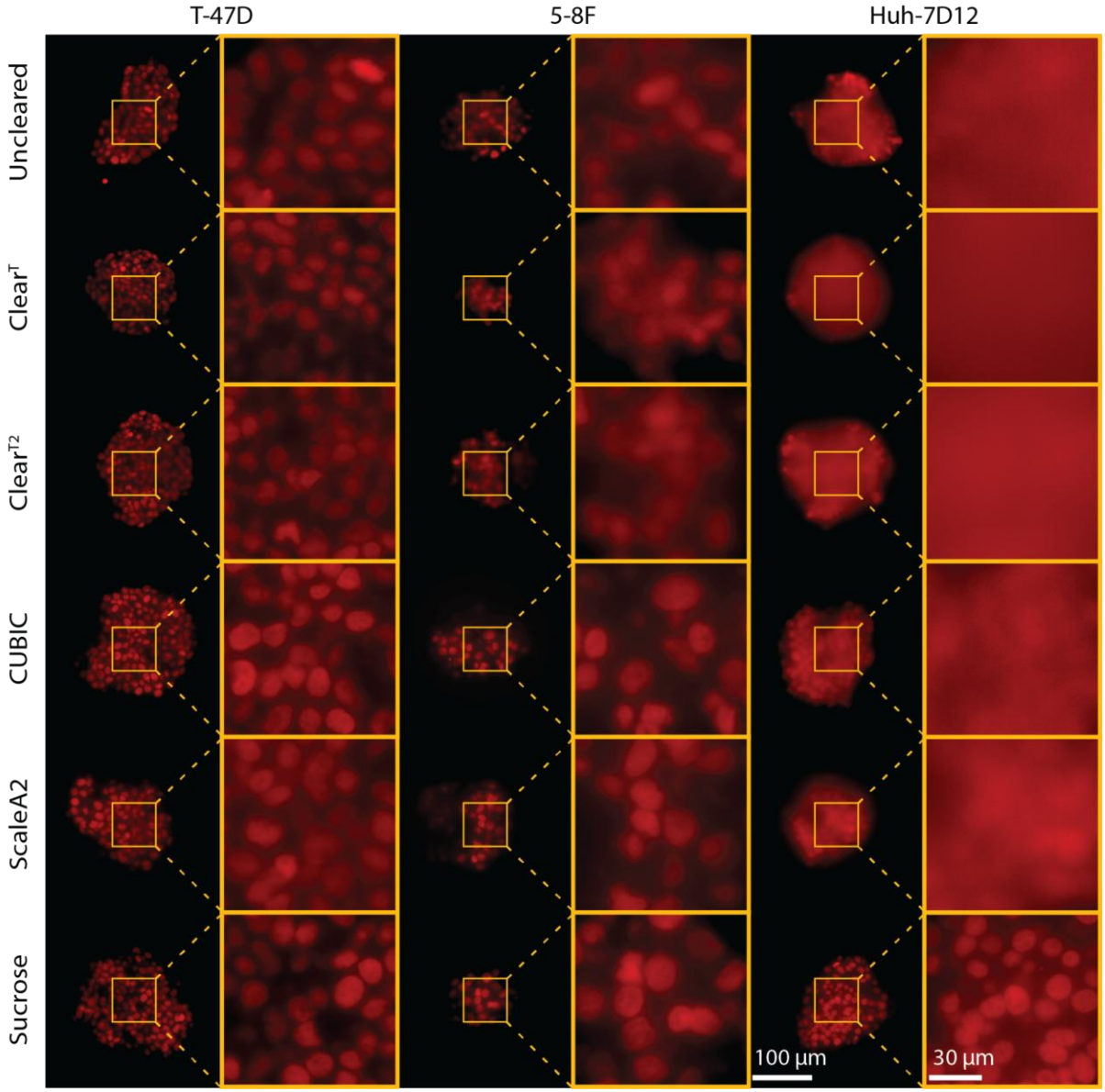

Figure 8. Representative images of the 3D spheroid dataset. The dataset includes 3 tumour spheroids (T-47D, 5-8F, and Huh-7D12) treated with 5 optical clearing protocols (Clear^{T}, Clear^{T2}, CUBIC, ScaleA2, and Sucrose). A Leica SP8 digital light-sheet microscope was used to take images of the spheroids after they had been cleared and stained with DRAQ5. Here, randomly selected images from the bottom regions were chosen for visualisation. The scale bars show 30 µm for the enlarged images and 100 µm for the entire spheroids. The figure is adapted from [67].

5.3.1.2. Expert-supervised ground truth image dataset

Evaluating the image quality of 90 spheroids with more than 5000 images is beyond human processing. Nevertheless, we wanted to benchmark the images and show the differences between the optimal and the less effective optical clearing protocols. Therefore, a team of 10 microscopy experts, each with extensive experience in

spheroid analysis, were involved in this study to score the images. For the evaluation, randomly selected images from the top, middle, and bottom region of each spheroid were used (n=378). Each expert gave a score ranging from 1 to 5, where 1 indicates the lowest image quality and 5 the sharpest. To assess consistency of the experts, some of the images were repeated.

The average self-accuracy of the 10 experts was 81.6%, with the highest consistency being 92.1% and the lowest being 74.5%. According to the expert's evaluation, T-47D and 5-8F samples were generally more transparent than the Huh-7D12 spheroids. The more transparent samples and better-quality images resulted in the greatest inconsistency and decreased the overall consistency of the experts. Among the 3 cell lines, T-47D spheroids received the highest scores, whilst Huh-7D12 spheroids received the lowest (Supplementary fig. 1). In the assessment of the optical clearing protocols, CUBIC, Sca*l*eA2, and Sucrose protocols achieved higher but slightly different scores indicating improved transparency. Whereas Clear^{T} and Clear^{T2} optical clearings received low scores, such as uncleared spheroids. During the scoring, experts were unable to recognise the visible differences between the clearing techniques, except for the morphological changes (shrinkage or expansion) caused by the clearing approaches. For the further experiments, we used the experts' assessment as a ground truth.

5.3.1.3. Quantitative metrics

To evaluate the quality of fluorescence microscopy images, we chose 7 metrics from the literature analysis: intensity variance, Laplacian variance, gradient magnitude variance, histogram threshold, histogram entropy, kurtosis, and frequency threshold (Fig. 9 and Supplementary fig. 2) [67]. Previously described dataset with the evaluation of the experts were used to benchmark each metric. Although experts evaluated only 3 images per spheroid, the metrics were applied to every single optical section of the complete z-stacks. In order to obtain more accurate information, we collected information from the whole area and from the inner parts of each spheroid. By using the internal circle option, we were able to collect data within a certain area of the core region that provided a more consistent measurement.

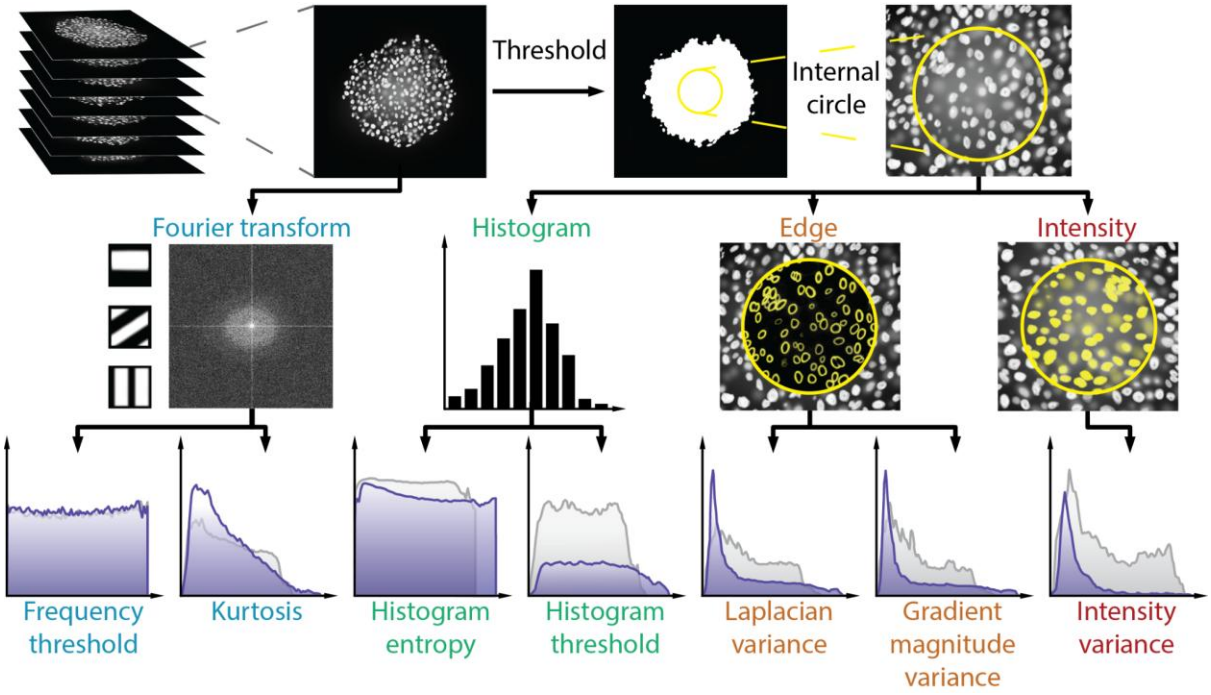

Figure 9. Conceptual illustration for the quantitative metrics workflow. The Fourier transformation-based metrics were assessed on the whole image. Other metrics were applied after an automatic Otsu threshold. The internal circle option was introduced to evaluate the information content at the centre of the objects only for metrics based on intensity, edge, and histogram. Each metric's results were visualised as a plot that described sharpness across the spheroid. Thus, the x-axis indicates how many images were in the stack and the y-axis shows the score that the metric achieved. Only the internal circle's results are shown for metrics based on histogram, edge, and intensity. The cleared spheroids are represented by grey colour, whilst the uncleared spheroids are represented by dark blue colours. The figure is adapted from [67].

The results showed that the intensity variance metric and the ground truth had the highest positive Pearson's correlation (Fig. 10). The overall correlation was 0.67, whereas the internal circle measurements achieved a score of 0.80 (Fig. 10a). Among the 7 metrics, intensity variance metric could accurately represent the experts' assessment. We found that the bottom region had the highest correlation coefficient (0.92), followed by the middle region (0.84), and the top region (0.46) had the weakest correlation coefficient (Fig. 10b-d). The human scoring was less consistent with the higher-quality images at the top region, which led to a weak correlation between the more transparent spheroids and image quality. In general, the intensity variance metric was chosen for the quantitative evaluation of optical clearing protocols because it showed reliable results when compared to the experts' scores (Fig. 10e).

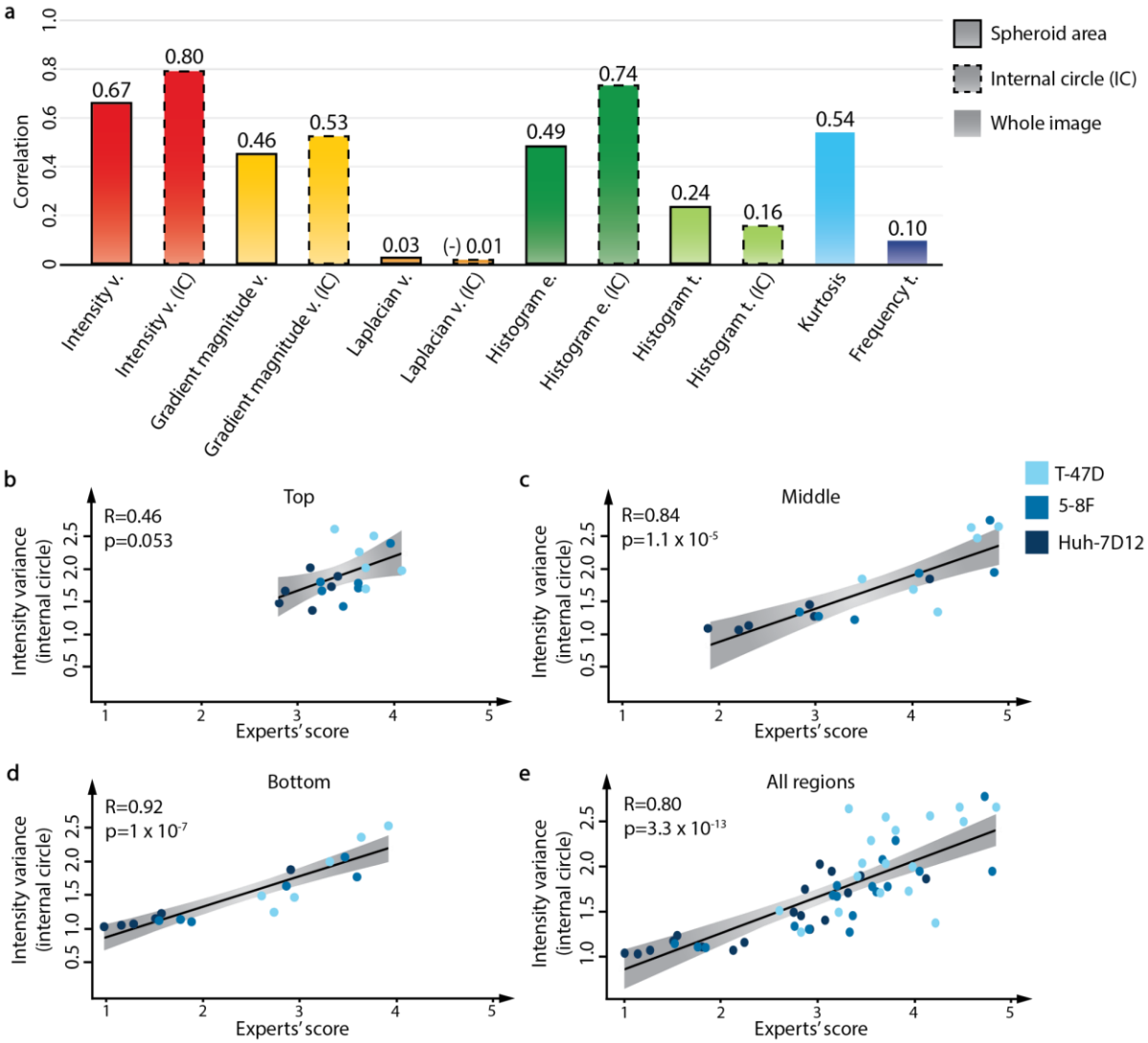

Figure 10. Correlation results between the metrics and the experts' assessment. (a) The bar plot visualises Pearson's correlations between the experts' evaluation and the 7 metrics. T-47D, 5-8F, and Huh-7D12 cell lines were taken into account when evaluating the metrics. Metrics were utilised either on the whole image (Kurtosis and Frequency threshold), the area of the spheroid (displayed with black bounding boxes), or the internal circle (bounding boxes with dashed lines). (b-d) Results of the intensity variance internal circle correlation separated by the top, middle, and bottom regions of the spheroids (n=18). (e) All 3 regions were included to calculate the overall correlation between a metric and the experts' assessment. Huh-7D12 spheroids are represented by dark-blue dots, 5-8F spheroids by blue dots, and T-47D spheroids by light-blue dots (n=54). Pearson's correlation coefficient was obtained for each spheroid, and the correlation was visualised using linear regression. R software was used to perform the statistical analysis. The figure is adapted from [67].

5.3.1.4. Correlation and clearing results

Spheroids analysed with the intensity variance metric confirmed the same conclusions reported by the experts (Supplementary fig. 1). Comparing the uncleared spheroids with the metric revealed that indeed the T-47D spheroids were the most transparent, followed by the 5-8F and Huh-7D12 spheroids (Fig. 11). Additionally, the metric also proved that the bottom region had the lowest scores, whilst the top and middle regions had the highest scores (Fig. 11a). These findings were claimed by the microscopy experts except the fact that the metric were more consistent in many cases. In particular, even though experts were unable to tell the difference between the uncleared and Clear^{T}/Clear^{T2} groups, intensity variance obtained higher scores. This indicates that Clear^{T}/Clear^{T2} protocols slightly increased the overall transparency, especially at the top regions (Fig. 11a). However, there was no significant difference compared to the uncleared samples. The spheroids' transparency was significantly improved by Sucrose, CUBIC, and Sca*l*eA2 optical clearing protocols, and there was no obvious difference when the effectiveness was compared on the T-47D spheroids (Fig. 11b). Meanwhile, Sucrose achieved the highest scores for the Huh-7D12 spheroids and considerably increased transparency for all three types of spheroids. However, the Sca*l*eA2 protocol outperformed all other clearing techniques for the 5-8F spheroids. For the analysis, both the internal circle option and the whole area measurements of the spheroids were used. Both methods separated the optical clearing protocols, however, the whole spheroid assessment decreased the comparison's accuracy. Obtaining information only from the core region, the internal circle achieved better results at differentiating clearing methods (Fig. 11b).

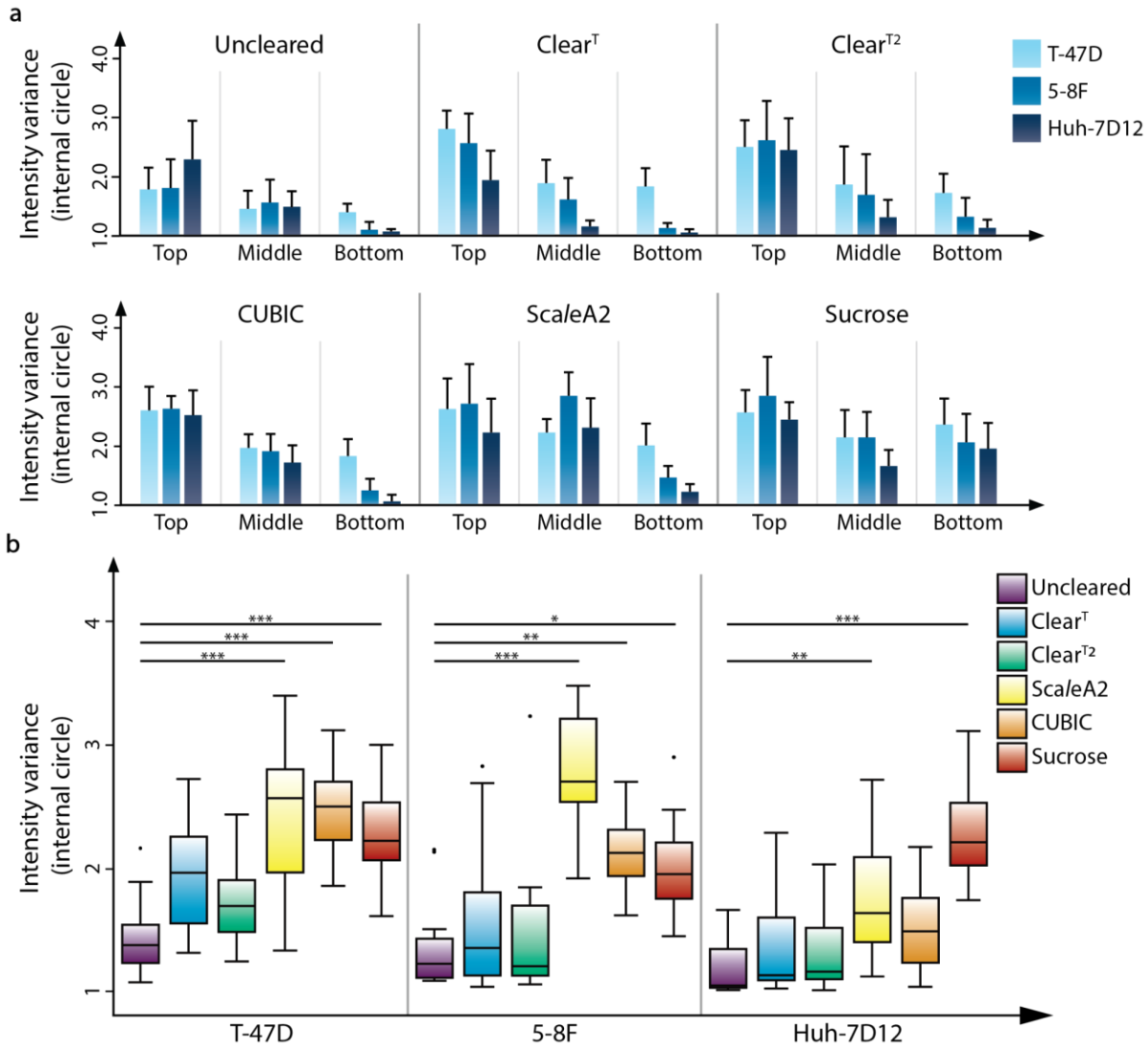

*Figure 11. Quantitative comparison of optical clearing protocols. (a) Using the intensity variance metric with the internal circle option, all spheroids were evaluated at the top, middle, and bottom regions visualised in a bar plot. T-47D, 5-8F, and Huh-7D12 spheroids are represented by light-blue, blue, and dark-blue colours. (b) Boxplot visualisation of the optical clearing protocols' efficacy. Clearing protocols on each type of spheroid are compared to determine which approach is best for each cell line. The internal circle option was utilized to evaluate each protocol's quality using intensity variance. The effectiveness of each clearing procedure was compared with the same type of uncleared spheroids. Five spheroids were separated into three regions (top, middle, and bottom) for each cleared group, resulting in 15 values for quality evaluation. The Kolmogorov-Smirnov test was applied to assess the normality of the distribution. For statistical evaluation of the optical clearing results, the non-parametric Kruskal-Wallis test was conducted, followed by Dunn's multiple comparisons. *p ≤ 0.05; **p ≤ 0.01; ***p ≤ 0.001. The figure is adapted from [67].*

5.3.2. Conclusion

This work led to 2 individual publications. First, we published a 3D light-sheet dataset of 90 tumour spheroids that were derived from 3 different cell lines as a separate data article [68]. As a value of the dataset, we considered the possibility to test and compare different metrics to characterise the general blurriness of 3D fluorescence images. Furthermore, the dataset is suitable to compare the effectiveness of various optical clearing protocols. In addition, due to the single-cell resolution, the dataset can be used to validate segmentation models or to create training sets for machine learning and deep-learning applications. In subsequent projects, we also trained and validated 3D segmentation methods using the dataset's images [103], [121]. The dataset reached more than 800 downloads according to Figshare [122].

The second publication includes all the details of the 7 metrics utilised in this work, the correlation results with the experts, and the evaluation of the optical clearing protocols [67]. In this case, the primary objective was to find an optimal metric to characterise the general blurriness in microscopy images. For that, all the metrics were implemented in a user-friendly ImageJ/Fiji plugin and applied on the 3D dataset. Due to the lack of gold standard metrics, we used the microscopy experts' sharpness evaluation and compared the results with the metrics-based analyses. After a detailed comparison, intensity variance had the strongest positive correlation with the experts' assessment of the 7 metrics that were tested. Even though the whole area of the spheroids already showed a good correlation, the results of the internal circle assessment showed a stronger correlation with the experts' assessment. Furthermore, the strongest correlation between the intensity variance metric and the human scores was found in cases where the experts were able to reliably distinguish between the effectiveness of the clearings. The experts, however, were unable to categorise images of similar quality, such as images of the top regions and the most transparent spheroids. Since the experts had the greatest consistency errors in these cases, we came to the conclusion that even the best metric might not always show a strong correlation with human assessment. Nevertheless, intensity variance metric may be used as a quantitative tool to assess the relative effectiveness of optical clearing protocols. In light of the beneficial results, we utilised intensity variance metric for assessing how effectively optical clearing treatments work on tumour spheroids.

Since hundreds of optical clearing approaches are available, our additional aim was to find an optical clearing protocol that can be used on all types of spheroids. However, the optical clearing methods selected for this comparison proved that the type of the cell line had a significant influence on the choice of the best protocol. In particular, none of the tested optical clearing protocols worked as well on all three cell lines. In general, T-47D spheroids were the most transparent and required the least amount of quality improvement. Therefore, Sucrose, CUBIC, and Sca*l*eA2 protocols showed equally good results allowing multiple options for optical clearing. Although Sucrose significantly improved transparency in all types of spheroids, Sca*l*eA2 protocol achieved the overall highest image quality for the 5-8F spheroids.

Finally, for the Huh-7D12 spheroids, only Sucrose optical clearing allowed us to detect single nuclei even at the bottom region.

The evaluation helped us choose the best clearing techniques for every cell line, which enabled us to achieve single-cell level resolution at different tumour spheroids with a diameter of 250 µm. Our results demonstrated that none of the 5 clearing protocols had the same level of success on all 3 cell lines. Thus, selecting the best optical clearing requires a proper, in-depth comparison of clearing protocols. Especially since the type of the spheroid has a significant influence on the effectiveness of the optical clearing. Considering these findings, we recommend intensity variance as the gold standard metric for quantitatively comparing various optical clearing methods.

5.3.3. Methods

The T-47D, 5-8F, and Huh-7D12 cell lines were maintained according to the suggested guidelines (ATCC, NCI - Frederick, and ECACC). Spheroids were generated using SphericalPlate 5D (Kugelmeiers Ltd., Erlenbach, Switzerland) seeding 750 cells per spheroid. Only the Huh-7D12 cell line was incubated for 4 days, whilst the other cell lines were incubated for 7 days to reach a size range between 200 and 250 µm in diameter. Spheroids then were washed with DPBS and fixed with 4% PFA for an hour at room temperature. Five spheroids per group were pre-selected based on their morphology and size. Five optical clearing protocols (Clear^{T}, Clear^{T2}, CUBIC, Sca*l*eA2, and Sucrose) were used according to Diosdi et al. [68]. Uncleared and cleared spheroids were stained with DRAQ5 to visualize cell nuclei.

Spheroids were imaged into a Cellview™ cell culture dish and U-shaped glass capillaries were used as sample holders. The U-shaped glass capillary was filled with a low-melting point agarose (1% dissolved in dH_2O) and samples were placed on top of it. Then, a droplet of agarose was placed on top of the sample to fix the sample's position. Depending on the optical clearing, different mounting media were used for imaging.

For the human evaluation, 10 experts evaluated the different cell lines and regions separately. Six images from the same region were displayed at the same time (5 cleared spheroids and one uncleared) where the experts scored between 1 and 5 (1 for the worst and 5 for the best images). Each expert evaluated 378 images and their average scores were used as a reference.

For intensity variance the following formula was implemented:

$$I_{average} = \frac{1}{MN} \sum_{i=1}^{N} \sum_{j=1}^{M} I\,(i,j)\,,$$

$$Var = \frac{1}{MN} \sum_{i=1}^{N} \sum_{j=1}^{M} \left(I(i,j) - I_{average}\right)^2,$$

Where *I* represent the image with a resolution of $M \times N$. Images with blurry nuclei result in low variance whilst images with high variance express very dark pixels to high values indicating sharp contours. A more detailed explanation about the tested metrics and the score calculation is provided according to Diosdi et al. [67]. For the statistical analysis, R software was used. The normal distribution of the data was evaluated using the Kolmogorov-Smirnov test. The non-parametric Kruskal-Wallis test with Dunn's multiple comparison was used to confirm the performance of the optical clearings. P-values were adjusted to take multiple comparisons into consideration, and the significance level was set at $\alpha = 0.05$ with a 95% confidence interval.

The Spheroid Quality Measurement (SQM) open-source plugin is freely available in ImageJ/Fiji or can be downloaded by using this link: https://bitbucket.org/biomag/qualitymetricplugin/downloads/.

5.4. Spheroid Handling: AI-based pre-selection and automated transfer of spheroid models

Nowadays, countless different ways are available to generate hundreds or even thousands of 3D-oids that allow high flexibility in the experiment planning phase. Independently from the generation method, one common aim is to achieve a high number of spheroids with uniform morphology, microenvironment, and cellular physiology to provide reliable assays for clinical studies [123], [124].

Apart from the increasing demands for consistent 3D cell culture applications, the ideal method must enable large-scale, reliable, and repeatable sample generation whilst allowing easy liquid and sample handling, and imaging [125]. Utilising the current technologies, generating thousands of samples at the same time is feasible (*e.g.* Sphericalplate 5D by Kugelmeiers Ltd., spheroid microplates by Corning), however, high heterogeneity of the 3D models is still an issue. By increasing the number of generated samples, it allows a new option to specifically select the ideal samples for further experiments. However, the manual selection of relatively small samples based on their morphology is time-consuming and inconsistent. Nevertheless, this process often requires human assistance that cannot guarantee uniformity.

Commercially available robotic systems for selecting and sorting samples (*e.g.* spheroOne by Cellenion) are relying on classical segmentation methods to collect features and isolate the detected samples. Thresholding, edge detection, or watershed methods are genuinely fast but often result in imprecise object detection that may distort the feature extraction. Furthermore, classical methods are sensitive to variation in imaging conditions (*e.g.* transparency of the object, medium density, and touching objects) and require the user to change parameters for each experiment. To improve object detection, DL segmentation models have been already proven to be beneficial for biological cases [88], [126]. Whilst better precision sounds optimistic, it is important to note that such a model requires a huge training set and the detection speed will be slower than any classical method. Nevertheless, other than the precise object detection, the main focus is the biologically safe transfer of live spheroids.

5.4.1. Results

Our first aim was to develop a fast and accurate DL-based framework for the detection and segmentation of spheroids in brightfield images. Unlike traditional methods, DL object detection provides better accuracy and does not require fine-tuning whilst imaging conditions may vary between experiments. The second aim was to build a robotised microscope that is capable of transferring pre-selected spheroids into various types of imaging plates based on their morphological features. The whole system, called SpheroidPicker [101], includes a light microscope, a micromanipulator, a syringe pump, and a controller computer (Fig. 12a). As a general concept, the source plate (e.g. Petri dishes or microwell plates) is scanned entirely where each spheroid is segmented. Then based on the 2D morphological features, spheroids with the most appropriate shapes and dimensions are selected and transferred into the target plate in a semi- or fully automated way (Fig. 12b).

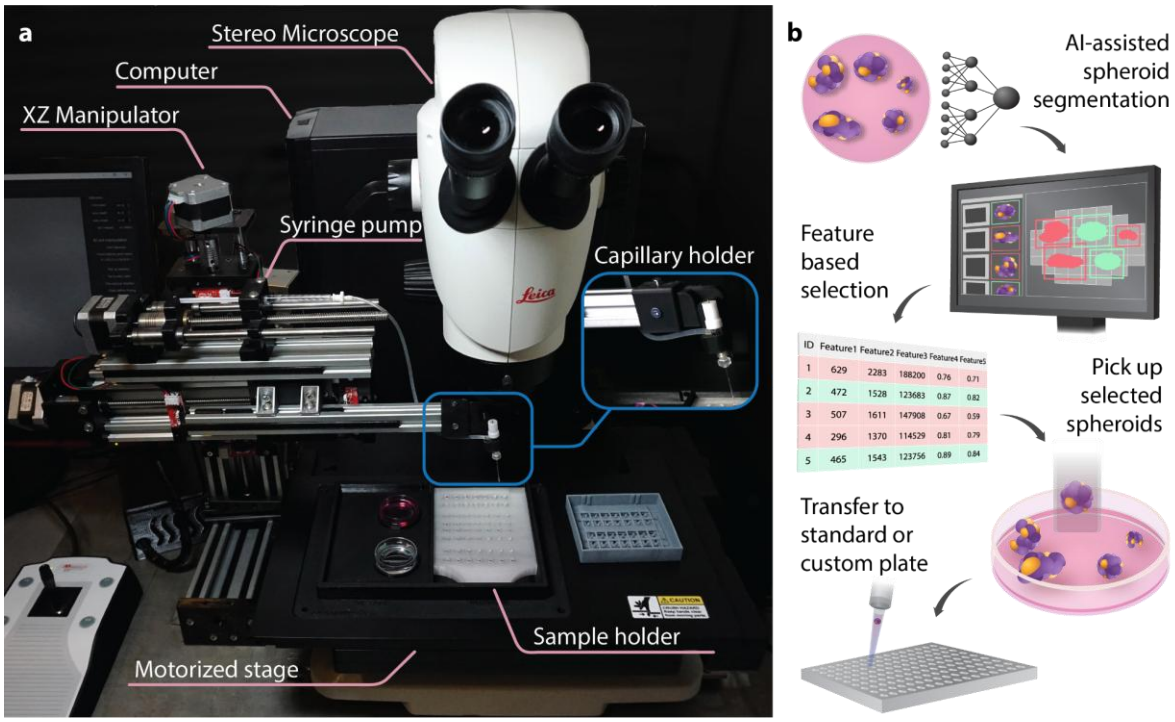

Figure 12. The SpheroidPicker system. (a) Each main component of the system is highlighted in the image. (b) The SpheroidPicker's pipeline allows for the semi- or fully automated transfer of 3D-oids based on morphology features. Image is adopted from [16].

5.4.1.1. Software and hardware

One of the main components of the SpheroidPicker system is a commercially available stereomicroscope (Leica S9i) with a large working distance that allows enough space to build and work around it. Combined with a motorised stage with an optimal 100×150 mm movement area allowed us to design a custom 3D printed plate holder insert element that is compatible with various microwell plates. Next to the microscope, a custom two-axis micromanipulator was placed to provide micrometre precision control. To ensure high-precision fluid movement, a stepper motor-driven syringe pump with 3D printed parts was used. The whole system is controlled by an Arduino Mega 2560 microcontroller. SpheroidPicker was designed as an affordable and compact system that can be installed under a sterile hood. The software handles hardware control, automated imaging, deep learning-based spheroid detection using Mask R-CNN, and a user-friendly interface for custom spheroid selection and transfer criteria.

5.4.1.2. Spheroid detection with AI

In order to train a DL model, we needed a brightfield image dataset of annotated spheroids. For the dataset, we acquired almost 1000 images with 1871 annotated spheroids using our annotator tool called AnnotatorJ [127]. By comparing the results of the segmentations to the expert's annotation, we found that U-net [128] segmented spheroids more accurately whilst Mask R-CNN [129] detected more objects reliably (Supplementary figure 3). In this case, accurate object detection is more important for the object manipulation than a slightly better pixel wise segmentation, therefore, we selected the Mask R-CNN model for our further experiments. To visualize segmentation accuracy, representative example images are provided (Fig. 13). The segmentation's speed was ~ 1s per image. Prior research published a more thorough comparison of different segmentation methods [101], which paved the way for a later development in which the AI-based image detection model was improved [16].
The most commonly reported 2D features from spheroids are *Area*, *Perimeter*, and *Circularity*, according to the literature. These features along with the mass centre and stage coordinates at the imaging position were implemented to distinguish the ideal spheroids. As a result, the operator can manually define the morphological properties, like specifying the size range or circularity values that mostly represents the model.

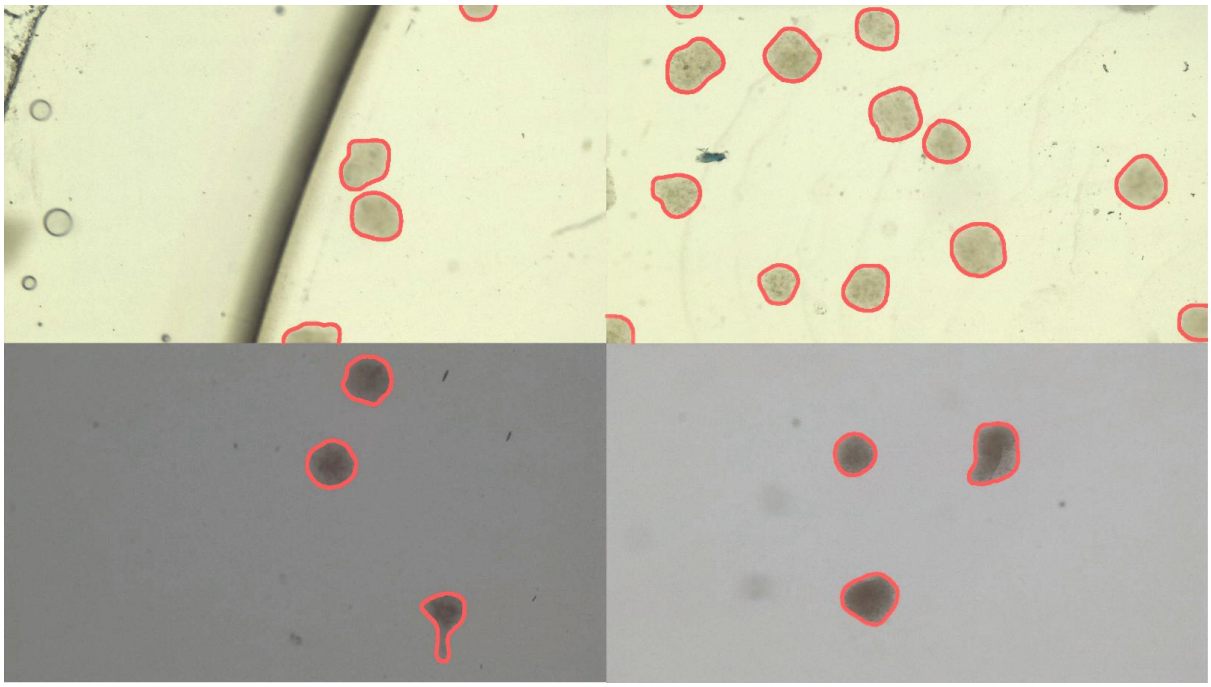

Figure 13. Detection of tumour spheroids using the SpheroidPicker. Spheroids with different morphology were derived from different cell lines and were imaged in different conditions. Red contour represents the result of the segmentation. The figure is adapted from [101].

5.4.1.3. Validation of operation: viability

Using a fluorescent live-dead cell viability assay (Calcein AM and ethidium homodimer-1) on 3 different types of spheroids (T-47D, 5-8F, and Huh-7D12), we confirmed that there was no negative effect that would affect the viability of the transferred spheroids (Fig. 14). The short-term experiment, where spheroids were imaged before and directly after the transferring process showed no significant differences when we compared the morphology and intensity values. Furthermore, spheroids that were transferred showed increase in size after 24 and 48 h, suggesting that cells retained proliferation capacity and no significant degradation effect was measured.

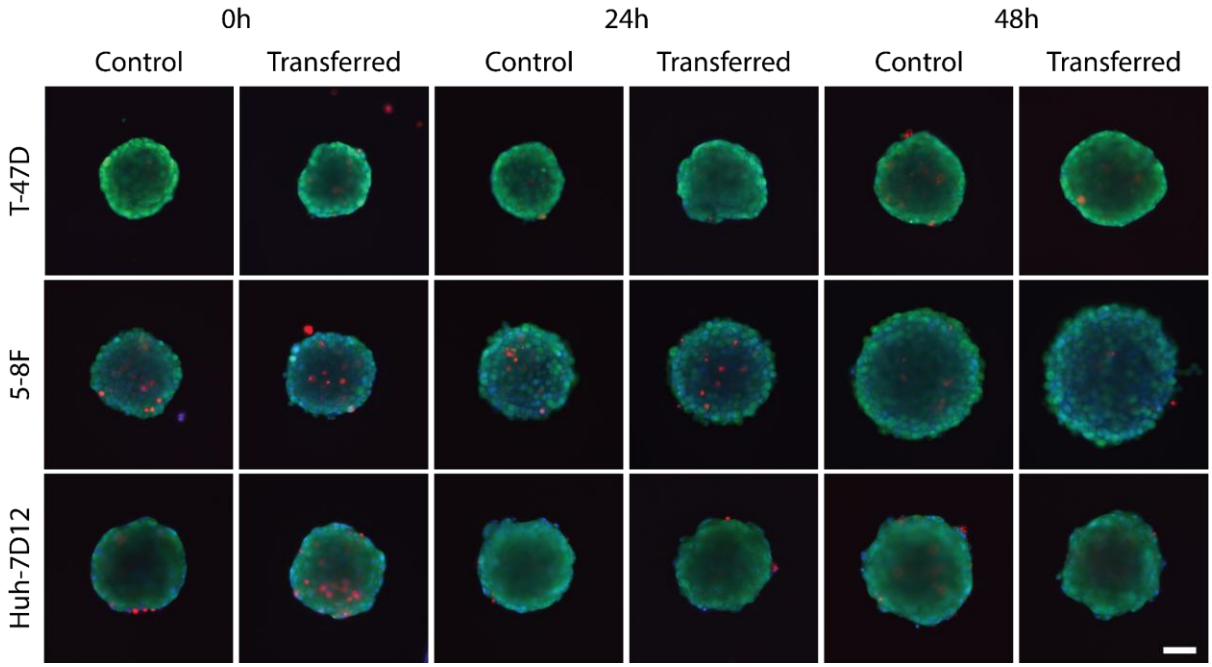

Figure 14. Viability assay of tumour spheroids. Short- and long-term viability assay of the control and transferred spheroids stained with Hoechst 33342 (blue), EthD-1 (red), and Calcein AM (green) at 0 - 24 - 48 hours. Fluorescence images were acquired using the Leica TCS SP8 microscope. Scale bar represents 100 µm. The figure is adapted from [101].

5.4.1.4. Validation of operation: performance

As a final test, we compared the selection and transferring capabilities of the SpheroidPicker to the skills of an expert who manually collected spheroids based on a given size and circularity range (Fig. 15). Both the SpheroidPicker and the expert collected 42-42 spheroids into a 96-well plate and the manually selected spheroids were validated by our system afterwards. For the *Area*, experts collected spheroids with a standard deviation 1.648 times higher with a slightly less circularity in average compared to the SpheroidPicker (Fig. 15a and b). The success rate for transferring spheroids was 89% for semi-automated and 80% for fully automated processes (Fig. 15c). The screening, processing, and the average transferring time on a 96-well plate was also measured (Fig. 15d).

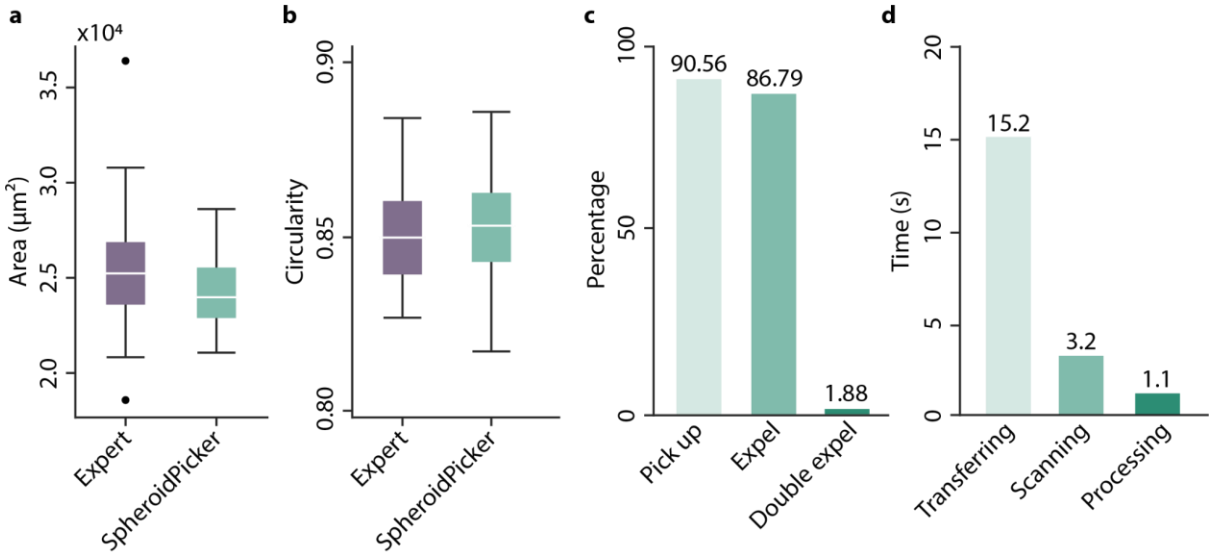

Figure 15. Performance evaluation of the SpheroidPicker. Precision comparison between the expert and the SpheroidPicker. The expert (purple) manually selected spheroids of similar morphology (size and shape) using the stereomicroscope. In contrast, the SpheroidPicker (green) applied selection based on certain criteria. (a) For the SpheroidPicker, 21,000 - 29,000 µm² area range was selected as an ideal size. (b) For selecting the most spherical samples, spheroids were selected with a higher than 0.815 circularity value. (c) Bar plot visualisation of the SpheroidPicker's reliability in percentage. (d) Execution times (s) for various tasks (transferring, scanning, and processing) performed by the SpheroidPicker. The figure is adapted from [101].

5.4.2. Conclusion

For the SpheroidPicker project, hardware and software solutions had to be developed and built in order to automate the spheroid handling processes. First, we needed a stereomicroscope with a relatively large working distance. Then a custom micromanipulator combined with a syringe pump was designed and built around the microscope. Furthermore, an annotated image database, a deep-learning model for spheroid segmentation, and software with a user-friendly graphical user interface (GUI) were needed to allow smooth operation for scientists. All of these components were essential to build an AI-guided automated 3D cell culture manipulator system that can accurately select and transfer spheroids between various sample holders. Using a deep-learning method for image processing resulted in reliable object detection with accurate 2D feature extraction. Moreover, using SpheroidPicker proved to be more precise and consistent in the pre-selection of spheroids, outperforming a

human expert. Samples transferred by SpheroidPicker maintained their morphology and viability throughout the transfer process and showed no degradation effect during the long-term experiments. The system allows semi- or fully automated transferring into predefined well plates. Although SpheroidPicker was tested only on spheroids, the system was generally designed for 3D-oids, which makes it perfect for clinical studies, basic research, and high-throughput tests.

5.4.3. Methods

For this project, the Leica S9i stereomicroscope (Leica, Germany) was selected because of the large working distance to build around the 2-axis micromanipulator. A 10 MP CMOS camera (Leica) was used to create the training set. The data includes overall 981 brightfield images of spheroids that were collected in different imaging conditions. Using the dataset, an expert biologist created mask images that served as ground truth data for the model's training using AnnotatorJ [127]. The dataset including 1871 annotated objects were divided into training (70%), validation (15%), and test (15%) groups.

Standard 24-, 96-, or 384-well plates can be used with a 3D printed plate holder that fits into the motorized stage's insert. To provide a high precision fluid movement (~3 µl), a custom-designed stepper motor-driven syringe pump was developed. The entire system is compact, thus it can be installed under a sterile hood.
Four primary operational steps are handled by the software. It controls the hardware, performs the automated imaging, executes the spheroid detection with a trained Mask R-CNN deep learning framework, and provides a user-friendly graphical user interface to specify personalized spheroid selection and transfer preferences.

To test the morphology changes and viability, similar spheroids as mentioned previously (T-47D, 5-8F, and Huh-7D12) were used [68]. The same technique and slightly different parameters were used to generate spheroids (spheroidisation time was reduced to prove viability on less compact spheroids). A live-dead cell viability assay was used to quantify cell death. For that, 3 dyes were mixed: Hoechst 33342 (1 µg/ml, Sigma-Aldrich), ethidium-homodimer-1 (EthD-1, 4 µM, Invitrogen, Thermo Fisher Scientific), and Calcein AM (5 µM, Invitrogen, Thermo Fisher Scientific) as recommended and added to the spheroids for 20 min at 37 °C. Brightfield and

fluorescence images of the spheroids were obtained at 0, 24, and 48 hours following their transfer into 96-well U-bottom, cell-repellent microplates (Greiner Bio-One). Spheroids were also manually placed onto the same plate for comparison. Both brightfield and fluorescence images of spheroids were acquired using the Leica TCS SP8 microscope and the average EthD-1 stain intensity across the whole spheroid was measured (n≥5). To quantify the morphological parameters, AnaSP software was used [85]. Each experiment was conducted on all 3 cell lines, 10 spheroids per group. Components were 3D printed using an Original Prusa i3 MK3s with PLA and PETG materials, designed in Autodesk Inventor and sliced with PrusaSlicer.

5.5. High-content screening plate for light-sheet microscopy

LSFM has proven to be a suitable imaging technique for visualising fine cellular details at the whole tissue or even at an organ level with minimum phototoxicity and photobleaching [79]. The increased penetration depth, high imaging speed, multiple acquisition directions, and millions of voxels arranged along the three spatial dimensions makes it preferred for the study of large living specimens. LSFM combined with automated image analysis can greatly expedite and lower the cost of traditional histology, therefore allowing dynamic imaging of 3D specimens. Nevertheless, this imaging technique is appropriate for imaging 3D cell cultures as well. HCS solutions developed for 3D cell cultures are mostly based on confocal microscopes where samples are simply placed into a glass bottom imaging plate. However, such imaging offers less flexibility and results in limited penetration depth and the slow image acquisition with high photobleaching. LSFM overcomes these difficulties, it often requires complicated and time-consuming sample preparation processes that strongly limits the potential of HCS studies. In order to fully utilize LSFM systems and increase their potential, an HCS plate is needed.

The obvious assumptions of an HCS plate include the possibility of screening high magnitude of samples whilst each object is separated and allowing the option to be used with automated pipetting systems. However, additional requirements for the plate are high optical properties for imaging, easy-to-handle features, compatibility with existing setups, customizable options for unique cases, long-term imaging, reusability, affordable price, and environment-friendly manufacturability. 3D imaging shows high variety, especially since samples may range from a few cells to small organs.

Therefore, many criteria must be taken into account developing a HCS plate with broad applicability because a variety of factors can change imaging conditions.

5.5.1. Results

In the course of this work, we developed and patented a HCS plate for fast and automatic object screening for light-sheet microscopy at a single-cell resolution (Fig. 16). The 3D imaging multiwell plate has 5 main parts:

(*I*) a mould element to form the cuvettes;
(*II*) a vacuum-formed FEP foil that separates the sample positions;
(*III*) a base element that holds the detection fluid;
(*IV*) an insert element that secures the samples' position inside the foil;
(*V*) a grid element that fixes the position of the FEP foil.

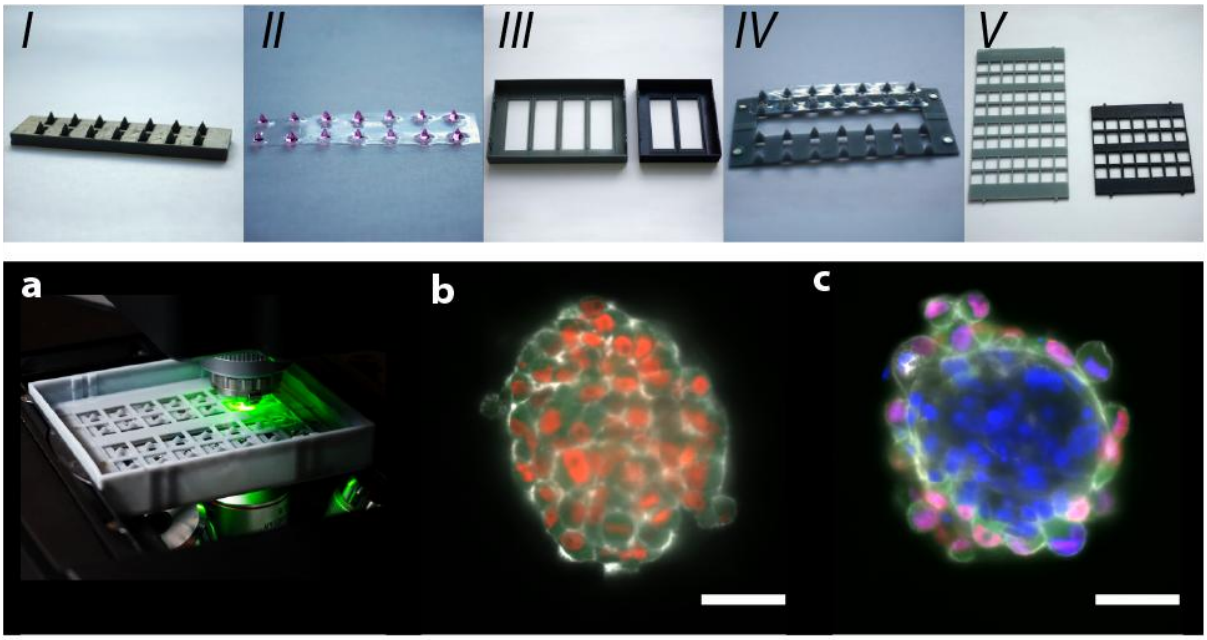

Figure 16. HCS plate for LSFM. Individual parts of the plate are displayed. (I) Heat-resistant mould element. (II) Transparent FEP foil filled with cell culture media. (III) Two versions of the base element where the bigger version is the same size as a conventional imaging plate. (IV) Insert element that is used to fix the samples position within the cuvettes of the FEP foil. (V) Grid element that secures the position of the foil within the base element. (a) Fully assembled HCS plate demonstrated in a relevant environment. (b) Example image of a monoculture spheroid formed by HeLa Kyoto cells (grey represents actin, red represents H2B-mCherry, and green represents

EGFP-alpha-tubulin) and screened using the HCS plate. A randomly selected images from the middle region of the spheroid were used for demonstration. The scale bar represents 50 µm. (c) Co-culture spheroid composed of HeLa Kyoto and MRC-5 cell lines are shown in a representative image (blue for DAPI, green for EGFP-alpha-tubulin, red for H2B-mCherry, and grey for actin). The scale bar represents 50 µm. The figure is adapted from [16].

With a single sample in each cuvette, this plate's design makes it appropriate for analysing a large number of samples using an LSFM (Fig. 16a). The plate was tested with tumour spheroids, screened with the Leica TCS SP8 DLS upright light-sheet microscope, but the design allows the screening of any kind of 3D cell culture (Fig. 16b and c). Samples can be placed into transparent cuvettes filled with cell culture media or hydrogel that is optimal for imaging. The predefined position of the cuvettes is compatible with a standard multi-pipette or a pipetting robot. In each cuvette, the position of the samples is predetermined that allows the automatic screening without the need of recalibration for each sample. Since certain plate’s components are reusable and can be manufactured via 3D printing, the production time and cost are low. Additionally, the only component that must be replaced is the transparent cuvettes that can be produced by vacuum-forming. Whilst 3D printing is not the cheapest method, it offers high customisability to design cuvettes for specific needs within hours. The plate is simple to assemble and doesn't require any changes to the tested microscope, however, various microscopy setups with different objectives may require modifications.

5.5.1.1. Vacuum-formed FEP foil

One of our biggest challenges was to find a transparent material to separate each sample within the plate. The transparent fluorinated ethylene propylene (FEP) foils with a refractive index of 1.341–1.347 are exceptional material for the examination of biological samples, particularly 3D-oids. FEP foil was previously described as a versatile specimen holder that is permeable to gases, cheap, and can be formed by vacuum forming. Furthermore, this material also meets EU (2002/72/EC) and FDA (21CFR.177.1550) requirements [130]. The foil's thickness can vary from 25 to 200 µm and a thin layer of foil is sufficiently transparent to serve as a sample holder and to be safe for use in live-cell imaging. Like most fluorocarbon plastics, FEP is chemically

inert and resistant to most organic solvents, acids, and bases. To create our own sample holder, FEP films (Holscot Europe, Netherlands) with a 50 µm thickness were placed into a JT-18 vacuum-forming machine (Yuyao Jintai Machine Company, China) to create unique shapes. The ideal temperature to form small and uniform cuvettes is between 260 and 280 °C. After extruding, the FEP foil is carefully removed from the mould and cleaned with an isopropyl alcohol bath to get rid of any excess resin components.

5.5.1.2. Positive mould

After selecting FEP foil, the next objective was to plan each cuvette to be easy to use with 3D cell cultures whilst it is compatible with multiple objectives. Since FEP foil was selected as a sample holder, we needed to design the most optimal shape for the cuvettes. Each cuvette should give place to one sample at a dedicated position whilst it should be ideal for imaging as well. We used an SLA (stereolithography) 3D printer with a DruckWege Type D (TDH-VIO-500) heat-resistant resin to create the positive mould with the Prusa SL1 printer (PRUSA). This way we could achieve greater printing resolution, smooth surface properties, and the high mechanical and thermal properties of the heat-resistant resin can withstand the vacuum-forming process. The final design of the cuvette forms a small pyramid-like shape with a sphere on the top that gives space for one sample up to 650 µm in diameter. Just like a standard U-shaped bottom plate, the pyramid-like shape also allows samples to easily sink to the bottom of the foil and take the center position. The distance and positions of the cuvettes are suitable to be compatible with the 2.5x and 5x illumination objectives, the 10x and 25x detection objectives, and the 2.5 mm and 5 mm mirrors. There are 7 cuvettes in each column that allows the manual transfer with single or multi-pipettes, or by using a pipetting robot. This allows overall 28 or 56 spheroids per well, however, the number of cuvettes can be increased. We used Blender 3.0 software to plan and edit the positive mould. After designing a mould that precisely fitted to the criteria, the 3D model was exported to a stereolithographic file format (.stl) and imported into PrusaSlicer v 2.6.1 software for printing.

5.5.1.3. Base element

The base, another 3D printed part of the plate, ensures that there is enough volume for the detection solution whilst the water immersion objectives can move freely inside the plate. Two versions of the plate were tested. The smaller version (85mm/73.8mm/15.4 mm) has the advantage of requiring less detection solution for imaging and is suitable for 28 samples. In contrast, the larger version (85mm/127mm/15.4 mm) scales up to 58 samples and has the same dimensions as a regular plate. Light is transmitted through standard coverslips (24 x 60 mm, preferably 150 µm thick, Menzel Gläser) from below due to the specifications of the upright light-sheet setup. Coverslips can be sealed with hydrophobic sealant such as silicone grease or Elastosil® E41 (Wacker). Small neodymium magnets can be attached to the bottom to secure the position of the insert element inside the plate. To create the base, we used the Prusa i3 MK3S+ (Prusa Research, Czech Republic) 3D printer with PETG (3DP-PETG1.75-01-BK; Gembird, Shenzhen, China). This Fused Deposition Modeling printer provides much faster and low-cost production. All models were 3D printed with the default Prusa PETG filament profile and with “0.4 Quality print settings” using a 0.4 nozzle.

5.5.1.4. Insert element

Hydrogels or a 3D-printed insert element can be used to secure the samples' position inside the cuvettes. Whilst hydrogels are recommended for smaller samples and especially for live cell imaging, the insert element provides an option to fix the position during imaging and collect the sample afterwards. The design of the insert element follows the same pyramid-like shape without the sphere at the top creating a chamber to the samples. When the element is inserted inside the cuvettes, all samples in the spheres are secured without any cell damage or deformation. The FEP foil with hydrogel or insert element should be turned over and inserted inside the base element in order to elevate the samples from the bottom to the same z-positions. The insert has four magnets that connect to the base to provide precise positioning and a locking mechanism for the cuvettes inside. Due to the detailed construct, this component was printed the same way as the positive mould, except that heat-resistant resin is not required.

5.5.1.5. Grid element

A final grid element was 3D printed to secure the position of the FEP foil within the base and to prevent the samples' shifting after filling up with mounting media. Predefined positions for the grid element help to fix the foil to the bottom of the plate. This compartment was printed with the Prusa i3 MK3S+ printer, same as described in the base section.

5.5.1.6. Assembly of the plate

Samples, which can be any kind of 3D-oid, must be carefully transferred into the cuvettes of the FEP foil (Fig. 17). An additional 3D printed part was designed to prevent the foil from moving during the sample transfer process. That element is not a part of the HCS plate, however, it can be used with SpheroidPicker as a stage insert. As a result, the user can choose the HCS plate format in the SpheroidPicker software, thus the automated sample transfer is possible. Before placing the samples, pre-filling cuvettes with liquid (*e.g.* detection solution, cell culture media, or dH_2O) can prevent the formation of air bubbles. Using either a manual method, a single or multi-channel pipette (8 channels), a pipetting robot, or the SpheroidPicker, the transfer process can be completed. After transferring a sample into the cuvette, a visual check is necessary to ensure that the samples are positioned in the centre, exactly at the bottom of the cuvette. It is possible to rearrange the samples' position if they are not in the centre of the cuvette by gently shaking the foil. Once every sample has reached the bottom of the cuvettes and there are no air bubbles, the samples' positions should be fixed using the insert element or any type of hydrogel. Agarose, or any hydrogel for that matter, can permanently fix the samples' position within the cuvettes. In contrast, the insert element enables a different approach that temporarily holds samples in place. Thus, it allows us to collect the samples at the end of the imaging for further experiments. Next, the insert element needs to be gently pressed into the FEP foil in order to hold the samples inside the cuvettes. The entire FEP foil containing all of the samples needs to be turned over because of the light-sheet microscope's TwinFlect mirror setup (Fig. 17). At this point, each sample should be inside the sphere of the cuvettes, elevated from the bottom, and covered with the foil. After that, the foil can be placed

and positioned inside the base element on top of the coverslips. Cuvettes are needed to be aligned, and no air bubbles should appear under the foil. To stabilise and prevent additional foil movement within the base, the grid element should be placed on top of the FEP foil before it is filled with detection media. After the plate has been carefully filled with the detection solution, the calibration procedure can finally begin.

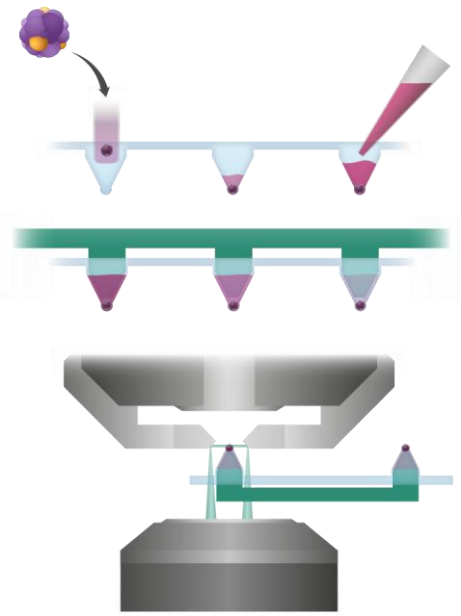

Figure 17. Schematic representation of HCS multiwell plate workflow. Selected spheroids are positioned within the HCS foil-based multiwell plate and stabilised using a dedicated insert element. The fully assembled system is then placed into the LSFM setup, enabling high-resolution 3D imaging at the single-cell level. The figure is adapted from [16].

5.5.1.7. Imaging and image quality

T-47D spheroids were used to validate the image quality and screening time. Spheroids with a diameter around 200 µm [68] were collected and divided into 2 groups (Fig. 18a). Five spheroids were prepared and screened as recommended by the manufacturer of the microscope (Leica). In this case samples were embedded in between 2 layers of agarose, and each spheroid was imaged in individual Petri dishes. For the other group, the HCS plate was used as described previously. In this case, spheroids were transferred into the cuvettes of the FEP-foil, secured with agarose, and screened within the plate. In terms of image quality, there was no visual difference

confirmed by microscopy experts and also no significant difference was measured between the two groups quantified by using the intensity variance metric [67] *(*Fig. 18b*)*. The following experiment wanted to demonstrate the effectiveness of the HCS plate compared to Leica's method. Using 10-10 spheroids, we compared the average time needed for screening in addition to the image quality. The HCS plate performed twice as fast (about 50 min) compared to the agarose embedding (about 110 min) *(*Fig. 18c*)*. The greatest time difference was measured at the sample preparation procedures, where the HCS plate significantly outperformed the embedding method. Specifically, manually moving spheroids into the HCS plate took 14±2 min, whereas embedding samples into agarose took about 37±5 min. The calibration steps for the agarose embedding took roughly 26±4 min to replace and calibrate on each spheroid, revealing yet another major difference. Since all 10 spheroids were separated and put into separate cuvettes with predetermined positions, the individual calibration steps are not relevant for the HCS plate. Therefore, it might not be required to perform separate calibration procedures for every spheroid. The imaging and general calibration steps took 30±3 min for both methods. Additionally, the samples' predetermined positions assist greatly in locating samples within the plate.

The designed plate can be used for many different purposes. For instance, we used the HCS plate to image relatively large optically cleared T-47D spheroids with a diameter of 350 µm (Fig. 18d) [69]. Also, a hydrogel-based multicellular model was used to test the live-cell imaging performance of the plate (Fig. 18e). Additionally, two high quality 3D image dataset was created including co- and tri-culture spheroid models (Fig. 18f) [121], [131].

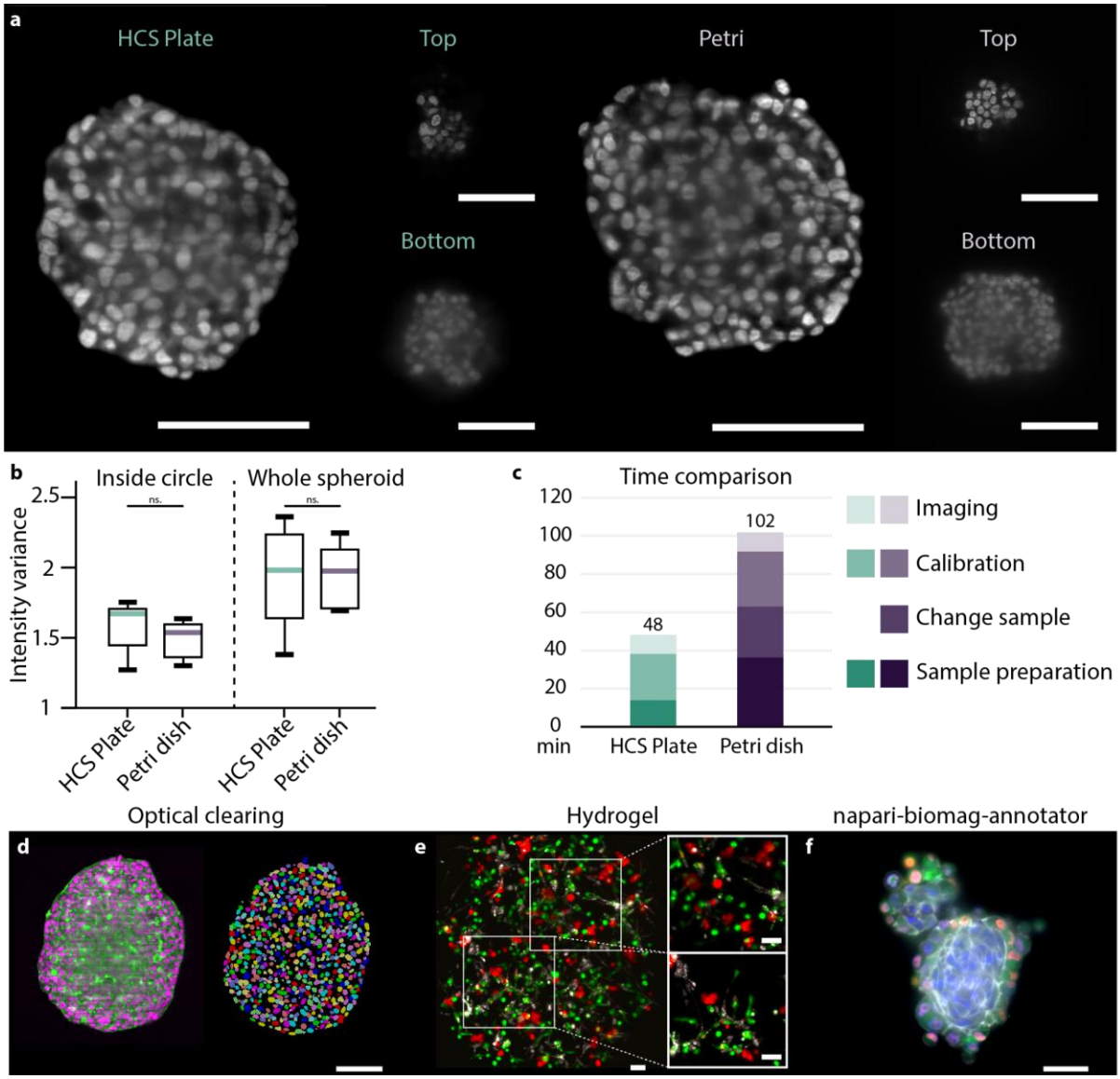

Figure 18. Qualitative comparison between the HCS plate and the conventional imaging technique. (a) To compare image quality, fluorescent images of T-47D spheroids stained with DRAQ5 were used as a reference. Top, middle, and bottom images of randomly selected spheroids screened with the HCS plate (left image) and Petri dish (right image) were displayed. The scale bar represents 100 µm. (b) The intensity variance metric was applied to both the inside circle and the whole spheroid to quantify the overall blurriness of the entire z-stack. A boxplot of the results demonstrates that there were no statistically significant differences between the HCS plate and the Petri. Each group has n = 5. (c) A stacked bar plot was used to show the preparation and screening times for both methods divided into 4 categories: Sample preparation, Change sample (which does not apply to the HCS plate), Calibration, and Imaging. For each method, the total time of 10 samples was displayed. (d) T-47D spheroid with a diameter of 350 µm was optically cleared with Sucrose and labelled with DRAQ5 for nuclei (purple) and Phalloidin 488 for actin (green). Overall, 5184 nuclei were segmented using the BIAS software. Scale bar represents 100 µm. (e) To track the tumour microenvironment in real time, a hydrogel-based tumour model was

*created. The model consists of T-47D breast cancer cells with MRC-5 fibroblasts and EA.hy926 endothelial cells. The CellTracker labelled tumour, endothelial, and fibroblast cells are marked by red, green, and white labels, respectively. Scale bar represents 50 µm. (f) An annotated image dataset of HeLa Kyoto - MRC-5 co-cultures spheroids. The dataset is publicly available at https://doi.org/10.6084/m9.figshare.c.7020531.v1. Scale bar represents 50 µm. For the statistical analysis the Kolmogorov-Smirnov test was used. *p ≤ 0.05; **p ≤ 0.01; ***p ≤ 0.001. The figure is adapted from [16].*

5.5.2. Conclusion

The HCS plate was designed and created to enable quick and automated multiple object screenings within a single plate with predetermined sample positions. The plate was tested on the Leica TCS SP8 DLS upright light-sheet microscope screening tumour spheroids to achieve single-cell resolution. The plate can be used with a multi-pipette or a pipetting robot to place the samples and apply various stainings or treatments, which will reduce the time-consuming sample preparation and transfer procedures. Low-melting agarose or other hydrogels in the cuvettes are ideal for preventing sample displacement, however, in order to obtain high-quality images, the refractive index must match with the sample and the mounting media. Using hydrogel works better with 3D cell cultures that have a relatively small size range (less than 300 µm), although, hydrogels can affect samples differently and can stop or slow down the diffusion of specific treatments. Moreover, it can be difficult to extract samples from hydrogel for further analysis. In contrast, the insert element enables precise positioning and the option to remove the samples after imaging. Since the samples' positions within each cuvette are predetermined, a motorized stage with software support enables continuous automatic screening without requiring the microscope to be recalibrated. An additional benefit of the HCS plate is the low production cost and time. 3D printed parts are reusable whilst the FEP foil, which is the only component that needs to be changed between experiments, can be made by vacuum-forming. Thus, manufacturing or changing the design of the plate is easy and offers a quick and affordable solution for HCS. The plate is simple to assemble and doesn't require any changes to the tested microscope, however, adjustments might be necessary for distinct microscopy setups with various objectives. This is the first high-content screening plate that was designed and tested on the light-sheet microscope with the

TwinFlect mirror versatile setup (i.e., Leica SP8 TCS DLS and Stellaris DLS microscopes). The HCS plate design is easy to use, saves imaging time, and yields images with the same quality as the manufacturer's recommended technique. We achieved single-cell resolution in human cancer spheroids with the same image quality as previously published using the HCS plate, but with a significantly quicker screening time. Furthermore, the plate was already used and validated on different experiments including optically cleared monoculture spheroids with a diameter of 350 µm [69], hydrogel embedded models, and high-quality 3D datasets [121], [131]. The suggested innovation is especially helpful for scientists who work with 3D tissue sections or cell cultures, as well as for industrial drug screening and personalized medical services. Such a system may enable important advances in drug discovery and regenerative medicine.

5.5.3. Methods

T-47D spheroids utilised in this study were generated by following the same protocol as described in the previous publication [68]. For imaging, 5 spheroids were prepared following Leica's guideline. For imaging, a 35/10 mm Cellview^{TM} cell culture dish with a glass bottom and U-shaped glass capillaries for sample holding is required. To create the sample holder, the glass capillary was positioned in the centre of the petri dish and fixed there with a drop of 2% agarose at each end. After the capillary had been filled with agarose, the spheroids were then placed on top of the hydrogel and secured with an additional layer of agarose. The second layer prevents the sample from moving during image acquisition. The best image quality was achieved by removing the U-shaped glass capillary. Lastly, immersion media (dH_2O) were added to the petri dishes.

Another 5 spheroids were selected with similar morphological characteristics to compare the image quality using the HCS plate. Samples were transferred into the cuvettes of the FEP-foil and secured with agarose. Next, the plate was used as described in the *Assembly of the plate* section. For immersion media, dH_2O was used. After mounting the samples on the LSFM microscope, complete z-stacks were obtained. Additionally, 10 spheroids were prepared and screened using both methods in order to compare the average screening time.

The Leica TCS SP8 Digital LightSheet microscope was used to validate the HCS plate. The plate's design enables screening without requiring any changes to the light path or the microscope. Therefore, the plate is ready for use if the standard 96-well plate format is available for the microscopy stage insert. A water immersion 25x/0.95 detection objective with a 2.5 mm mirror device was used to capture fluorescence DLS images. The exposure time was 200 ms at 638 nm with a laser intensity of 15% (maximum laser intensity of 350 mW). Images with a resolution of 2048 × 2048 pixels and a pixel size of 0.144 µm were taken using the Leica sCMOS DFC9000 camera.

5.6. Structural analysis of spheroid models using advanced 3D image analysis

Whilst 3D imaging allows more representative information about the screened object, the importance of 3D features is often overlooked. Despite having additional 3D information, relying strictly on 2D information is the most common way for the analysis of 3D-oids [132]. Mostly because microscopy systems dedicated for 3D imaging are not available for most research groups, besides many commercially available microscopes produce low quality 3D data. Also, 3D analysis is computationally demanding, requiring high-quality data and expertise in the field [83]. When time is taken into account, 2D image analysis is orders of magnitude faster and the whole process, including hardware and software are cost less in general. These factors resulted in significantly more software tools developed and designed for 2D images rather than for 3D images. In parallel, such disadvantages are preventing 3D analysis becoming widely usable and standardized. Although 2D analysis seems more accessible and less demanding, we have to consider the importance of losing the information of one dimension. Over the years, only a few tools have been developed to help bridge the gap between 2D and 3D [133-135].

5.6.1. Results

Morphological features determine our understanding of 3D-oids and certain 2D features are more important than others. More specifically, when capturing image-based features most publications use parameters such as *Diameter*, *Perimeter*,

Area, *Volume*, *Circularity*, *Sphericity*, and *Convexity*. Since we were able to obtain single-cell resolution images of tumour spheroids, we wanted to examine and visualise the difference between 2D and 3D features. Our top priorities were to understand the limitation of 2D measurements and to find a better feature to improve predictability. Therefore, 426 spheroid, 223 monoculture (100 HeLa Kyoto cells/well) and 203 co-culture (40 HeLa Kyoto and 160 MRC-5 cells/well) samples were selected and imaged in brightfield for further investigation. From these samples, randomly selected 110 mono- and 114 co-culture spheroids were imaged with the LSFM using the HCS plate. Nucleus and whole spheroid segmentations were applied on spheroids screened with LSFM.

5.6.1.1. 2D and 3D features

Distribution of individual spheroids were visualised in a scatter plot based on morphological and size-related 2D parameters (Fig. 19). Among the tested features, *Circularity* and *Diameter* revealed a higher number of similar spheroids and a stronger correlation: 55.1% and Rs.: -0.54; and for co-cultures 60.5% and Rs.: -0.69 for monocultures. Changing *Diameter* to *Area*, and *Circularity* to *Solidity*, no correlation was measured, and a lower number of similar spheroids were quantified (49.7% and 50.2% for monoculture and 51.2% and 54.6% for co-culture). Further investigation showed no strong correlation between spheroids' size and morphology. However, based on the selected features, different numbers of ideal spheroids can be isolated.

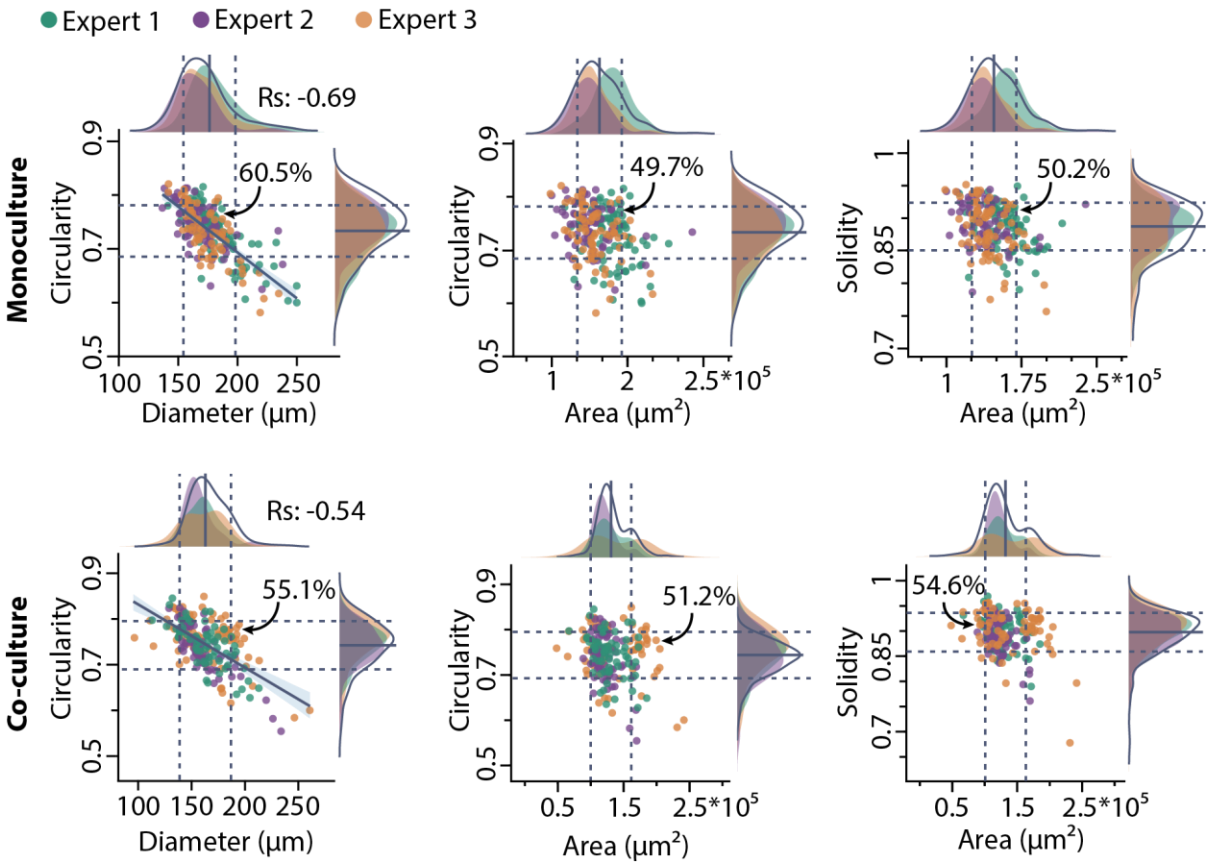

Figure 19. Scatterplot visualisation of the mono- and co-culture spheroid dataset. Based on the 2D features of Diameter, Area, Solidity, and Circularity, the distribution of monoculture (n=223) and co-culture (n=203) spheroids was visualised. Each colour represents a different expert (green for Expert 1, purple for Expert 2, and orange for Expert 3), and each dot represents a spheroid. The dashed lines show the plus and minus one standard deviation, whilst the central lines show the average value for all the samples. The correlation (Rs) was assessed using Spearman's correlation. The figure is adapted from [16].

A sub-group of spheroids (n=37) were selected from both datasets and used for direct comparison of 2D and 3D features. For this analysis, we also included 2D features extracted from the brightfield images that estimates the 3D properties of a spheroid (*e.g. Volume 2D*, *Solidity*, *Sphericity*). The direct comparison revealed that 2D analysis showed in general smaller in size but more spherical objects than what was measured in 3D (Fig 20). Among the shape descriptors, *Solidity 2D* and *3D* features showed the highest correlation.

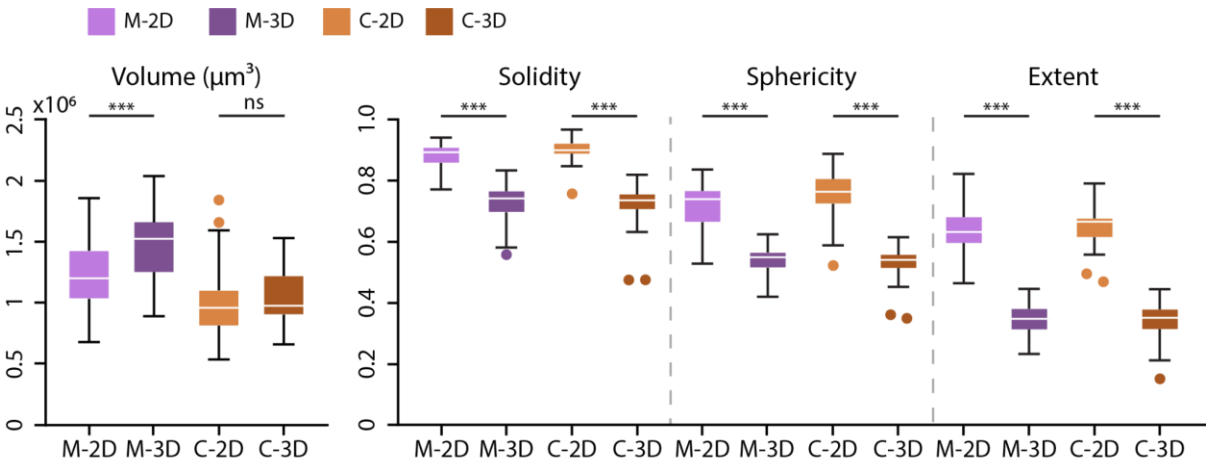

*Figure 20. 2D and 3D feature comparison in a box plot. Thirty-seven spheroids were selected and their corresponding 2D and 3D images collected. Features like Solidity (-), Sphericity (-), Volume 3D (µm³), and Extent (-) were extracted both in 2D and 3D and compared. Results of the co-culture 2D (light orange, C-2D), co-culture 3D (dark orange, C-3D), monoculture 2D (light purple, M-2D), and monoculture 3D (dark purple, M-3D) are displayed. For statistical analysis, the Kolmogorov-Smirnov test was applied. *p ≤ 0.05; **p ≤ 0.01; ***p ≤ 0.001. The figure is adapted from [16].*

Additionally, the 3D nucleus and whole spheroid segmentation revealed a strong positive correlation proving that both nucleus and whole spheroid segmentation is accurate (Supplementary fig 4). However, when *Volume 3D* was changed to *Area*, only a moderately positive correlation was seen, indicating poor predictability.

To determine which morphology feature is more predictable based on the 2D features, we separated the dataset into 2 groups. Using the *Solidity 3D* feature, spheroids were separated either into a Spherical or an Irregular category. The Spherical group showed the strongest positive correlations with *Volume*, *Area*/*Volume 3D*, and *Solidity*, which were 0.78, 0.78, and 0.72, respectively (Fig. 21). There was a moderately positive correlation between *Sphericity* and *Circularity*/*Sphericity 3D*. The more regular shape resulted in better predictability, as evidenced by the fact that the spherical group consistently achieved a higher correlation than the Irregular group.

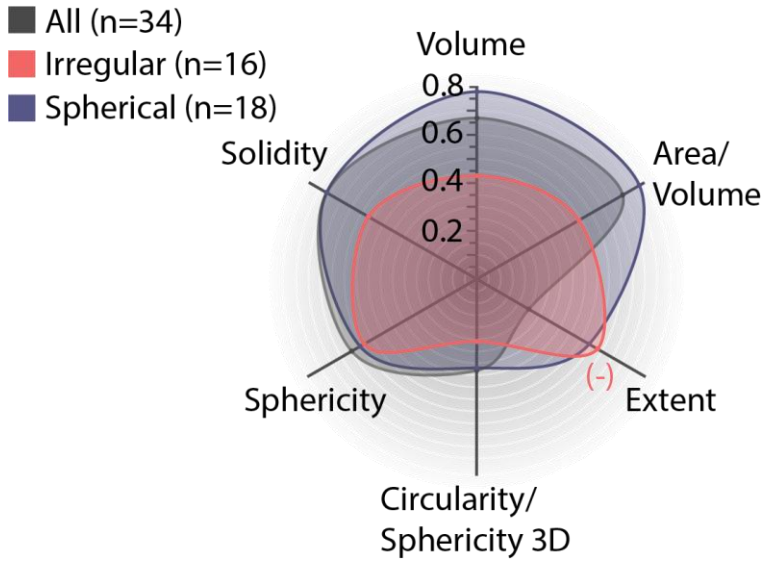

Figure 21. Spearman's correlation between 2D and 3D features is represented by a spider plot. Based on the Solidity 3D feature, paired spheroids (grey, n=34) were ranked and separated into two groups: spherical (dark blue, n=18) and irregular (red, n=16; outliers were removed). The figure is adapted from [16].

Additionally, we tested whether 2D features are representative enough to select similar spheroids with similar 3D morphology. For comparison, we used the highest correlating 2D features (*Area*, *Solidity 2D*, and *Circularity*) to plot and highlight the Spherical and Irregular spheroids. In this case, an accurate 2D representation would result in completely separated groups. However, the scatter plot demonstrated that the data points could not be visually separated into a Spherical and an Irregular group (Fig. 22). The data points are mixed and not visually distinct, even for *Solidity 2D* that showed the best correlation.

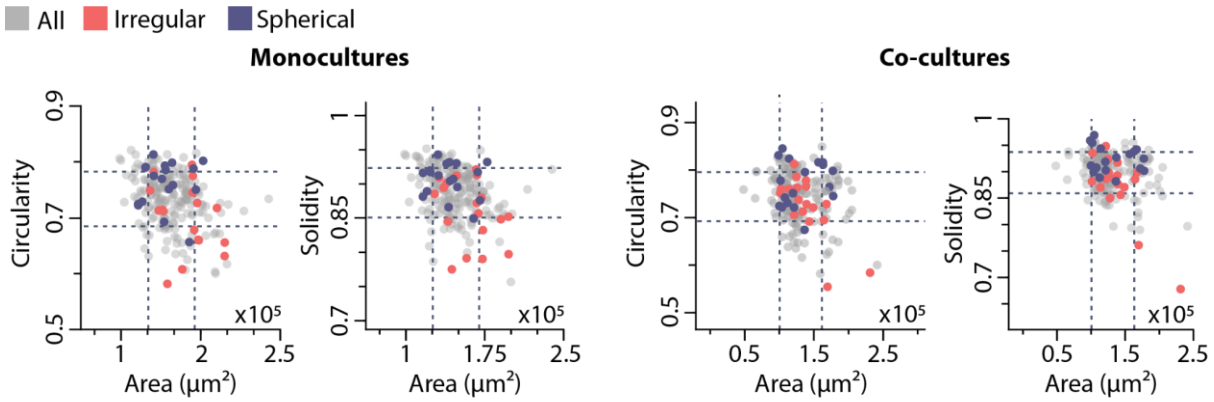

Figure 22. Scatterplot visualisation of the mono- and co-culture spheroid dataset highlighting the Irregular and Spherical samples. Overall, 36 spheroids were divided into a spherical (dark blue) and an irregular (red) group based on Solidity 3D. Using

only 2D features (Area, Solidity, and Circularity), these spheroids and the entire dataset (grey) were plotted where each dot represents a spheroid, and the standard deviation is shown by dashed lines. The figure is adapted from [16].

5.6.1.2. Complex models

The more complex a model is, the more uncertainty occurs during the analysis. Thus, all the experiments were compared on mono- and co-culture spheroid models.
For the monoculture spheroids, the largest spheroid had 2.76 times more nuclei (585) than the smallest (212 nuclei), whilst the average number of nuclei was 358 (Fig. 23). Compared to monocultures, co-culture spheroids contained twice as many seeding cells, however, they were significantly smaller in size. The largest spheroid had 2.32 times more nuclei (423) than the smallest (185), with an average of 280 nuclei for the co-culture spheroids. The smaller size indicates a more compact structure where cells are more densely attached to each other.

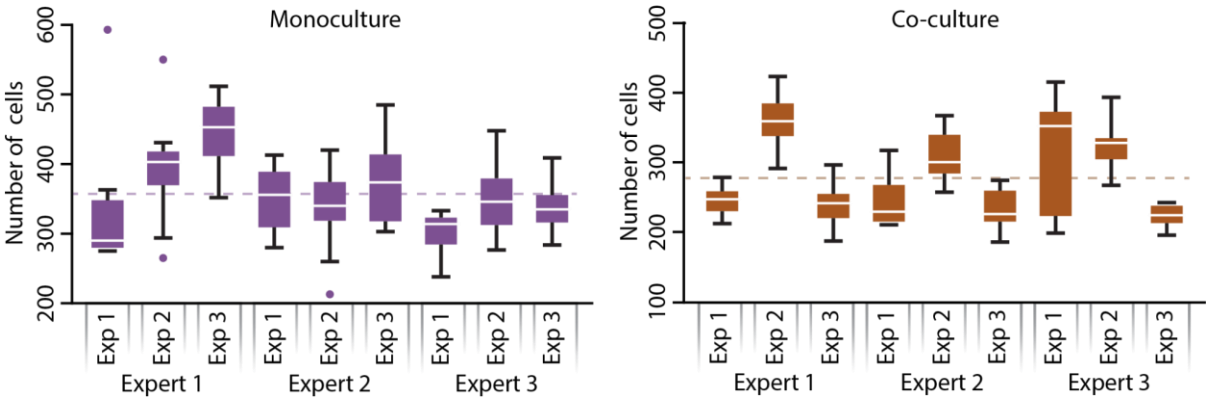

Figure 23. The number of nuclei in the mono and co-culture datasets for each experiment (n≥7) is shown in a box plot. Significant differences were not included. The figure is adapted from [16].

Apart from the morphological differences, 114 co-culture spheroids consisting of HeLa Kyoto and MRC-5 cells, were analysed to understand their structural landscape. According to cell ratio results, 63% of the 114 spheroids were primarily composed of MRC-5 cells (from now on referred to as the M-M group), whereas only 24% were primarily composed of HeLa Kyoto cells (from now on referred to as the H-M group) (Fig. 24a). Only 14 spheroids (referred to as the E group from now on) displayed equal numbers of the two cell lines. Spheroids were then classified based on their cellular composition into H-M, E, and M-M groups. Among the 3 categories, the M-M group

was found to have a higher total cell number resulting in the largest spheroids (Fig. 24b). Whilst H-M spheroids were the smallest. Even though the cell ratio had a significant impact on the spheroids' size, there was no difference considering the shape of the samples. Furthermore, significant variations were observed in the number of cells for the various compositions, regardless of the fact that each spheroid should have a similar number of cells.

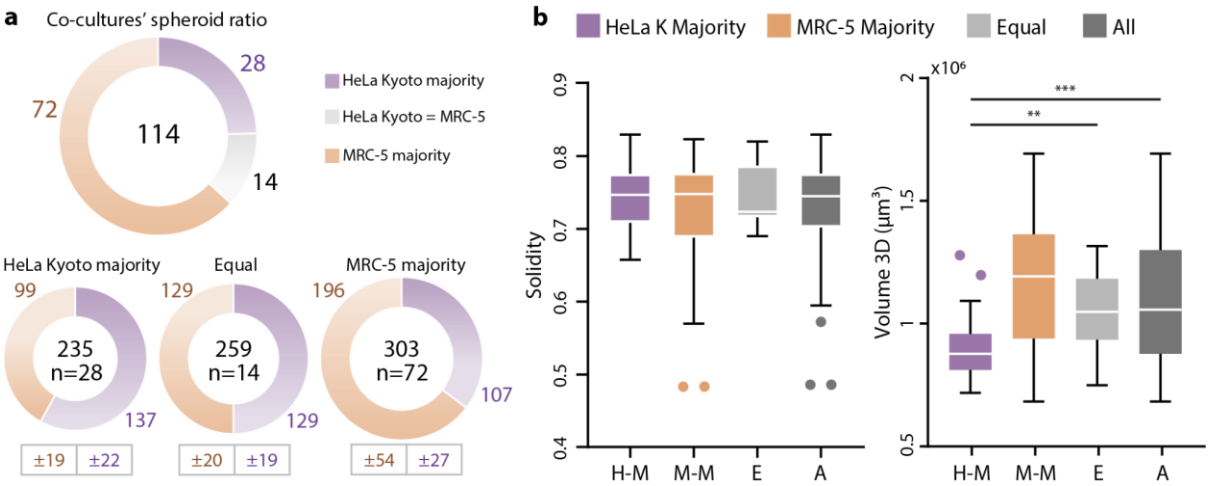

Figure 24. Characterizing single-cell dynamics in co-culture spheroids. (a) By analysing the cell ratio of 114 co-culture spheroids, 72 samples showed MRC-5 cells majority (orange), 28 spheroids with a majority of HeLa Kyoto (purple), and 14 spheroids with an equal number of cells (grey). Based on the majority of the cell type, the 114 spheroids were split into 3 groups: MRC-5 majority (M-M), Equal (E), and HeLa Kyoto majority (H-M). The average cell numbers for each group are indicated by the doughnut charts' size and the numbers in the middle. The average values for each cell type, along with their corresponding standard deviations, are represented in orange for MRC-5 and purple for HeLa Kyoto. (b) The Volume 3D and Solidity 3D features obtained from the spheroids were shown in a box plot according to the 3 groups. The average value of the entire dataset is represented by the dark grey colour. The figure is adapted from [16].

5.6.2. Conclusion

Whilst ImageJ/Fiji is a widely adopted image analysis tool primarily for 2D images, there is no such software with an extensive plugin ecosystem yet in 3D. During the search for publicly available and reliable software tools for analysis, we realized that several options are accessible but with limited features only. Most of the individual steps that are essential for analysis (*e.g.* mask editing, 3D segmentation, classification, feature extraction) were only available in separate image analysis tools.

Also, there are several specialised tools and software packages designed for specific 3D applications. Whilst commercially available software that offer complete pipelines are mostly specific for the imaging microscope. In our experience, there is not a single tool that has achieved the same level of universal adoption and extensive plugin ecosystem that ImageJ/Fiji has for 2D images. Therefore, we started developing our own software solution called BIAS that would work for a variety of 2D and 3D image analysis tasks to analyse 3D-oids at multiple levels.

The selection of features greatly determines our understanding of 3D-oids. Describing a 3D object based on their 2D parameters truly helps to understand certain aspects of its features but greatly decreases our overall understanding of the model. Thus, in this work we generated mono- and co-culture spheroids and analysed and compared them both in 2D and 3D. For the 2D analysis, we used the brightfield images of spheroids that were manually annotated by an expert and extracted morphological features. Fluorescence images were used to collect 3D features, including whole spheroid segmentation, 3D single nuclei segmentation, and classification.

Although spheroids were generated using the same method, comparing hundreds of samples revealed significant heterogeneity due to the nature of 3D-oids. Among the tested features, only *Circularity* and *Diameter* had a moderate negative correlation indicating that smaller spheroids were more circular. This particular conclusion tends to be model specific since the opposite correlation was described in a previous work [136]. However, there was no correlation when *Diameter* was replaced by *Area*. By comparing the 2D and 3D features, we showed that the volume estimation resulted in slightly lower scores than the true 3D volume, whilst 2D shape descriptors always showed higher values. The direct analysis revealed that the most spherical samples showed the highest correlation for *Solidity* and *Volume* estimation, whilst irregular shapes reduce the predictability. Also, the total number of cells within a spheroid showed weak positive correlation with *Area* but strong positive correlation with *Volume 3D*.

In conclusion, size and shape features revealed a moderate to no correlation, making it impossible to identify the number of outliers with a single feature. A comparison of 2D and 3D spheroids revealed that at least 2 features related to size and shape are necessary to describe the population of spheroids. Although 2D pre-selection aids in eliminating strong outliers, it may not select the most similar spheroids in 3D.

As the biological model gets more complicated, the more potential errors may occur during the analysis. To define a multi-cell line spheroid, not only the traditional features (*e.g.* size, shape, number of cells) are needed but also structural information and cell ratio are essential.

Despite the fact that the spheroids' size had no effect on the circularity, spheroid formation was significantly influenced by cell type and ratio. For instance, our co-culture spheroids had twice as many seeding cell numbers than the monocultures but resulted in a much smaller size. A more insightful analysis revealed that based on the cell ratio, co-cultures can be divided into 3 groups. We could also confirm that the different cell ratio caused significant differences in size but not in shape.

2D analysis of 3D-oids provides a more accessible and less complicated process, whilst allowing a faster assessment of the data. However, such analysis is not a precise representation of the data that may result in inconsistent findings. Indeed, perfectly spherical models are best suited for estimating 3D properties, especially using *Volume* and *Solidity* features, but most 3D-oids could show irregular shapes that decrease the overall predictability and comparability. Therefore, including more information about the specimen may improve accuracy and efficiency of drug screening studies.

5.6.3. Methods

HeLa Kyoto EGFP-alpha-tubulin/H2B-mCherry cervical cancer cells (Cell Lines Service, Eppelheim, Germany) were used to generate spheroid monocultures. The cells were maintained in a HeLa Kyoto medium that contained 0.5 mg/ml G418 (Gibco, Montana, United States), 0.5 µg/ml puromycin (Sigma, Kanagawa, Japan), 2 mM L-glutamine (Lonza), 10% fetal bovine serum (FBS, Euroclone, Milan, Italy), in DMEM (Lonza, Basel, Switzerland). In U-bottom cell-repellent 384-well plates (Greiner Bio-One, Kremsmünster, Austria), 100 cells were seeded into each well for 48 hours at 37 °C and 5% CO2 in order to produce uniform spheroids. After 48 hours, spheroids were gathered, washed 3 times using Dulbecco's Phosphate Buffered Saline (DPBS), and then fixed for 60 minutes using 4% paraformaldehyde (PFA). After 3 DPBS washes, the spheroids were kept in DPBS at 4°C until imaging. Spheroids were washed again 3 times with DPBS and incubated in 0.1% Triton X-100 for overnight at

room temperature before imaging. Spheroids were stained with 1:200 Flash Phalloidin NIR 647 (Biolegend, San Diego, California) for 60 minutes and washed 3 times with DPBS before imaging.

MRC-5 fibroblasts (ATCC) and HeLa Kyoto cells were used to create co-culture spheroids. The guidelines provided by the manufacturer were used to maintain the cells.

DMEM, 10% FBS, 1% L-glutamine (2 mM), and 1% Penicillin-Streptomycin-Amphotericin B mixture (Lonza) were utilized as a co-culture medium to create spheroids. In U-bottom cell-repellent 384-well plates, 40 HeLa Kyoto cells were seeded into each well at 37 °C and 5% CO_2. The HeLa Kyoto cells were incubated for 24 hours, and then 160 MRC-5 cells were added to each well. The co-cultures were incubated for an additional day to form a compact structure. Then the spheroids were washed with DPBS 3 times and fixed with 4% PFA for 60 min. The PFA was removed by washing the spheroids 3 times with DPBS and stored at 4°C until imaging. Before imaging, spheroids were incubated in 0.1% Triton X-100 and 1 µg/ml DAPI for overnight at room temperature, and then they were washed 3 times with DPBS. For 60 minutes, spheroids were stained with 1:200 Flash Phalloidin NIR 647. Lastly, DPBS was used 3 times to wash the spheroids.

For the 2D images, fixed samples were put in a glass-bottom 35/10 mm cell culture dish (627965, Cellview, Austria) in DPBS. The Leica SP8 TCS was used to capture brightfield images with a 20x/0.4 objective.

For the 3D imaging, the HCS foil multiwell plate was used on the Leica TCS SP8 Digital LightSheet (DLS) microscope. Fluorescence images were taken using a 25x/0.95 detection objective with a mounted 2.5 mm mirror device, which was illuminated by a 5x/0.15 objective. Using the sCMOS DFC9000 Leica camera, images with a resolution of 2048×2048 pixels and a pixel size of 0.144 µm were taken. In each z-stack, the images were separated by a z-distance of 2 µm. For each spheroid, dH_2O mounting medium was used.

The AnaSP software was used to annotate brightfield images and to obtain the binary masks with the extracted *Volume 2D* feature. Then, images with the corresponding masks were imported to BIAS software for image analysis. 3D fluorescent images were analysed in BIAS using algorithms based on StarDist (nuclei segmentation) and U-Net (for whole spheroid segmentation) methods for segmentation tasks, whilst multilayer perceptron (MLP) was used for classification.

6. Discussion

In this thesis, 5 closely connected aims were pursued:

1. Enhancing reproducibility and methodological transparency in spheroid-based experiments.
2. Standardising optical clearing assessment, enabling consistent evaluation of protocols for spheroid models.
3. Automating sample selection and transfer using robotic systems to minimise human variability and streamline experimental workflows.
4. Developing the HCS multiwell imaging plate for LSFM to screen multicellular cultures at single-cell resolution.
5. Developing a robust image analysis pipeline capable of extracting 3D features from complex volumetric datasets.

Collectively, these efforts have supported the development of the HCS-3D*X* platform. In the following chapters, we give a focused summary of current methodological and technological developments, contextualising our contributions within the broader landscape of spheroid research.

6.1. Biological significance of spheroid generation

3D-oids have changed *in vitro* research by offering more physiologically accurate models than conventional 2D cell cultures. Since 3D cell cultures first appeared in the 1970s in a form of basic multicellular aggregates, the field has advanced significantly thanks to new discoveries and innovative methods [137]. All of these developments lead to a high variety of complex systems, including brain organoids [138], tumours models [139], and even 3D bioprinted models [140-142]. Despite all the promises that 3D-oids can be an alternative to animal models, industrial applications remain limited due to several reasons [143]. The expectation of a complete replacement is hindered by a number of issues, such as the unavailability of reliable validation techniques, minimum information requirements for publications, appropriate standards, and large-scale production protocols [144].

Considering only spheroid models, the community already started to work on some of the mentioned limitations. Analysing the literature revealed that sometimes even the most general information is missing (*e.g.* cell type, cell culture media and formation method, samples' size) [99]. Thus, a crowdsourcing database with minimum information requirements could aid the overwhelming issues of a high variety of protocols. Therefore, the MISpheroID consortium created a database that includes more than 4800 spheroid related experiments with a purpose to improve methodological consistency in spheroid research. By using the MISpheroID website, experimental parameters related to spheroids are recorded as part of each upload. The aim of the database is to improve experimental design, thus it neither reflects nor mandates a particular methodology. Furthermore, it encourages researchers to compare general and specific data and raises awareness, whilst it also allows a variety of search parameters to use when looking for articles in the knowledgebase.

Another important aspect of spheroid research was the intra- and interlaboratory studies that demonstrated how changes in culture parameters, like the composition of nutrients, can have major effects on cellular behaviour and the morphology of spheroids [99], [145]. These results highlight how crucial it is to standardise experimental parameters in order to guarantee reliable and consistent findings across research. As a continuation of the MISpheroID project, 8000 images of various spheroids generated by using different culture media and formation methods were published as the SLiMIA dataset [146]. With an emphasis on spheroids, both the MISpheroID and SLiMIA projects seek to advance research studies to improve, standardise, and expand the use of 3D cell culture methods in biomedical research. Even though these studies focused solely on spheroid models, more work and effort will be required to investigate other complex 3D models.

6.2. Quantitative assessment of optical clearing protocols

The wide variety of protocols has also had an impact on different aspects of working with 3D-oids. For the imaging of multicellular 3D-oids, optical clearing is an essential technique, because it aims to improve the imaging depth and quality of fluorescence microscopy by reducing light scattering. However, direct comparison of clearing

protocols may not be feasible even for an expert, due to the inherent subjectivity of visual assessments, observer-related inconsistencies, and the low throughput associated with manual evaluations. To quantitatively compare the efficacy of various optical clearing protocols in 3D requires reliable, good-quality, and publicly available datasets and an evaluation method. Whilst most publications relied on confocal microscopy images for the evaluation, high-resolution light-sheet microscopy datasets were always appreciated by the community [68], [131]. One important conclusion to be learned from these datasets is the obvious need to test and validate optical clearing methods on a variety of cell lines or tissue types. This heterogeneity is important since the sample's lipid content, structural density, and biological composition can all have a substantial impact on the clearing efficacy. Furthermore, multiple tissue models allow researchers to evaluate a clearing method's general applicability and reproducibility [67], [119]. Despite the numerous tests and publications of optical clearing protocols applied on 3D-oids and tissue samples, no gold standard protocol was chosen [53], [57], [60], [147], [148]. One obvious reason for the high diversity of protocols comes from the specific needs of different samples and experimental conditions. These protocols aim to improve the overall transparency, however, their usage may differ depending on the biological specimens, sample’s size, staining and imaging techniques, processing time, complexity, and reversibility [60]. For instance, the lipid content of the sample, along with the imaging method, frequently affect the clearing protocol selection. Additionally, some clearing techniques are made to preserve fluorescence signals from specific dyes, whilst others were optimized to minimize sample distortion, such as shrinkage or expansion [57]. This high variability makes it possible for researchers to choose the best protocol to produce high-quality imaging whilst preserving the samples' biological significance.

Another obvious reason for the absence of a gold standard method is the inability to properly compare the optical clearings’ efficacy. Whilst many forms of comparison exist, comparing the image quality typically involves both qualitative and quantitative assessments [113], [114], [119], [120]. Qualitative evaluations, such as the visual inspection of the clearings’ effect, usually relying on expert judgment, focuses on the transparency, contrast, and size changes of before and after images [113]. On the other hand, quantitative approaches use metrics to measure the SNR, fluorescence intensity resolution, or quantify the segmented objects [114], [120]. These methods

collectively help researchers determine the effect of the optical clearing protocols but are not exactly suited for proper comparison. The intensity variance metric proved to be an accurate method to assess optical clearing protocols, particularly due to its validation against an experts-defined ground truth [67]. This method is able to distinguish optical clearing protocols with high accuracy even in cases where only one component differs. Furthermore, the quantitative comparison showed a difference between the uncleared spheroids' optical characteristics confirming that the cell line used for the spheroid formation has a significant impact on the clearings' efficacy. Thus, intensity variance might be used as a quantitative tool to assess the relative effectiveness of optical clearing protocols or compare spheroids composed of different cell lines. In addition, the same metric was used to evaluate the image quality of mounting platforms [16].

The high diversity of 3D-oids and the abundance of optical clearing methods reflects the need for tailored approaches in advanced imaging studies. Most TOC protocols were used on fixed samples due to the significant alterations in the molecular profile of the samples. But more recently, protocols for optical clearing on living samples have been developed that may greatly broaden the possibilities for imaging [149], [150]. Although, finding the best optical clearing protocol may not be feasible, yet hundreds of protocols and samples are waiting to be tested.

6.3. Automated spheroid selection and transfer

It has been repeatedly demonstrated that additional information gained by the analysis of 3D-oids can be advantageous to more closely mimic and reproduce the *in vivo* tissue environment [151-153]. Each day, more and more advanced technologies are becoming commercially available for high-throughput 3D cell-based disease models which make 3D-oids widely applicable for research groups in both academic and industrial fields. From the industrial point of view, automatic generation, detection, and handling of spheroids became one of the fastest developing subfields that often required the development of both hardware and software solutions. In the case of the hardware, advanced 3D bioprinting methods, which are still in the early developmental phase, already showed promising results for spheroid generation and manipulation

[154], [155]. Also, engineered microfluidic chips are proved to be clinically relevant for testing tumour or basic organ models [156-158]. In terms of software development, a new era of user-friendly and high precision AI-based 2D segmentation methods appeared [159-162]. Fast and reliable AI-based segmentation methods quickly became popular that opened the door for new opportunities. For instance, the combination of segmentation methods and high-precision robotic systems for the automatic selection, manipulation, and evaluation of spheroids is one of the sectors that greatly benefitted from the parallel development [101], [102], [163-165]. As the spheroid generation has evolved to the level that hundreds or even thousands of spheroids can be produced in a single experiment, the automatic pre-selection of spheroids based on 2D features has become a valid option to decrease the number of outliers.

6.4. High-content screening of 3D-oids

Over the years, only a limited number of 2D and 3D imaging systems have been designed specifically for 3D-oids [166-175]. Among the developed systems, widefield and confocal fluorescence microscopy continue to be more widely used because they work with standard plate formats and are appropriate for routine screening workflows. However, widefield systems have limited penetration depth, despite their quick acquisition and smooth integration with microfluidic technologies [166], [167]. Confocal microscopy, on the other hand, offers subcellular resolution but at the expense of slower imaging rates and higher phototoxicity. Because of these drawbacks, confocal microscopy-based HCS systems usually use expensive, specialised imaging plates and generally smaller 3D models [168-170].

HCS systems designed for LSFM have become an effective option to overcome the imaging limitations and to achieve overall better results [171-175]. Complex 3D-oid structures in large samples can be examine due to the higher penetration depth and the ability to quickly acquire single-cell resolution volumes with much lower phototoxicity. However, LSFM-based methods have drawbacks as well, such as the requirement for specialised image processing pipelines, sample preparations,

hardware configurations, and imaging plates, which can restrict scalability and accessibility.

Building and designing a HCS compatible imaging system requires advanced knowledge including custom optics, sample holders, and alignment protocols. All of these making the process expensive and technically complex. As an alternative, creating a custom multiwell imaging plate for LSFM can improve throughput, lower manufacturing costs, and simplify integration, but it might limit flexibility in various setups [16], [175]. In general, many criteria must be taken into account when developing an HCS plate with broad applicability because a variety of factors can change imaging conditions. For example, samples can be as small as a few cells or as large as tiny organs, so 3D imaging shows a great deal of variation. Nevertheless, the obvious expectation of an HCS plate is that it can be used with automated pipetting systems and that it can allow the screening large numbers of samples whilst each item is separated. The plate must also have high optical qualities for imaging, compatibility with existing setups, flexible options for special cases, long-term imaging, reusability, and affordability and environmentally friendly manufacturing.

The next frontier in 3D HCS requires platforms based on modularity, transparency, and openness, whether through the development of innovative microscopy systems or the engineering of versatile imaging plates. Systems that can be quickly adapted to various biological contexts without compromising fidelity or throughput are required due to the inherent variability in 3D-oids, whether it be in size, morphology, or culture conditions.

6.5. Quantitative 3D image analysis for 3D cell cultures

Whilst 2D features proved to be an efficient way to get general information from complex objects, the 3D information is still needed for the in-depth analysis. Although several microscopy systems exist for 3D imaging, LSFM is one of the best tools to acquire high-quality 3D images, with low phototoxicity and fast acquisition time [78]. Even a new type of light-sheet method was introduced to reach single-cell resolution in relatively big tissue samples [82]. However, most LSFM setups have the same

limitations, which are the time-consuming sample embedding, less flexibility in terms of objective usage, and complex calibration processes that lead to the lack of HCS solutions. Furthermore, conventional imaging plates are not compatible with LSFM. Thus, to overcome these limitations and to elevate the number of screened objects within a day, the development of custom HCS imaging plates have started [16], [176-178]. Nevertheless, screening hundreds to thousands of 3D-oids holds limited significance without the ability to analyse the data effectively. As highlighted throughout this thesis, human assessment and interpretation of 3D data have fundamental limitations. Nonetheless, precise analytical methods can uncover critical insights that might otherwise remain undetected. It is important to note that there are many possible forms to analyse 3D-oids and the way we understand them is significantly influenced by the selected features for the analysis. For instance, 2D features give interpretable descriptions of a 3D model but give no structural information. Furthermore, using only a single 2D feature (*e.g. Diameter*, *Area*, *Volume*, *Circularity*) to describe spheroids is not adequate because both size and shape descriptors may include information regarding the outliers. Thus, the selection of an appropriate feature tends to change the outcome of the conclusion. A direct 2D and 3D comparison on spheroid models proved that for the accurate representation of spheroids' population requires at least a size and a shape-related feature [16]. Also, expecting the most similar spheroids that were selected based on their 2D properties is not realistic. Despite the limitation of the 2D features, pre-selection of 3D-oids still helps to remove strong outliers from the experiment.

Whilst 2D analysis of 3D-oids offers a simpler and faster evaluation, such analysis is not a precise representation of the data that may result in inconsistent findings. In particular, because cell type and ratio had a major impact on spheroid formation [179]. Although most 3D-oids may have irregular shapes that reduce overall predictability and comparability, perfectly spherical models are in fact best suited for estimating 3D properties. Providing more single cell related details about the specimen may take more time during the analysis. However, it could increase the precision of the evaluation, thus increasing the effectiveness of drug screening studies.

6.6. HCS-3D*X* platform

Over the past few years, the huge number of publications resulted in hundreds of unique methodological protocols for spheroid generation and imaging that largely slow down scientific advancement [99]. Furthermore, commercially available microscopy and image analysis tools often allow only specific use cases for a marginally higher price range. Keeping these challenges in mind, we started to work on the HCS-3D*X* project that required multidisciplinary efforts and a few years of development to establish an HCS system for 3D-oids [16]. During the development, we faced all the common issues starting from the spheroid generation to the image analysis that others are struggling with as well. In this thesis, most of the challenging aspects working with spheroid models were discussed to show possibilities and alternative solutions for several issues.

First, by reviewing the literature and emphasising the deficiency of minimum information for reproducibility, we addressed the issue of low reproducibility in spheroid-based experiments. The interlaboratory study demonstrated that even the most fundamental information could be crucial to enhancing laboratory transparency. The standardisation of procedures and protocols to promote reproducibility may be aided by the crowdsourcing knowledgebase. Second, we created a benchmarking tool to compare and objectively evaluate the performance of the optical clearing protocols in spheroid models. For different type of tumour spheroids, the optimal working protocols were determined by utilising the intensity variance metric. Third, we wanted to reduce the labour-intensive manual sample handling process of selecting and transferring spheroids by creating the SpheroidPicker system. Our aim was to increase throughput and reduce operator bias. Fourth, to enable high-resolution and scalable screening of 3D-oids, we created a specialised HCS multiwell imaging plate that is optimized for LSFM. Lastly, we developed an advanced image analysis pipeline that provides phenotypic profiling and quantification of spheroids at a single-cell level.

HCS-3D*X* is our versatile solution that combines AI-driven solutions with cutting-edge imaging methods like LSFM. The HCS-3D*X* system was tested on multiple experiments and we foresee its full potential in drug screening pipelines and in

personalised medicine approaches. Additionally, it might be an effective solution for the validation of newly developed 3D bioprinting models, where 3D structure is essential. In summary, the robustness of HCS-3DX makes it a flexible tool for academics and clinicians, opening the door for further advancements in biomedical research.

6.7. Future of 3D cell cultures

3D-oids are fundamental models and stand at the frontier of biomedical innovation, offering new avenues for discovery beyond the limits of traditional 2D cultures. Such models enable the creation of tissue like constructs and serve as models for investigating tissue development and disease. Despite the advantages, 3D-oids are more difficult to establish and handle than conventional 2D cell cultures because of their complexity. It is challenging to achieve reproducibility and consistency across experiments. Furthermore, the lab equipment and devices needed for 3D samples can be costly, and the methods frequently call for specific knowledge and expertise. Despite all the difficulties, 3D-oids are still frequently cited, and as technology advances, more and more study will demonstrate how useful these models are.

3D bioprinting, a technique that enables researchers to deposit layer-by-layer constructs of cells and biomaterials with high spatial precision, is driving the future of 3D cell culturing. Due to the possibility of high-precision designing and standardisation, bioprinting overcomes the two major limitations that still limit the extended usage of 3D-oids in clinical trials. Active research is being done on developing tissue-like structures, therefore, this technique holds promise for producing tissue tailored to each patient for regenerative medicine and disease modelling.

In parallel, new tissue-specific scaffolds and hydrogels will be crucial to the next wave of tissue engineering. Not just because 3D bioprinting heavily relies on the hydrogel-based bioinks but also because they bring us closer to long-term growing vascularized, innervated, and fully functional tissue constructs *in vitro,* which is not just for studying disease, but potentially for transplanting them.

For 3D-oids to reach their full potential and offer more profound insights into biological processes, it will be essential to integrate them with high-throughput screening systems combined with automated 3D analysis. Thus, robotic automation and AI-integrated platforms were envisioned to improve the scaling. In high-throughput culturing plates, robotic systems are being developed for basic purposes, such as liquid handling and plating cell suspension. These closed-loop systems can already improve reproducibility and free up important research time but are not ready for custom systems. Also, the automation of handling hydrogel-based systems like collagen and Matrigel will be a key issue in the near feature.

Imaging 3D-oids poses further complications. Fluorescence microscopy will remain a cornerstone of phenotypic analysis. Currently, 3D imaging methods are separated into two major categories: high penetration depth with slow acquisition and high-throughput imaging of small, live samples. Looking ahead, we may expect hybrid systems that combine deep imaging with real-time feedback to reconstruct high-resolution 3D images of living samples. Looking forward, we can envision even more refined techniques such as the integration of artificial intelligence and machine learning could accelerate the analysis of vast 3D imaging datasets and enhance predictive modelling of cell behaviours.

Despite these obstacles, momentum is building, and in our opinion, the community needs more early-stage multidisciplinary partnerships, methodology guidelines, improved communication, and better education. One of the reasons for the low number of clinically validated 3D-oid models is that they are not likely complex enough to accurately replicate *in vivo* physiology. Thus, it is our responsibility to improve methodological transparency, provide appropriate protocols for model generation and validation, improve screening possibilities, and develop better data analysis pipelines. Future directions focus strongly on organoid technology for personalised medicine, including alternatives to organ transplants and creating accurate tumour models derived from patient-specific stem cells. Ideas such as "organs-on-demand" that refers to the emerging ability to create transplantable human organs in the lab, have the potential to revolutionise transplantation and emergency medicine. Therefore, to encourage the adoption of standardised 3D assay methods, we advocate for industry and academics to work together to establish more clinically validated 3D-oid models.

7. Acknowledgements

I would like to express my deepest gratitude to my supervisor, Péter Horváth, for his unwavering support and guidance throughout my PhD journey. His willingness to share ideas and advice has been invaluable, helping me grow both as a scientist and as an individual.

I would like to express my sincere gratitude to Dr. Fruzsina Walter and Prof. Dr. Attila Gácser for proofreading my thesis and providing invaluable feedback.

My heartfelt appreciation goes to Filippo Piccinini, who guided me through the difficulties of publishing and always pushed me to achieve the best version of myself.

I am also sincerely thankful to past and present members of the BIOMAG group for the enriching discussions that have shaped my research. A special thanks to Tímea Tóth, Mária Harmati, Mária Kovács, István Grexa, and Dominik Hirling, whose kindness and encouragement made my transition into the group seamless. I truly appreciate the assistance of Ferenc Kovács and András Kriston, who always helped me.

I am also deeply thankful to Ildikó Szőts, Gergő Drabbant, Árpád Szilágyi, and Tibor Szöllősi for their encouragement over the years, keeping my spirits high through the challenges.

Finally, my profound gratitude goes to my family for their patience, love, and support throughout this journey. Their belief in me has been the foundation of my achievements.

Grants that supported our research: Lendület BIOMAG grant (no. 2018–342), TKP2021-EGA09, HUNRENTECH (TECH-2024-34), Horizon-BIALYMPH, Horizon-SYMMETRY, Horizon-SWEEPICS, H2020-Fair-CHARM, HAS-NAP3, the HUNTER-Excellence 2024, grant from OTKA-SNN no. 139455/ARRS, and OTKA-Excellence 2025.

8. Summary

2D cell cultures are still one of the most standard models for drug testing, but these models lack the ability to replicate the complexity of tissue structures and tumour microenvironments. In contrast, 3D-oids (spheroids, organoids, assembloids, etc.) have emerged as a more relevant approach, maintaining tissue-like structures and making them highly useful in many fields such as drug discovery, regenerative medicine, tumour biology, and immunotherapy.

Nearly 40,000 publications have been published since 2010, reflecting a significant increase in scientific interest in 3D-oids. Only a small number of these studies concentrate on creating standardised 3D HCS platforms, indicating significant challenges in this field. These challenges include the generation, handling, imaging, and analysis of 3D-oids that makes reproducibility difficult to achieve.

Although many different protocols and imaging setup exists, during our work with tumour spheroid models we encountered similar problems as often highlighted by the community. Therefore, starting from the generation of uniform spheroid models to the automated single-cell resolution analysis, we wanted to analyse each problematic point and come up with suggestions on how we can improve the current systems. In this thesis, a summarised version of these works is collected and written in a way to give an insight of our recent developments.

One of the most crucial challenges is the generation and the standardised reporting of 3D-oids related works. Protocols often missed crucial details that would greatly hinder reproducibility. Frequently overlooked details such as cell line, the composition of the culture medium, the formation method, and the size of the spheroids were not specifically reported or sometimes even missed in publications. Since in our work we especially focused on tumour spheroids, we joined in the MISpheroID consortium that published a crowdsourcing knowledgebase and defined a minimum set of experimental parameters to improve reproducibility for spheroids. We also did an interlaboratory experiment to raise attention to the effect of cell culture media in terms

of reproducibility on spheroids. Although MISpheroID was dedicated for spheroid models, the same guidelines would be accurate for other 3D-oids as well.

Optical clearing is an essential technique to improve the image quality by reducing light scattering within a 3D sample. Due to the high variety of samples and experimental conditions, numerous clearing methods were developed for tissue samples and 3D-oids, but no gold standard protocol was determined. In our next work, we publicly shared a high-resolution light-sheet fluorescence microscopy dataset that assisted in the evaluation of optical clearing techniques. Overall, 90 optically cleared multicellular spheroids were used, derived from 3 human carcinoma cell lines with similar morphology. The dataset was evaluated by 10 microscopy experts and based on the quality of the images, the experts assigned scores. We used the scores as a ground truth to distinguish the less effective and optimal methods. However, our conclusion was that the human evaluation alone is not sufficient to select the best optical clearing protocol. Then we compared the correlation between the experts and 7 no-reference sharpness metrics, and we found that intensity variance had the strongest positive correlation with the experts' assessment. Thus, using intensity variance, we evaluated all 3 cell lines and 5 optical clearing protocols, and the results indicated that the various spheroids responded differently to the tested optical clearing protocols. We proved that the optically cleared spheroid models can be quantitatively compared using intensity variance metric that we implemented as a Fiji plugin. In light of these findings, we support intensity variance as a reliable quantitative tool to assess the relative effectiveness of optical clearing protocols.

For the pre-selection and handling of spheroids, we developed SpheroidPicker that is an AI-guided automated 3D cell culture manipulator system. In this project, we had to integrate hardware and software solutions, combining a stereomicroscope, a custom micromanipulator, and a syringe pump that allowed us to transfer spheroids between various sample holders. Thanks to the AI-based segmentation method, we achieved reliable object detection with accurate 2D feature extraction. Furthermore, SpheroidPicker showed better consistency and precision in the pre-selection of spheroids, outperforming a human expert. The system was validated using the semi- or fully automated transferring methods on spheroid models that maintained their morphology and viability throughout the transfer process and showed no degradation

effect during the long-term experiments. In conclusion, the SpheroidPicker system makes it perfect for clinical studies, basic research, and high-throughput tests.

Since we achieved the single-cell resolution in relatively big tumour spheroids, our next step was to develop an HCS imaging plate for LSFM. We designed and created a working prototype for an HCS imaging plate that allows the screening of multiple spheroids where each sample is separated and has a predetermined position. The HCS plate has 5 elements: a mould element to form the FEP-foil; a vacuum-formed FEP-foil that has the unique cuvettes and separates the samples; a base element that holds the mounting media; an insert element that secures the position of the samples inside the cuvettes; and a grid element that secures the position of the FEP-foil. The plate has low production time and cost, and the possibility to produce the plate in-house. The 3D-printed elements are reusable and only the FEP-foil should be replaced between experiments. Furthermore, it can be used without any modification or adjustment with LSFM systems using the TwinFlect mirror versatile setup. The predetermined samples' position allows continuous automatic screening without the need to recalibrate the microscope that reduces the sample preparation and screening time. Finally, we defined the HCS plate within SpheroidPicker, which allows the automatic transfer of preselected spheroids into the plate. The plate has been used and validated in various experiments where we proved that it provides a substantially faster screening time whilst maintaining the same image quality.

In parallel to the HCS plate development, we realised that screening hundreds of spheroids holds limited significance without the proper data analysis. As the final step of our pipeline, we aimed to analyse spheroids at a single-cell level and compare the accuracy of the most commonly used 2D and 3D features. In addition, we also aimed to extend our understanding of spheroid models with structural information and cellular composition. For that, we used mono- and co-culture spheroids, imaged them both in 2D and 3D, applied segmentation and classification methods, and extracted 2D and 3D features. Working with hundreds of spheroids resulted in high morphological heterogeneity even though the models were generated using the same technique and repeated multiple times by the same experts. We also proved that the selection of an appropriate feature tends to influence the outcome of the analysis. For instance, using only a single 2D feature (*e.g. Diameter*, *Perimeter, Area*, *Volume*, *Circularity*) to

characterise spheroids is not adequate because both size and shape descriptors may include information regarding the outliers.

In conclusion, we proved that for an accurate representation of the spheroid's population it requires at least a size and a shape-related feature. According to the direct analysis, we showed that 2D shape descriptors consistently showed higher values, whilst the volume estimation resulted in lower values than the actual 3D volume. Nevertheless, spheroids with the most spherical shapes can be better estimated using only 2D features when 3D information is not available. However, spheroids with irregular shapes had lower predictability. Although it is not possible to select the most similar spheroids based on 2D features, we still accept and support 2D preselection of 3D-oids, particularly because it aids in eliminating strong outliers. By analysing the spheroid models at a single-cell level, we concluded that cell type and ratio had a major effect on spheroid formation, size, but not on shape.

This dedicated work resulted in the development of the HCS-3D*X* platform, which required interdisciplinary work to create an HCS system for 3D-oids. HCS-3D*X* was designed to allow accurate, automated, high-throughput single-cell analysis. This platform represents a breakthrough in 3D HCS by fusing AI-driven solutions with state-of-the-art imaging techniques like LSFM, offering a complete solution for complex *in vivo* models. The HCS-3D*X* system was tested on multiple experiments, and we anticipate that it will reach its full potential in personalised medicine and drug screening pipelines. Furthermore, it could be a useful way to validate recently created 3D bioprinting models, where 3D structure is crucial. In summary, the robustness of HCS-3D*X* makes it a flexible tool for academics and clinicians, opening the way for future developments in biomedical research.

9. Összefoglalás

A kétdimenziós (2D) sejtkultúrák még mindig az egyik legelterjedtebben használt modellek a gyógyszerkísérletekhez, ugyanakkor számos kutatás bebizonyította, hogy nem képesek a szöveti struktúrák és tumoros mikrokörnyezet komplexitásának reprodukálására. Ezzel szemben a háromdimenziós (3D) sejtkultúrákat relevánsabb modellként tartják számon, mivel képesek reprodukálni a szövetszerű mintázatokat, továbbá kiemelten jelentősek olyan területeken, mint a gyógyszerkutatás, a regeneratív orvoslás, a tumorbiológia vagy az immunterápia.

Az elmúlt 15 évben megközelítőleg mintegy 40.000 közlemény jelent meg 3D sejtkultúrákkal kapcsolatban, amely jelzi a feltörekvő modell iránti érdeklődést. Ugyanakkor ezen publikációknak csupán a töredéke foglalkozik a nagy áteresztőképességű rendszerek fejlesztésével, amely a terület újszerűsége mellet annak széleskörű kihívásaira utal. Ezen nehézségek közé tartozik többek között a minták nagyszámban történő előállítása, kezelése, detektálása és feldolgozása melyek együttesen hátráltatják a reprodukálhatóságot és automatizálást igényelnek.

Habár számtalan protokoll és képalkotó eljárás létezik, a szferoidokkal történő munkánk során számos, más laborokban egyaránt tapasztalt technikai problémával találkoztunk. Ezért a szferoid minták előállításától kezdve egészen az automatikus egysejt szintű képfeldolgozásig, ezen technikai kihívások áthidalására alkalmas eljárásokat fejlesztettünk. A tézis ezen munkák együttes összefoglalását tartalmazza, kitérve a legújabb fejlesztésekre és megoldásokra.

A 3D sejtkultúrák előállítása és standardizálása az egyik legtöbbször előforduló probléma. A publikált protokollok és kísérletek bemutatása számos esetben nem tartalmaz elegendő információt a reprodukálhatósághoz. Sok esetben olyan fontos részletek, mint például a felhasznált sejtvonal, a táptalaj összetétele, az előállítás módszere vagy akár a minta mérete pontatlanul vagy egyáltalán nincsenek közölve. Tumor szferoidokkal való munkánk során lehetőségünk nyílt csatlakozni a MISpheroID konzorciumhoz, mely létrehozott egy publikusan elérhető szferoid adatbázist. Az adatbázisba bármilyen szferoidokkal kapcsolatos kísérlet feltölthető a kötelező

minimum információk megadásával, ezzel segítve a kutatások átláthatóságát és reprodukálhatóságát. Ezzel párhuzamosan részt vettünk egy laboratóriumok közötti kísérletben, amelynek fő célja volt, hogy összehasonlítsuk a különböző laboratóriumokban előállított mintákat és kimutassuk a különböző tápoldatok hatását szferoid modelleken.

A 3D sejtkultúrák esetén a képalkotás nehézségekbe ütközhet a fokozott fénytörés következtében. A minták optikai tulajdonságainak módosításával viszont csökkenthetjük a fényszóródás hatását, amely javítja a képminőséget (a nemzetközi szaknyelvben ezt a módszert optikai clearing-nek nevezzük). Bár számos protokoll foglalkozik a minták törésmutatójának megváltoztatásával, összehasonlításukra és kiértékelésükre nincs egységes módszer/metrika. Munkánk során létrehoztunk és publikusan elérhetővé tettünk egy 3D képi adatbázist, amely 90 szferoidról készült egysejtszintű fluoreszcens 3D mikroszkópos felvételt tartalmaz. Összesen 3 különböző sejtvonalból hoztunk létre karcinóma szferoidokat (T-47D, Huh-7D12, 5-8F), melyeken 5 eltérő optikai clearing módszert (*Clear^{T}, Clear^{T2}, CUBIC, ScaleA2, Sucrose*) alkalmaztunk a kontroll minták mellett. Az adatbázisból válogatott reprezentatív képszeleteket a minőségük alapján 10 szakértő önállóan pontozta és kategorizálta, az optikai törésmutatót módosító kezelések összehasonlítása érdekében. Emellett 7 különböző élességmérési módszert is teszteltünk, melyek közül az intenzitás variancia mutatta a legjobb egyezést a szakértők pontozásával, így a továbbiakban a teljes, több mint 5000 képszeletet tartalmazó adatbázis kiértékeléséhez ezt a módszert használtuk és megállapítottuk, hogy a különböző optikai clearing módszerek eltérő hatékonysággal működtek az egyes szferoid modellek esetében, és ennek mértékét számszerűsíteni is tudtuk. Bebizonyítottuk, hogy az intenzitás variancia egy megfelelő módszer lehet a különböző törésmutatók kvantitatív kiértékelésére. Ezen eredmények fényében támogatjuk az intenzitás variancia módszer alkalmazását az optikai törésmutatót befolyásoló protokollok relatív hatékonyságának kiértékelésére.

A szferoidok automatikus morfológia-alapú kiválogatásához fejlesztettük az ún. SpheroidPicker pipettázó robotot, amely mesterséges intelligencia-alapú (MI) képanalízis módszerek révén képes a szferoidok detektálására és morfológiai analízisére, majd áthelyezi azokat a sejttenyésztő edényből a képalkotásra használt

mintatartóba. Ebben a projektben szoftveres és hardveres módszerek kombinációjára volt szükség a sztereó mikroszkóp, a mikromanipulátor és a fecskendő pumpa együttes vezérléséhez, amelyek a szferoidok felszívásáért és átpipettázásáért felelősek. A SpheroidPicker használatával lehetővé vált a hasonló morfológiájú szferoidok szakértők teljesítményét meghaladó, automatikus kigyűjtése. A rendszer képes teljesen automatizált működésre, ugyanakkor van lehetőség felhasználó vezérelt működtetésre is. A kiválogatott szferoidok mindkét esetben megőrizték morfológiájukat és életképességüket. Így a SpheroidPicker alkalmasnak bizonyult klinikai vizsgálatokhoz, alapkutatáshoz és nagy áteresztőképességű tesztekhez egyaránt.

A megfelelő képminőséget biztosító módszerek kidolgozását követően egy HCS képalkotó mintatartó lemez megtervezését tűztük ki célul, amely kompatibilis az általunk használt szelektív sík megvilágítású mikroszkóppal. 3D nyomtató és vákuum-fóliázó technológiák használatával előállítottuk a prototípust, amely lehetővé tette, hogy akár több mintát vizsgáljunk meg egyetlen lemezen. Ebben az esetben minden szferoid egymástól elválasztva, előre definiált pozícióban helyezkedik el. A mintatartó előállításához mindösszesen 5 különböző elemre van szükség: egy hőálló pozitív formára a vákuum-fóliázáshoz; a vákuum-fóliázással kialakított FEP-fóliára; egy rögzítő elemre, amely a minták pozícióját rögzíti a fóliában; egy váz elemre, amely a mintatartó keretét adja; és egy leszorító elemre, amely a fóliát rögzíti a vázhoz. A kifejlesztett és szabadalmaztatott mintatartó alacsony előállítási költsége és gyors előállítása lehetővé teszi a saját gyártást. Továbbá elegendő kizárólag a FEP-fóliát cserélni, minden más 3D nyomtatott elem sterilizálható és újrahasználható. A mintatartó használatához nem szükséges módosítani a szelektív sík megvilágítású mikroszkópot, amennyiben az rendelkezik a TwinFlect tükör megvilágítással. A minták automatizált detektálása kivitelezhető, nincs szükség mintánkénti kalibrálásra. Végezetül, a HCS mintatartó kompatibilis az általunk fejlesztett SpheroidPicker pipettázó robottal, amelynek köszönhetően a minták automatikus kiválasztása és áthelyezése szintén automatizálható. A mintatartó számos kísérletben volt tesztelve, ahol megállapítottuk, hogy lehetővé teszi a minták gyorsabb detektálását megfelelő képminőség mellett.

A mintatartó alkalmasnak bizonyult nagy mennyiségű képi adathalmaz előállítására. Ezért szükségessé vált egy olyan 3D képfeldolgozó folyamat fejlesztése, amely képes a szferoidok egysejt szintű elemzésére, vagyis 2D és 3D tulajdonság vektorok segítségével strukturális és akár sejt összetételi adatokat is eredményez. A szferoidok részletesebb vizsgálatához mono- és ko-kultúra tumor modelleket állítottunk elő, majd fénymikroszkóppal és szelektív sík megvilágítású mikroszkóppal is képfelvételeket készítettünk róluk, melyeket szegmentációs és klasszifikációs módszerek révén tulajdonság vektorok használatával elemeztünk. Vizsgálataink számszerűsítették a szferoid modellek közötti morfológiai varianciát, amely standard előállítási paraméterek mellett is nagymértékű volt. Kísérleteink arra utaltak, hogy a 3D kísérletek biológiai eredményei csak magas ismétlésszámok esetén lehetnek relevánsak. Továbbá vizuálisan szemléltettük, hogy a különböző morfológiai tulajdonságok használata befolyásolhatja az analízis kimenetelét. Felhívtuk a figyelmet arra is, hogy csupán egyetlen tulajdonság vektor használata, mint például az átmérő, a terület, a térfogat, vagy a köralakúság, nem elegendő a szferoidok jellemzéséhez és egy egységes mintahalmaz kiválogatásához. Ezért legalább egy mérettel és egy formával kapcsolatos tulajdonság vektor együttes használatát javasoltuk, mely alkalmasabb lehet különböző szferoid populációk összehasonlítására (például egy gyógyszertesztelési kísérletben), vagy az összehasonlító analízisek eredményeit potenciálisan torzító, szabálytalan morfológiájú szferoidok kiszűrésére is. Méréseink alapján azt tapasztaltuk, hogy a 2D tulajdonság vektorok, amelyek egyetlen fénymikroszkópos képfelvétel elemzésével keletkeztek, konzisztensen magasabb értékeket mutattak a szferoidok formáját illetően, ugyanakkor alacsonyabb értéket jeleztek a minták térfogata esetén a valós 3D eredményekhez képest. Továbbá megállapítottuk, hogy a 2D tulajdonságok kiterjesztése 3D mérésekre kizárólag a szabályosan gömbszerű objektumokra kivitelezhetőek, ha nem áll rendelkezésre valós 3D adat, mivel a szabálytalan alak jelentősen csökkenti a tulajdonságok prediktálhatóságát. Eredményeink alapján megállapítottuk, hogy a 2D tulajdonság vektorok, annak ellenére, hogy a legtöbb tanulmány csupán ezeket alkalmazza, nem elég precízek ahhoz, hogy következtetni tudjunk a valós 3D tulajdonságokra, ugyanakkor megfelelően alkalmazhatóak az erősen kiugró vagy eltérő minták megkülönböztetésére. Az egysejt szintű és strukturális tulajdonságok elemzése arra utalt, hogy a sejtek típusának és arányának jelentős szerepe van a szferoidok méretének meghatározásában, de nincs hatással az alaki tulajdonságokra. Ily módon

ahhoz, hogy releváns biológiai következtetéseket vonhassunk le, az egysejtszintű információk nem hagyhatók figyelmen kívül, például a napjainkban egyre nagyobb számban alkalmazott ko-kultúra modellek esetében.

Ezen interdiszciplináris projektek integrálásával létrehoztuk az ún. HCS-3D*X* platformot, amelyet specifikusan 3D sejtkultúrák létrehozására, kezelésére, képalkotására és automatikus vizsgálatára fejlesztettünk. A platform lehetővé tette az egysejt szintű precíz és automatizált munkafolyamatokat és ennek köszönhetően nagy számú minta feldolgozására alkalmas. A HCS-3D*X* platform egyik megkülönböztető jellege az MI alapú szoftveres támogatottság, továbbá a jó minőségű szelektív sík megvilágítású mikroszkópos detektálás. A rendszert számos különböző kísérletben teszteltük és legnagyobb hasznosítási potenciálját tekintve, főként a személyre szabott terápiák validálásában és drog szűrési kísérletekben lehet ígéretes. Továbbá alkalmas lehet a 3D bionyomtatással készült biológiai modellek analízisében, ahol döntő fontosságú a megfelelő szerkezet elemzése. Összefoglalva, a HCS-3D*X* platform széleskörű alkalmazhatósága új lehetőségeket biztosít mind az alap-, mind az alkalmazott kutatásban, sőt a 3D kultúrák egysejtszintű elemzésével a kutatás új dimenziója nyílhat meg, amely potenciálisan új interdiszciplináris kutatási területek kialakulását eredményezheti. Az MI adta lehetőségek kiaknázásával a korábbiaknál nagyságrendekkel nagyobb felbontású információkat nyerhetünk például a sejt-sejt kapcsolatok és a szöveti dinamika területén nemcsak a tumorkutatásokban, hanem számos más területen is, mint a szöveti regeneráció, embriológia, vagy az immunológia.

10. References

[1] N. Kramer *et al.*, “In vitro cell migration and invasion assays,” *Mutat. Res.*, vol. 752, no. 1, pp. 10–24, Jan-Mar 2013.

[2] C. Fischbach, H. J. Kong, S. X. Hsiong, M. B. Evangelista, W. Yuen, and D. J. Mooney, “Cancer cell angiogenic capability is regulated by 3D culture and integrin engagement,” *Proc. Natl. Acad. Sci. U. S. A.*, vol. 106, no. 2, pp. 399–404, Jan. 2009.

[3] S. Breslin and L. O’Driscoll, “Three-dimensional cell culture: the missing link in drug discovery,” *Drug Discov. Today*, vol. 18, no. 5–6, pp. 240–249, Mar. 2013.

[4] E. C. Costa, D. de M.-D. André F Moreira, V. M. Gaspar, M. P. Carvalho, and I. J. Correia, “3D tumor spheroids: an overview on the tools and techniques used for their analysis,” *Biotechnol. Adv.*, vol. 34, no. 8, pp. 1427–1441, Dec. 2016.

[5] O. Habanjar, M. Diab-Assaf, F. Caldefie-Chezet, and L. Delort, “3D Cell Culture Systems: Tumor Application, Advantages, and Disadvantages,” *Int. J. Mol. Sci.*, vol. 22, no. 22, Nov. 2021, doi: 10.3390/ijms222212200.

[6] L. D. Amer, A. Holtzinger, G. Keller, M. J. Mahoney, and S. J. Bryant, “Enzymatically degradable poly(ethylene glycol) hydrogels for the 3D culture and release of human embryonic stem cell derived pancreatic precursor cell aggregates,” *Acta Biomater.*, vol. 22, pp. 103–110, Aug. 2015.

[7] C. Liu *et al.*, “Potential effect of matrix stiffness on the enrichment of tumor initiating cells under three-dimensional culture conditions,” *Exp. Cell Res.*, vol. 330, no. 1, pp. 123–134, Jan. 2015.

[8] F. M. Kievit *et al.*, “Proliferation and enrichment of CD133(+) glioblastoma cancer stem cells on 3D chitosan-alginate scaffolds,” *Biomaterials*, vol. 35, no. 33, pp. 9137–9143, Nov. 2014.

[9] H. K. Kleinman, D. Philp, and M. P. Hoffman, “Role of the extracellular matrix in morphogenesis,” *Curr. Opin. Biotechnol.*, vol. 14, no. 5, pp. 526–532, Oct. 2003.

[10] F. Xu and K. J. L. Burg, “Three-dimensional polymeric systems for cancer cell studies,” *Cytotechnology*, vol. 54, no. 3, pp. 135–143, Jul. 2007.

[11] J. Debnath and J. S. Brugge, “Modelling glandular epithelial cancers in three-dimensional cultures,” *Nat. Rev. Cancer*, vol. 5, no. 9, pp. 675–688, Sep. 2005.

[12] J. Ro, J. Kim, and Y.-K. Cho, “Recent advances in spheroid-based microfluidic models to mimic the tumour microenvironment,” *Analyst*, vol. 147, no. 10, pp. 2023–2034, May 2022.

[13] K. Stock *et al.*, “Capturing tumor complexity in vitro: Comparative analysis of 2D and 3D tumor models for drug discovery,” *Sci. Rep.*, vol. 6, p. 28951, Jul. 2016.

[14] D. Sun, W. Gao, H. Hu, and S. Zhou, “Why 90% of clinical drug development fails and how to improve it?,” *Acta Pharm Sin B*, vol. 12, no. 7, pp. 3049–3062, Jul. 2022.

[15] H. Dowden and J. Munro, “Trends in clinical success rates and therapeutic focus,” *Nat. Rev. Drug Discov.*, vol. 18, no. 7, pp. 495–496, Jul. 2019.

[16] A. Diosdi *et al.*, “HCS-3DX, a next-generation AI-driven automated 3D high-content screening system,” *bioRxiv*, p. 2024.07.15.603536, Jul. 17, 2024. doi: 10.1101/2024.07.15.603536.

[17] I. Holen, F. Nutter, J. M. Wilkinson, C. A. Evans, P. Avgoustou, and P. D. Ottewell, “Human breast cancer bone metastasis in vitro and in vivo: a novel 3D model system for studies of tumour cell-bone cell interactions,” *Clin. Exp. Metastasis*, vol. 32, no. 7, pp. 689–702, Oct. 2015.

[18] T. Sethi *et al.*, “Extracellular matrix proteins protect small cell lung cancer cells against apoptosis: a mechanism for small cell lung cancer growth and drug resistance in vivo,” *Nat. Med.*, vol. 5, no. 6, pp. 662–668, Jun. 1999.

[19] E. Cukierman, R. Pankov, D. R. Stevens, and K. M. Yamada, “Taking cell-matrix adhesions to the third dimension,” *Science*, vol. 294, no. 5547, pp. 1708–1712, Nov. 2001.

[20] M. Bokhari, R. J. Carnachan, N. R. Cameron, and S. A. Przyborski, “Culture of HepG2

liver cells on three dimensional polystyrene scaffolds enhances cell structure and function during toxicological challenge," *J. Anat.*, vol. 211, no. 4, pp. 567–576, Oct. 2007.
[21] L. P. Ferreira, V. M. Gaspar, and J. F. Mano, "Design of spherically structured 3D in vitro tumor models -Advances and prospects," *Acta Biomater.*, vol. 75, pp. 11–34, Jul. 2018.
[22] J. Raitanen, B. Barta, M. Hacker, D. Georg, T. Balber, and M. Mitterhauser, "Comparison of Radiation Response between 2D and 3D Cell Culture Models of Different Human Cancer Cell Lines," *Cells*, vol. 12, no. 3, p. 360, Jan. 2023.
[23] S. A. Langhans, "Three-Dimensional in Vitro Cell Culture Models in Drug Discovery and Drug Repositioning," *Front. Pharmacol.*, vol. 9, p. 334617, Jan. 2018.
[24] F. Mittler, P. Obeïd, A. V. Rulina, V. Haguet, X. Gidrol, and M. Y. Balakirev, "High-Content Monitoring of Drug Effects in a 3D Spheroid Model," *Front. Oncol.*, vol. 7, p. 288955, Dec. 2017.
[25] F. Piccinini, I. D. Santis, and A. Bevilacqua, "Advances in cancer modeling: fluidic systems for increasing representativeness of large 3D multicellular spheroids," *Biotechniques*, vol. 65, no. 6, pp. 312–314, Dec. 2018.
[26] J. Ackermann, M. B. Amar, and J-F. Joanny "Multi-cellular aggregates, a model for living matter," *Phys. Rep.*, vol. 927, pp. 1–29, Sep. 2021.
[27] M. Zanoni *et al.*, "3D tumor spheroid models for in vitro therapeutic screening: a systematic approach to enhance the biological relevance of data obtained," *Sci. Rep.*, vol. 6, no. 1, pp. 1–11, Jan. 2016.
[28] B. W. M. T. J. Basnayake *et al.*, "Head and neck cancer patient-derived tumouroid cultures: opportunities and challenges," *Br. J. Cancer*, vol. 128, no. 10, pp. 1807–1818, Feb. 2023.
[29] I. Yakavets, A. Francois, A. Benoit, J.-L. Merlin, L. Bezdetnaya, and G. Vogin, "Advanced co-culture 3D breast cancer model for investigation of fibrosis induced by external stimuli: optimization study," *Sci. Rep.*, vol. 10, no. 1, pp. 1–11, Dec. 2020.
[30] L. Song *et al.*, "Assembly of Human Stem Cell-Derived Cortical Spheroids and Vascular Spheroids to Model 3-D Brain-like Tissues," *Sci. Rep.*, vol. 9, no. 1, pp. 1–16, Apr. 2019.
[31] M. Asmani *et al.*, "Fibrotic microtissue array to predict anti-fibrosis drug efficacy," *Nat. Commun.*, vol. 9, no. 1, pp. 1–12, May 2018.
[32] B. L. LeSavage, R. A. Suhar, N. Broguiere, M. P. Lutolf, and S. C. Heilshorn, "Next-generation cancer organoids," *Nat. Mater.*, vol. 21, no. 2, pp. 143–159, Aug. 2021.
[33] M. A. Lancaster and J. A. Knoblich, "Generation of cerebral organoids from human pluripotent stem cells," *Nat. Protoc.*, vol. 9, no. 10, pp. 2329–2340, Sep. 2014.
[34] E. Kim *et al.*, "Creation of bladder assembloids mimicking tissue regeneration and cancer," *Nature*, vol. 588, no. 7839, pp. 664–669, Dec. 2020.
[35] N. Vogt, "Assembloids," *Nat. Methods*, vol. 18, no. 1, pp. 27–27, Jan. 2021.
[36] B. V. Slaughter, S. S. Khurshid, O. Z. Fisher, A. Khademhosseini, and N. A. Peppas, "Hydrogels in regenerative medicine," *Adv. Mater.*, vol. 21, no. 32–33, pp. 3307–3329, Sep. 2009.
[37] J. Zhang, E. Wehrle, M. Rubert, and R. Müller, "3D Bioprinting of Human Tissues: Biofabrication, Bioinks, and Bioreactors," *Int. J. Mol. Sci.*, vol. 22, no. 8, Apr. 2021, doi: 10.3390/ijms22083971.
[38] A. C. Juraski *et al.*, "3D bioprinting for organ and organoid models and disease modeling," *Expert Opin. Drug Discov.*, vol. 18, no. 9, pp. 1043–1059, Jul. 2023.
[39] I. Matai, G. Kaur, A. Seyedsalehi, A. McClinton, and C. T. Laurencin, "Progress in 3D bioprinting technology for tissue/organ regenerative engineering," *Biomaterials*, vol. 226, p. 119536, Jan. 2020.
[40] T.-M. Achilli, J. Meyer, and J. R. Morgan, "Advances in the formation, use and understanding of multi-cellular spheroids," *Expert Opin. Biol. Ther.*, vol. 12, no. 10, pp. 1347–1360, Oct. 2012.
[41] D. Duguay, R. A. Foty, and M. S. Steinberg, "Cadherin-mediated cell adhesion and tissue segregation: qualitative and quantitative determinants," *Dev. Biol.*, vol. 253, no. 2,

pp. 309–323, Jan. 2003.
[42] N.-E. Ryu, S.-H. Lee, and H. Park, “Spheroid Culture System Methods and Applications for Mesenchymal Stem Cells,” *Cells*, vol. 8, no. 12, Dec. 2019, doi: 10.3390/cells8121620.
[43] A. Amann *et al.*, “Development of an innovative 3D cell culture system to study tumour--stroma interactions in non-small cell lung cancer cells,” *PLoS One*, vol. 9, no. 3, p. e92511, Mar. 2014.
[44] S. Gunti, A. T. K. Hoke, K. P. Vu, and N. R. London Jr, “Organoid and Spheroid Tumor Models: Techniques and Applications,” *Cancers* , vol. 13, no. 4, Feb. 2021, doi: 10.3390/cancers13040874.
[45] A. S. Nunes, A. S. Barros, E. C. Costa, A. F. Moreira, and I. J. Correia, “3D tumor spheroids as in vitro models to mimic in vivo human solid tumors resistance to therapeutic drugs,” *Biotechnol. Bioeng.*, vol. 116, no. 1, pp. 206–226, Jan. 2019.
[46] N. Rohwer and T. Cramer, “Hypoxia-mediated drug resistance: novel insights on the functional interaction of HIFs and cell death pathways,” *Drug Resist. Updat.*, vol. 14, no. 3, pp. 191–201, Jun. 2011.
[47] M. Pickl and C. H. Ries, “Comparison of 3D and 2D tumor models reveals enhanced HER2 activation in 3D associated with an increased response to trastuzumab,” *Oncogene*, vol. 28, no. 3, pp. 461–468, Jan. 2009.
[48] C. Ingeson-Carlsson, A. Martinez-Monleon, and M. Nilsson, “Differential effects of MAPK pathway inhibitors on migration and invasiveness of BRAF(V600E) mutant thyroid cancer cells in 2D and 3D culture,” *Exp. Cell Res.*, vol. 338, no. 2, pp. 127–135, Nov. 2015.
[49] S. Nath and G. R. Devi, “Three-dimensional culture systems in cancer research: Focus on tumor spheroid model,” *Pharmacol. Ther.*, vol. 163, pp. 94–108, Jul. 2016.
[50] K. Yanagihara, S. Uchida, S. Ohba, K. Kataoka, and K. Itaka, “Treatment of Bone Defects by Transplantation of Genetically Modified Mesenchymal Stem Cell Spheroids,” *Mol Ther Methods Clin Dev*, vol. 9, pp. 358–366, Jun. 2018.
[51] T. R. Olsen *et al.*, “Processing cellular spheroids for histological examination,” *J. Histotechnol.*, vol. 37, no. 4, pp. 138–142, Dec. 2014.
[52] O. Sirenko, T. Mitlo, J. Hesley, S. Luke, W. Owens, and E. F. Cromwell, “High-content assays for characterizing the viability and morphology of 3D cancer spheroid cultures,” *Assay Drug Dev. Technol.*, vol. 13, no. 7, pp. 402–414, Sep. 2015.
[53] H. R. Ueda *et al.*, “Tissue clearing and its applications in neuroscience,” *Nat. Rev. Neurosci.*, vol. 21, no. 2, pp. 61–79, Jan. 2020.
[54] J. Mertz, “Optical sectioning microscopy with planar or structured illumination,” *Nat. Methods*, vol. 8, no. 10, pp. 811–819, Sep. 2011.
[55] G. Lazzari *et al.*, “Light sheet fluorescence microscopy versus confocal microscopy: in quest of a suitable tool to assess drug and nanomedicine penetration into multicellular tumor spheroids,” *Eur. J. Pharm. Biopharm.*, vol. 142, pp. 195–203, Sep. 2019.
[56] D. S. Richardson and J. W. Lichtman, “Clarifying Tissue Clearing,” *Cell*, vol. 162, no. 2, pp. 246–257, Jul. 2015.
[57] E. C. Costa, D. N. Silva, A. F. Moreira, and I. J. Correia, “Optical clearing methods: An overview of the techniques used for the imaging of 3D spheroids,” *Biotechnol. Bioeng.*, vol. 116, no. 10, pp. 2742–2763, Oct. 2019.
[58] J. Seo, M. Choe, and S.-Y. Kim, “Clearing and Labeling Techniques for Large-Scale Biological Tissues,” *Mol. Cells*, vol. 39, no. 6, pp. 439–446, Jun. 2016.
[59] E. A. Genina, A. N. Bashkatov, and V. V. Tuchin, “Tissue optical immersion clearing,” *Expert Rev. Med. Devices*, Nov. 2010, doi: 10.1586/erd.10.50.
[60] T. Yu, Y. Qi, H. Gong, Q. Luo, and D. Zhu, “Optical clearing for multiscale biological tissues,” *J. Biophotonics*, vol. 11, no. 2, p. e201700187, Feb. 2018.
[61] E. Lee, H. J. Kim, and W. Sun, “See-Through Technology for Biological Tissue: 3-Dimensional Visualization of Macromolecules,” *Int. Neurourol. J.*, vol. 20, no. Suppl 1, pp. S15–22, May 2016.
[62] K. Tainaka, A. Kuno, S. I. Kubota, T. Murakami, and H. R. Ueda, “Chemical Principles in

Tissue Clearing and Staining Protocols for Whole-Body Cell Profiling," *Annu. Rev. Cell Dev. Biol.*, vol. 32, no. Volume 32, 2016, pp. 713–741, Oct. 2016.
[63] B. Mattei, R. B. Lira, K. R. Perez, and K. A. Riske, "Membrane permeabilization induced by Triton X-100: The role of membrane phase state and edge tension," *Chem. Phys. Lipids*, vol. 202, pp. 28–37, Jan. 2017.
[64] L. Silvestri, I. Costantini, L. Sacconi, and F. S. Pavone, "Clearing of fixed tissue: a review from a microscopist's perspective," *JBO*, vol. 21, no. 8, p. 081205, Mar. 2016.
[65] A. Feuchtinger, A. Walch, and M. Dobosz, "Deep tissue imaging: a review from a preclinical cancer research perspective," *Histochem. Cell Biol.*, vol. 146, no. 6, pp. 781–806, Oct. 2016.
[66] K. Chung *et al.*, "Structural and molecular interrogation of intact biological systems," *Nature*, vol. 497, no. 7449, pp. 332–337, Apr. 2013.
[67] A. Diosdi *et al.*, "A quantitative metric for the comparative evaluation of optical clearing protocols for 3D multicellular spheroids," *Comput. Struct. Biotechnol. J.*, vol. 19, pp. 1233–1243, Jan. 2021.
[68] A. Diosdi *et al.*, "Cell lines and clearing approaches: a single-cell level 3D light-sheet fluorescence microscopy dataset of multicellular spheroids," *Data Brief*, vol. 36, no. 107090, p. 107090, Jun. 2021.
[69] E. Blondeel *et al.*, "Sequential orthogonal assays for longitudinal and endpoint characterization of three-dimensional spheroids," *Nat. Protoc.*, Apr. 2025, doi: 10.1038/s41596-025-01150-y.
[70] N. Farahain *et al.*, "Three-dimensional Imaging and Scanning: Current and Future Applications for Pathology," *J. Pathol. Inform.*, vol. 8, no. 1, p. 36, Jan. 2017.
[71] E. H. K. Stelzer *et al.*, "Light sheet fluorescence microscopy," *Nature Reviews Methods Primers*, vol. 1, no. 1, pp. 1–25, Nov. 2021.
[72] F. Helmchen and W. Denk, "Deep tissue two-photon microscopy," *Nat. Methods*, vol. 2, no. 12, pp. 932–940, Dec. 2005.
[73] A. Aghigh, S. Bancelin, M. Rivard, M. Pinsard, H. Ibrahim, and F. Légaré, "Second harmonic generation microscopy: a powerful tool for bio-imaging," *Biophys. Rev.*, vol. 15, no. 1, pp. 43–70, Jan. 2023.
[74] L. Mostaço-Guidolin, N. L. Rosin, and T.-L. Hackett, "Imaging Collagen in Scar Tissue: Developments in Second Harmonic Generation Microscopy for Biomedical Applications," *Int. J. Mol. Sci.*, vol. 18, no. 8, p. 1772, Aug. 2017.
[75] J. Cheng, S. M. McMahon, D. W. Piston, and M. B. Jackson, "Comparing confocal and two-photon Ca2+ imaging of thin low-scattering preparations," *Biophysical Reports*, vol. 3, no. 2, p. 100109, Jun. 2023.
[76] P. Sahu and N. Mazumder, "Advances in adaptive optics–based two-photon fluorescence microscopy for brain imaging," *Lasers Med. Sci.*, vol. 35, no. 2, pp. 317–328, Nov. 2019.
[77] B. Weigelin, G.-J. Bakker, and P. Friedl, "Third harmonic generation microscopy of cells and tissue organization," *J. Cell Sci.*, vol. 129, no. 2, pp. 245–255, Jan. 2016.
[78] "Method of the Year 2014," *Nat. Methods*, vol. 12, no. 1, pp. 1–1, Dec. 2014.
[79] A. H. Voie, D. H. Burns, and F. A. Spelman, "Orthogonal-plane fluorescence optical sectioning: Three-dimensional imaging of macroscopic biological specimens," *J. Microsc.*, vol. 170, no. 3, pp. 229–236, Jun. 1993.
[80] J. M. Heddleston and T.-L. Chew, "Light sheet microscopes: Novel imaging toolbox for visualizing life's processes," *Int. J. Biochem. Cell Biol.*, vol. 80, pp. 119–123, Nov. 2016.
[81] C. M. Hobson, M. Guo, H. D. Vishwasrao, Y. Wu, H. Shroff, and T.-L. Chew, "Practical considerations for quantitative light sheet fluorescence microscopy," *Nat. Methods*, vol. 19, no. 12, pp. 1538–1549, Oct. 2022.
[82] L. Tang *et al.*, "Curved light sheet microscopy for centimetre-scale cleared tissue imaging," *Nat. Photonics*, vol. 19, no. 6, pp. 577–584, Jun. 2025.
[83] N. Carragher, F. Piccinini, A. Tesei, O. J. T. Jr, M. Bickle, and P. Horvath, "Concerns, challenges and promises of high-content analysis of 3D cellular models," *Nat. Rev. Drug Discov.*, vol. 17, no. 8, pp. 606–606, Jul. 2018.

[84] M. A. Borten, S. S. Bajikar, N. Sasaki, H. Clevers, and K. A. Janes, “Automated brightfield morphometry of 3D organoid populations by OrganoSeg,” *Sci. Rep.*, vol. 8, no. 1, p. 5319, Mar. 2018.
[85] F. Piccinini, “AnaSP: a software suite for automatic image analysis of multicellular spheroids,” *Comput. Methods Programs Biomed.*, vol. 119, no. 1, pp. 43–52, Apr. 2015.
[86] C. Z. Eddy, A. Naylor, C. T. Cunningham, and B. Sun, “Facilitating cell segmentation with the projection-enhancement network,” *Phys. Biol.*, vol. 20, no. 6, Oct. 2023, doi: 10.1088/1478-3975/acfe53.
[87] M. Barbier *et al.*, “Ellipsoid segmentation model for analyzing light-attenuated 3D confocal image stacks of fluorescent multi-cellular spheroids,” *PLoS One*, vol. 11, no. 6, p. e0156942, Jun. 2016.
[88] R. Hollandi *et al.*, “nucleAIzer: A Parameter-free Deep Learning Framework for Nucleus Segmentation Using Image Style Transfer,” *Cell Syst*, vol. 10, no. 5, pp. 453–458.e6, May 2020.
[89] K. McDole *et al.*, “In Toto imaging and reconstruction of post-implantation mouse development at the single-cell level,” *Cell*, vol. 175, no. 3, pp. 859–876.e33, Oct. 2018.
[90] P. P. Shinde and S. Shah, “A review of machine learning and deep learning applications,” in *2018 Fourth International Conference on Computing Communication Control and Automation (ICCUBEA)*, IEEE, Aug. 2018. doi: 10.1109/iccubea.2018.8697857.
[91] A. Shadmani, M. R. Nikoo, A. H. Gandomi, R.-Q. Wang, and B. Golparvar, “A review of machine learning and deep learning applications in wave energy forecasting and WEC optimization,” *Energy Strategy Reviews*, vol. 49, p. 101180, Sep. 2023.
[92] X. Ying, “An Overview of Overfitting and its Solutions,” *J. Phys. Conf. Ser.*, vol. 1168, p. 022022, Feb. 2019.
[93] H. Kaur, H. Nori, S. Jenkins, R. Caruana, H. Wallach, and J. Wortman Vaughan, “Interpreting interpretability: Understanding data scientists’ use of interpretability tools for machine learning,” in *Proceedings of the 2020 CHI Conference on Human Factors in Computing Systems*, New York, NY, USA: ACM, Apr. 2020. doi: 10.1145/3313831.3376219.
[94] E. Moen, D. Bannon, T. Kudo, W. Graf, M. Covert, and D. Van Valen, “Deep learning for cellular image analysis,” *Nat. Methods*, vol. 16, no. 12, pp. 1233–1246, Dec. 2019.
[95] K. He, X. Zhang, S. Ren, and J. Sun, “Deep residual learning for image recognition,” in *2016 IEEE Conference on Computer Vision and Pattern Recognition (CVPR)*, IEEE, Jun. 2016. doi: 10.1109/cvpr.2016.90.
[96] K. Weiss, T. M. Khoshgoftaar, and D. Wang, “A survey of transfer learning,” *J. Big Data*, vol. 3, no. 1, Dec. 2016, doi: 10.1186/s40537-016-0043-6.
[97] X. Mei *et al.*, “RadImageNet: An open radiologic deep learning research dataset for effective transfer learning,” *Radiol. Artif. Intell.*, vol. 4, no. 5, p. e210315, Sep. 2022.
[98] M. Kapałczyńska *et al.*, “2D and 3D cell cultures – a comparison of different types of cancer cell cultures,” *Arch. Med. Sci.*, vol. 14, no. 4, pp. 910–919, Jun. 2018.
[99] A. Peirsman *et al.*, “MISpheroID: a knowledgebase and transparency tool for minimum information in spheroid identity,” *Nat. Methods*, vol. 18, no. 11, pp. 1294–1303, Nov. 2021.
[100] K. N. Bergdorf *et al.*, “Immunofluorescent staining of cancer spheroids and fine-needle aspiration-derived organoids,” *STAR Protocols*, vol. 2, no. 2, p. 100578, Jun. 2021.
[101] I. Grexa *et al.*, “SpheroidPicker for automated 3D cell culture manipulation using deep learning,” *Sci. Rep.*, vol. 11, no. 1, pp. 1–11, Jul. 2021.
[102] V. Zieger *et al.*, “Towards Automation in 3D Cell Culture: Selective and Gentle High-Throughput Handling of Spheroids and Organoids via Novel Pick-Flow-Drop Principle,” *Adv. Healthc. Mater.*, vol. 13, no. 9, p. 2303350, Apr. 2024.
[103] A. Diosdi *et al.*, “HCS-3D*X*, a next-generation AI-driven automated 3D high-content screening system,” *bioRxiv*, Jul. 17, 2024. doi: 10.1101/2024.07.15.603536.
[104] T. Riss and O. J. Trask Jr, “Factors to consider when interrogating 3D culture models with plate readers or automated microscopes,” *In Vitro Cell. Dev. Biol. Anim.*, vol. 57,

no. 2, pp. 238–256, Feb. 2021.
[105] S. J. Han, S. Kwon, and K. S. Kim, “Challenges of applying multicellular tumor spheroids in preclinical phase,” *Cancer Cell Int.*, vol. 21, no. 1, p. 152, Mar. 2021.
[106] G. Mehta, A. Y. Hsiao, M. Ingram, G. D. Luker, and S. Takayama, “Opportunities and challenges for use of tumor spheroids as models to test drug delivery and efficacy,” *J. Control. Release*, vol. 164, no. 2, pp. 192–204, Dec. 2012.
[107] F. Monjaret, M. Fernandes, E. Duchemin-Pelletier, A. Argento, S. Degot, and J. Young, “Fully automated one-step production of functional 3D tumor spheroids for high-content screening,” *J. Lab. Autom.*, vol. 21, no. 2, pp. 268–280, Apr. 2016.
[108] M. B. Cutrona and J. C. Simpson, “A high-throughput automated confocal microscopy platform for quantitative phenotyping of nanoparticle uptake and transport in spheroids,” *Small*, vol. 15, no. 37, p. e1902033, Sep. 2019.
[109] J. Kriston-Vizi and H. Flotow, “Getting the whole picture: High content screening using three-dimensional cellular model systems and whole animal assays,” *Cytometry A*, vol. 91, no. 2, pp. 152–159, Feb. 2017.
[110] A. S. Chalkley, M. M. Mysior, and J. C. Simpson, “A robust method for the large-scale production of spheroids for high-content screening and analysis applications,” *J. Vis. Exp.*, no. 178, Dec. 2021, doi: 10.3791/63436.
[111] L. Li, Q. Zhou, T. C. Voss, K. L. Quick, and D. V. LaBarbera, “High-throughput imaging: Focusing in on drug discovery in 3D,” *Methods*, vol. 96, pp. 97–102, Mar. 2016.
[112] J. F. Dekkers *et al.*, “High-resolution 3D imaging of fixed and cleared organoids,” *Nat. Protoc.*, vol. 14, no. 6, pp. 1756–1771, Jun. 2019.
[113] H. Kolesová, M. Čapek, B. Radochová, J. Janáček, and D. Sedmera, “Comparison of different tissue clearing methods and 3D imaging techniques for visualization of GFP-expressing mouse embryos and embryonic hearts,” *Histochem. Cell Biol.*, vol. 146, no. 2, pp. 141–152, Aug. 2016.
[114] I. Smyrek and E. H. K. Stelzer, “Quantitative three-dimensional evaluation of immunofluorescence staining for large whole mount spheroids with light sheet microscopy,” *Biomed. Opt. Express*, vol. 8, no. 2, pp. 484–499, Feb. 2017.
[115] E. C. Costa, A. F. Moreira, D. de Melo-Diogo, and I. J. Correia, “Polyethylene glycol molecular weight influences the ClearT2 optical clearing method for spheroids imaging by confocal laser scanning microscopy,” *J. Biomed. Opt.*, vol. 23, no. 5, pp. 1–11, May 2018.
[116] E. C. Costa, A. F. Moreira, D. de Melo-Diogo, and I. J. Correia, “ClearT immersion optical clearing method for intact 3D spheroids imaging through confocal laser scanning microscopy,” *Opt. Laser Technol.*, vol. 106, pp. 94–99, Oct. 2018.
[117] N. Ansari, S. Müller, E. H. K. Stelzer, and F. Pampaloni, “Quantitative 3D cell-based assay performed with cellular spheroids and fluorescence microscopy,” *Methods Cell Biol.*, vol. 113, pp. 295–309, 2013.
[118] P. Klaka *et al.*, “A novel organotypic 3D sweat gland model with physiological functionality,” *PLoS One*, vol. 12, no. 8, p. e0182752, Aug. 2017.
[119] E. Nürnberg *et al.*, “Routine optical clearing of 3D-cell cultures: Simplicity forward,” *Front. Mol. Biosci.*, vol. 7, p. 20, Feb. 2020.
[120] M. E. Boutin, T. C. Voss, S. A. Titus, K. Cruz-Gutierrez, S. Michael, and M. Ferrer, “A high-throughput imaging and nuclear segmentation analysis protocol for cleared 3D culture models,” *Sci. Rep.*, vol. 8, no. 1, p. 11135, Jul. 2018.
[121] R. Hollandi *et al.*, “When the pen is mightier than the sword: semi-automatic 2 and 3D image labelling,” *bioRxiv*, Jan. 16, 2024. doi: 10.1101/2024.01.15.575658.
[122] F. Piccinini and A. Diosdi, “2020_Diosdi_ClearedSpheroids.” figshare, Jul. 07, 2020. doi: 10.6084/M9.FIGSHARE.12620078.V1.
[123] K. Froehlich *et al.*, “Generation of multicellular breast cancer tumor spheroids: Comparison of different protocols,” *J. Mammary Gland Biol. Neoplasia*, vol. 21, no. 3–4, pp. 89–98, Dec. 2016.
[124] K.-H. Lee and T.-H. Kim, “Recent advances in multicellular tumor spheroid generation for drug screening,” *Biosensors (Basel)*, vol. 11, no. 11, p. 445, Nov. 2021.

[125] D. Liu, S. Chen, and M. Win Naing, “A review of manufacturing capabilities of cell spheroid generation technologies and future development,” *Biotechnol. Bioeng.*, vol. 118, no. 2, pp. 542–554, Feb. 2021.
[126] A. Mund *et al.*, “Deep Visual Proteomics defines single-cell identity and heterogeneity,” *Nat. Biotechnol.*, vol. 40, no. 8, pp. 1231–1240, Aug. 2022.
[127] R. Hollandi, Á. Diósdi, G. Hollandi, N. Moshkov, and P. Horváth, “AnnotatorJ: an ImageJ plugin to ease hand annotation of cellular compartments,” *Mol. Biol. Cell*, vol. 31, no. 20, pp. 2179–2186, Sep. 2020.
[128] O. Ronneberger, P. Fischer, and T. Brox, “U-Net: Convolutional Networks for Biomedical Image Segmentation,” in *Lecture Notes in Computer Science*, in Lecture notes in computer science. , Cham: Springer International Publishing, 2015, pp. 234–241.
[129] K. He, G. Gkioxari, P. Dollar, and R. Girshick, “Mask R-CNN,” in *2017 IEEE International Conference on Computer Vision (ICCV)*, IEEE, Oct. 2017. doi: 10.1109/iccv.2017.322.
[130] K. Hötte *et al.*, “Ultra-thin fluorocarbon foils optimise multiscale imaging of three-dimensional native and optically cleared specimens,” *Sci. Rep.*, vol. 9, no. 1, p. 17292, Nov. 2019.
[131] A. Diosdi *et al.*, “Single-cell light-sheet fluorescence 3D images of tumour-stroma spheroid multicultures,” *Sci. Data*, vol. 12, no. 1, p. 492, Mar. 2025.
[132] A. Niederlein, F. Meyenhofer, D. White, and M. Bickle, “Image analysis in high-content screening,” *Comb. Chem. High Throughput Screen.*, vol. 12, no. 9, pp. 899–907, Nov. 2009.
[133] F. Piccinini, A. Tesei, M. Zanoni, and A. Bevilacqua, “ReViMS: Software tool for estimating the volumes of 3-D multicellular spheroids imaged using a light sheet fluorescence microscope,” *Biotechniques*, vol. 63, no. 5, pp. 227–229, Nov. 2017.
[134] X. Ruan *et al.*, “Image processing tools for petabyte-scale light sheet microscopy data,” *Nat. Methods*, vol. 21, no. 12, pp. 2342–2352, Dec. 2024.
[135] G. de Medeiros *et al.*, “Multiscale light-sheet organoid imaging framework,” *Nat. Commun.*, vol. 13, no. 1, p. 4864, Aug. 2022.
[136] H. J. Hwang, M.-S. Oh, D. W. Lee, and H.-J. Kuh, “Multiplex quantitative analysis of stroma-mediated cancer cell invasion, matrix remodeling, and drug response in a 3D co-culture model of pancreatic tumor spheroids and stellate cells,” *J. Exp. Clin. Cancer Res.*, vol. 38, no. 1, p. 258, Jun. 2019.
[137] Z. Sumbalova Koledova, “3D Cell Culture: Techniques for and beyond organoid applications,” *Methods Mol. Biol.*, vol. 2764, pp. 1–12, 2024.
[138] S. P. Pașca, “The rise of three-dimensional human brain cultures,” *Nature*, vol. 553, no. 7689, pp. 437–445, Jan. 2018.
[139] R. Polak, E. T. Zhang, and C. J. Kuo, “Cancer organoids 2.0: modelling the complexity of the tumour immune microenvironment,” *Nat. Rev. Cancer*, vol. 24, no. 8, pp. 523–539, Aug. 2024.
[140] L. Neufeld, E. Yeini, S. Pozzi, and R. Satchi-Fainaro, “3D bioprinted cancer models: from basic biology to drug development,” *Nat. Rev. Cancer*, vol. 22, no. 12, pp. 679–692, Dec. 2022.
[141] S. V. Murphy and A. Atala, “3D bioprinting of tissues and organs,” *Nat. Biotechnol.*, vol. 32, no. 8, pp. 773–785, Aug. 2014.
[142] S. V. Murphy, P. De Coppi, and A. Atala, “Opportunities and challenges of translational 3D bioprinting,” *Nat. Biomed. Eng.*, vol. 4, no. 4, pp. 370–380, Apr. 2020.
[143] C. Mukhopadhyay and M. K. Paul, “Organoid-based 3D in vitro microphysiological systems as alternatives to animal experimentation for preclinical and clinical research,” *Arch. Toxicol.*, vol. 97, no. 5, pp. 1429–1431, May 2023.
[144] A. Mukherjee, A. Sinha, M. Maibam, B. Bisht, and M. K. Paul, “Organoids and Commercialization,” in *Biomedical Engineering*, IntechOpen, 2022.
[145] S. Zhu *et al.*, “Influence of experimental variables on spheroid attributes,” *Sci. Rep.*, vol. 15, no. 1, p. 9751, Mar. 2025.

[146] E. Blondeel *et al.*, “The Spheroid Light Microscopy Image Atlas for morphometrical analysis of three-dimensional cell cultures,” *Sci. Data*, vol. 12, no. 1, p. 283, Feb. 2025.
[147] X. Liang and H. Luo, “Optical tissue clearing: Illuminating brain function and dysfunction,” *Theranostics*, vol. 11, no. 7, pp. 3035–3051, Jan. 2021.
[148] M. Campbell-Thompson and S.-C. Tang, “Pancreas optical clearing and 3-D microscopy in health and diabetes,” *Front. Endocrinol. (Lausanne)*, vol. 12, p. 644826, Apr. 2021.
[149] Z. Ou *et al.*, “Achieving optical transparency in live animals with absorbing molecules,” *Science*, vol. 385, no. 6713, p. eadm6869, Sep. 2024.
[150] A. Banerjee, A. Indoliya, and R. Poddar, “Edible oil based optical clearing for optical coherence tomography angiography imaging,” *Microvasc. Res.*, vol. 154, no. 104671, p. 104671, Jul. 2024.
[151] W. H. Abuwatfa, W. G. Pitt, and G. A. Husseini, “Scaffold-based 3D cell culture models in cancer research,” *J. Biomed. Sci.*, vol. 31, no. 1, p. 7, Jan. 2024.
[152] M. Cortesi, K. Warton, and C. E. Ford, “Beyond 2D cell cultures: how 3D models are changing the *in vitro* study of ovarian cancer and how to make the most of them,” *PeerJ*, vol. 12, no. e17603, p. e17603, Aug. 2024.
[153] A. Marchini and F. Gelain, “Synthetic scaffolds for 3D cell cultures and organoids: applications in regenerative medicine,” *Crit. Rev. Biotechnol.*, vol. 42, no. 3, pp. 468–486, Apr. 2022.
[154] A. C. Daly, M. D. Davidson, and J. A. Burdick, “3D bioprinting of high cell-density heterogeneous tissue models through spheroid fusion within self-healing hydrogels,” *Nat. Commun.*, vol. 12, no. 1, p. 753, Feb. 2021.
[155] M. H. Kim *et al.*, “High-throughput bioprinting of spheroids for scalable tissue fabrication,” *Nat. Commun.*, vol. 15, no. 1, p. 10083, Nov. 2024.
[156] C. M. Leung *et al.*, “A guide to the organ-on-a-chip,” *Nat. Rev. Methods Primers*, vol. 2, no. 1, May 2022, doi: 10.1038/s43586-022-00118-6.
[157] P. Guerrero-López *et al.*, “2D versus 3D tumor-on-chip models to study the impact of tumor organization on metabolic patterns in vitro,” *Sci. Rep.*, vol. 15, no. 1, p. 19506, Jun. 2025.
[158] R. S. Schneider *et al.*, “On-chip 3D potency assay for prediction of clinical outcomes for cell therapy candidates for osteoarthritis,” *Nat. Commun.*, vol. 16, no. 1, p. 4915, May 2025.
[159] A. Akshay *et al.*, “SpheroScan: a user-friendly deep learning tool for spheroid image analysis,” *Gigascience*, vol. 12, Dec. 2022, doi: 10.1093/gigascience/giad082.
[160] T. K. N. Ngo *et al.*, “A deep learning-based pipeline for analyzing the influences of interfacial mechanochemical microenvironments on spheroid invasion using differential interference contrast microscopic images,” *Mater. Today Bio*, vol. 23, no. 100820, p. 100820, Dec. 2023.
[161] A. S. Shahbazi, F. Irandoost, R. Mahdavian, S. Shojaeilangari, A. Allahvardi, and H. Naderi-Manesh, “A multi-stage weakly supervised design for spheroid segmentation to explore mesenchymal stem cell differentiation dynamics,” *BMC Bioinformatics*, vol. 26, no. 1, p. 20, Jan. 2025.
[162] F. Oudouar *et al.*, “An empirical evaluation of neural network architectures for 3D spheroid segmentation,” *Computers*, vol. 14, no. 3, p. 86, Feb. 2025.
[163] J. E. Urrutia Gómez *et al.*, “Highly parallel and high-throughput nanoliter-scale liquid, cell, and spheroid manipulation on droplet microarray,” *Adv. Funct. Mater.*, vol. 35, no. 1, Jan. 2025, doi: 10.1002/adfm.202410355.
[164] M. Trossbach, E. Åkerlund, K. Langer, B. Seashore-Ludlow, and H. N. Joensson, “High-throughput cell spheroid production and assembly analysis by microfluidics and deep learning,” *SLAS Technol.*, vol. 28, no. 6, pp. 423–432, Dec. 2023.
[165] I. Stepanov *et al.*, “Low-cost robotic manipulation of live microtissues for cancer drug testing,” *Sci. Adv.*, vol. 11, no. 20, p. eads1631, May 2025.

[166] H. J. Hwang, M.-S. Oh, D. W. Lee, and H.-J. Kuh, “Multiplex quantitative analysis of stroma-mediated cancer cell invasion, matrix remodeling, and drug response in a 3D co-culture model of pancreatic tumor spheroids and stellate cells,” J. Exp. Clin. Cancer Res., vol. 38, no. 1, p. 258, Jun. 2019.
[167] J. G. Delinasios et al., “Proliferating fibroblasts and HeLa cells co-cultured in vitro reciprocally influence growth patterns, protein expression, chromatin features and cell survival,” Anticancer Res., vol. 35, no. 4, pp. 1881–1916, Apr. 2015.
[168] X. Li et al., “Intravoxel incoherent motion MR imaging of early cervical carcinoma: correlation between imaging parameters and tumor-stroma ratio,” Eur. Radiol., vol. 28, no. 5, pp. 1875–1883, May 2018.
[169] F. Mittler, P. Obeïd, A. V. Rulina, V. Haguet, X. Gidrol, and M. Y. Balakirev, “High-Content Monitoring of Drug Effects in a 3D Spheroid Model,” Front Oncol, vol. 7, p. 293, Dec. 2017.
[170] S.-Y. Lee, I. Doh, D.-H. Nam, and D. W. Lee, “3D Cell-Based High-Content Screening (HCS) Using a Micropillar and Microwell Chip Platform,” Anal Chem, vol. 90, no. 14, pp. 8354–8361, Jul. 2018.
[171] N. Sandström *et al.*, “Miniaturized and multiplexed high-content screening of drug and immune sensitivity in a multichambered microwell chip,” Cell Reports Methods, vol. 2, no. 7, p. 100256, Jul. 2022.
[172] M. B. Cutrona and J. C. Simpson, “A high-throughput automated confocal microscopy platform for quantitative phenotyping of nanoparticle uptake and transport in spheroids,” Small, vol. 15, no. 37, p. e1902033, Sep. 2019.
[173] R. Muckom et al., “High-throughput 3D screening for differentiation of hPSC-derived cell therapy candidates,” Sci Adv, vol. 6, no. 32, p. eaaz1457, Aug. 2020.
[174] S. B. Bozal *et al.*, “Development of an automated 3D high content cell screening platform for organoid phenotyping,” SLAS Discovery, vol. 29, no. 7, p. 100182, Oct. 2024.
[175] A. Beghin et al., “Automated high-speed 3D imaging of organoid cultures with multi-scale phenotypic quantification,” Nature Methods, vol. 19, no. 7, pp. 881–892, Jun. 2022.
[176] B. Eismann *et al.*, “Automated 3D light-sheet screening with high spatiotemporal resolution reveals mitotic phenotypes,” *J. Cell Sci.*, vol. 133, no. 11, p. jcs245043, Jun. 2020.
[177] A. Beghin *et al.*, “Automated high-speed 3D imaging of organoid cultures with multi-scale phenotypic quantification,” *Nat. Methods*, vol. 19, no. 7, pp. 881–892, Jul. 2022.
[178] S. De Beuckeleer *et al.*, “An agarose fluidic chip for high-throughput in toto organoid imaging,” *Lab Chip*, vol. 25, no. 2, pp. 235–252, Jan. 2025.
[179] J. G. Delinasios *et al.*, “Proliferating fibroblasts and HeLa cells co-cultured in vitro reciprocally influence growth patterns, protein expression, chromatin features and cell survival,” *Anticancer Res.*, vol. 35, no. 4, pp. 1881–1916, Apr. 2015.

11. Supplementary

a

Experts' score

	Uncleared	Clear^{T}	Clear^{T2}	CUBIC	ScaleA2	Sucrose	
T-47D	3.52	3.72	3.68	3.72	3.36	4.04	Top
	4.32	3.64	4.04	4.84	4.52	4.64	Middle
	2.72	2.60	2.92	3.88	3.28	3.60	Bottom
5-8F	3.24	3.20	2.92	3.56	3.76	3.60	Top
	3.60	3.00	3.24	4.80	4.68	4.28	Middle
	1.84	1.48	1.76	3.56	3.44	2.84	Bottom
Huh-7D12	3.00	2.80	2.84	3.32	3.00	3.36	Top
	2.28	1.92	2.20	3.00	2.88	3.88	Middle
	1.12	1.00	1.20	1.40	1.44	2.72	Bottom

b

Intensity v. (internal circle)

	Uncleared	Clear^{T}	Clear^{T2}	CUBIC	ScaleA2	Sucrose	
T-47D	1.71	2.52	2.02	2.26	2.62	1.97	Top
	1.35	1.84	1.70	2.66	2.64	2.48	Middle
	1.26	1.51	1.47	2.54	2.02	2.38	Bottom
5-8F	1.43	1.76	1.63	1.79	2.26	1.72	Top
	1.24	1.34	1.29	1.95	2.79	1.93	Middle
	1.10	1.10	1.11	1.77	2.08	1.65	Bottom
Huh-7D12	1.38	1.71	1.51	1.68	2.03	1.86	Top
	1.05	1.09	1.15	1.29	1.45	1.85	Middle
	1.02	1.04	1.05	1.12	1.19	1.92	Bottom

1 3 5

Supplementary figure 1. The experts' scores and the intensity variance internal circle scores are represented as a heatmap. (a) The heatmap shows the average evaluation scores for the ten experts. The experts evaluated five spheroids from each group, evaluating only one image per region. (b) In contrast, five spheroids from each group were evaluated using the intensity variance metric (with the internal circle option) to determine the quality assessment. In this case, the metric evaluated each image from each region and the average scores were used.

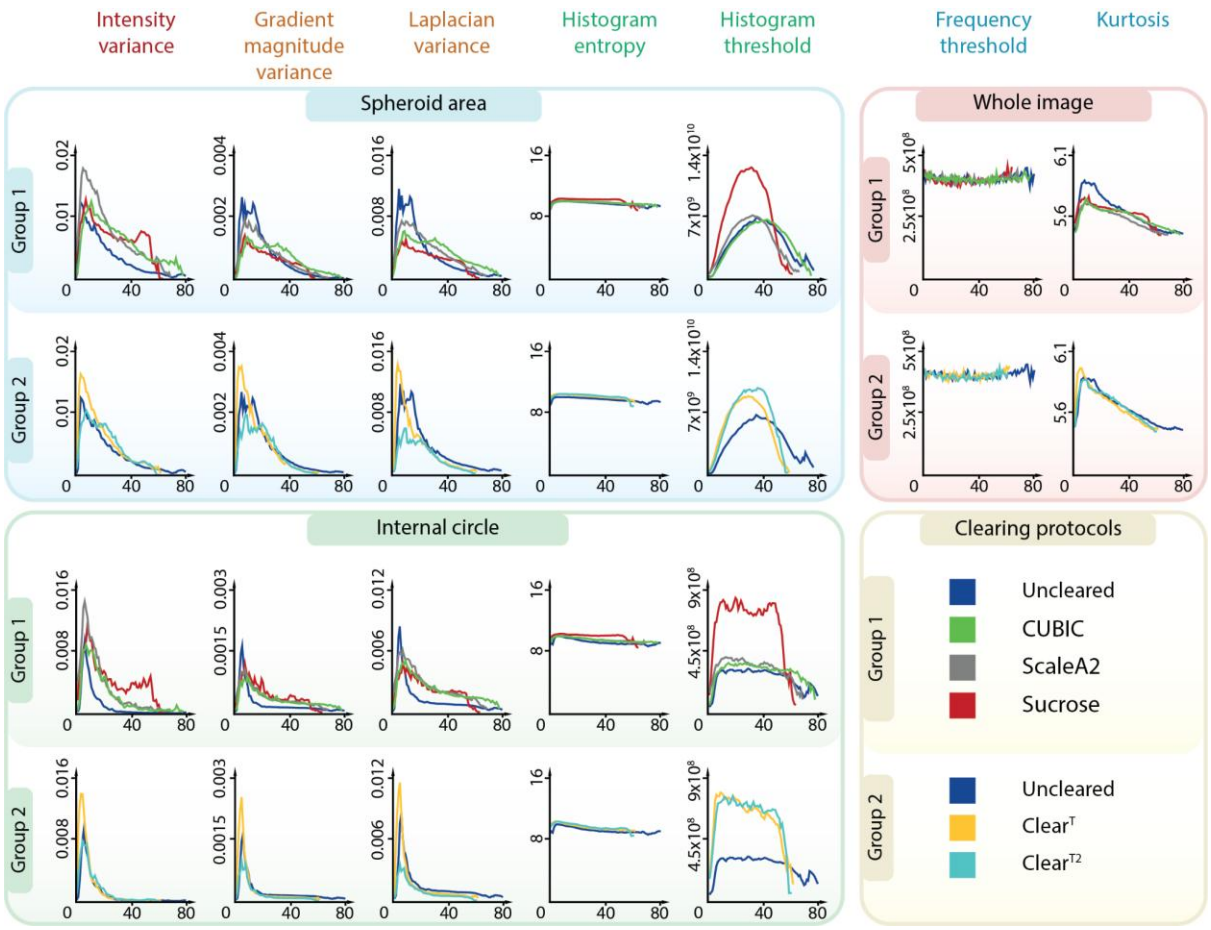

Supplementary figure 2. Demonstration of the results achieved by all 7 metrics on Huh-7D12 spheroids. All 7 metrics were used to evaluate the Huh-7D12 spheroids. Image quality was evaluated using the thresholded area of the spheroid and the internal circle options for intensity variance, gradient magnitude variance, Laplacian variance, histogram entropy, and histogram threshold metrics. The whole image was evaluated using frequency threshold and kurtosis metrics. The results for the optical clearing groups are divided into 2 groups to achieve better visibility.

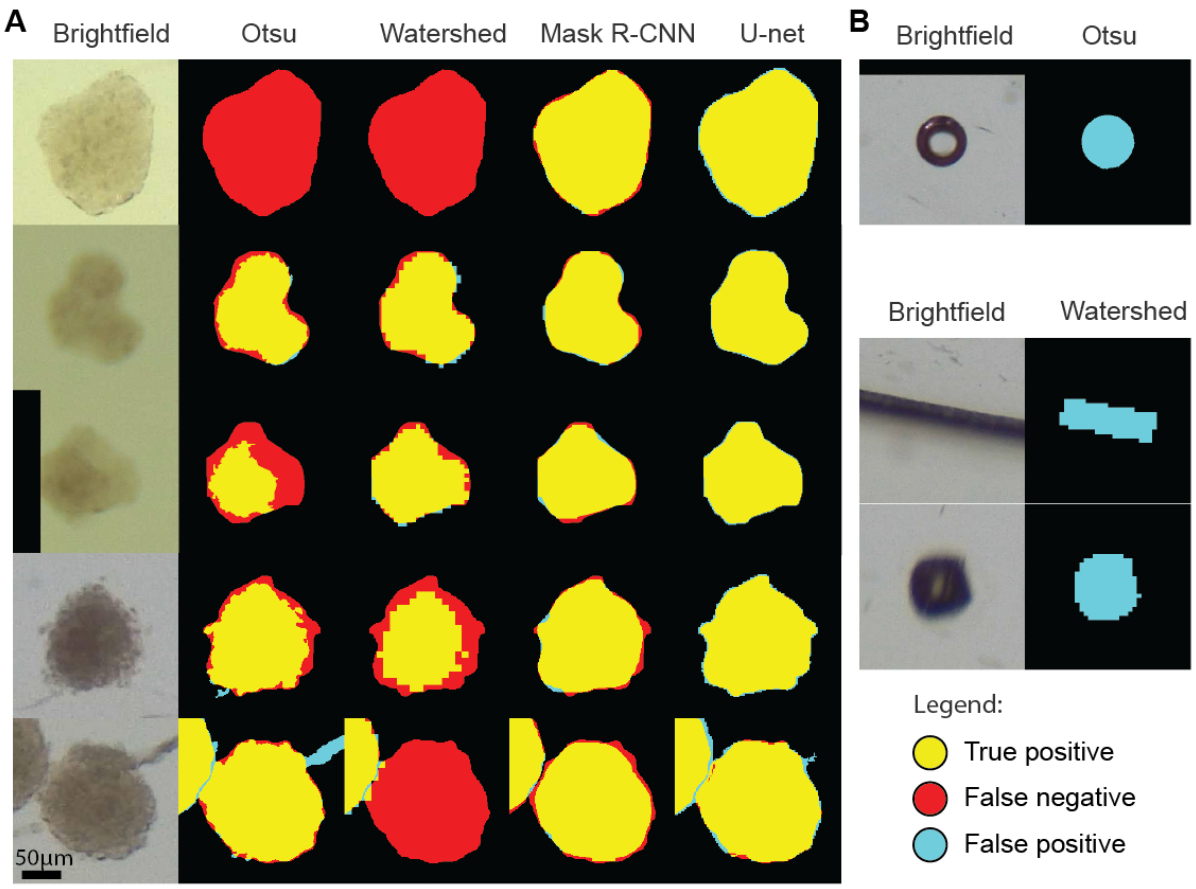

Supplementary figure 3. Qualitative comparison of segmentation methods. (a) Brightfield images of spheroids of different sizes and shapes are shown in the first column. The results of 4 distinct segmentation methods including Otsu, Watershed, Mask R-CNN, and U-Net were displayed in the following columns, respectively. Yellow colour is used to label true positive pixels, red for false negative, and cyan for false positive pixels. (b) Illustrations of Otsu thresholding and watershed algorithms' false positive cases. Scale bar represents 50 μm. The figure is adapted from [101].

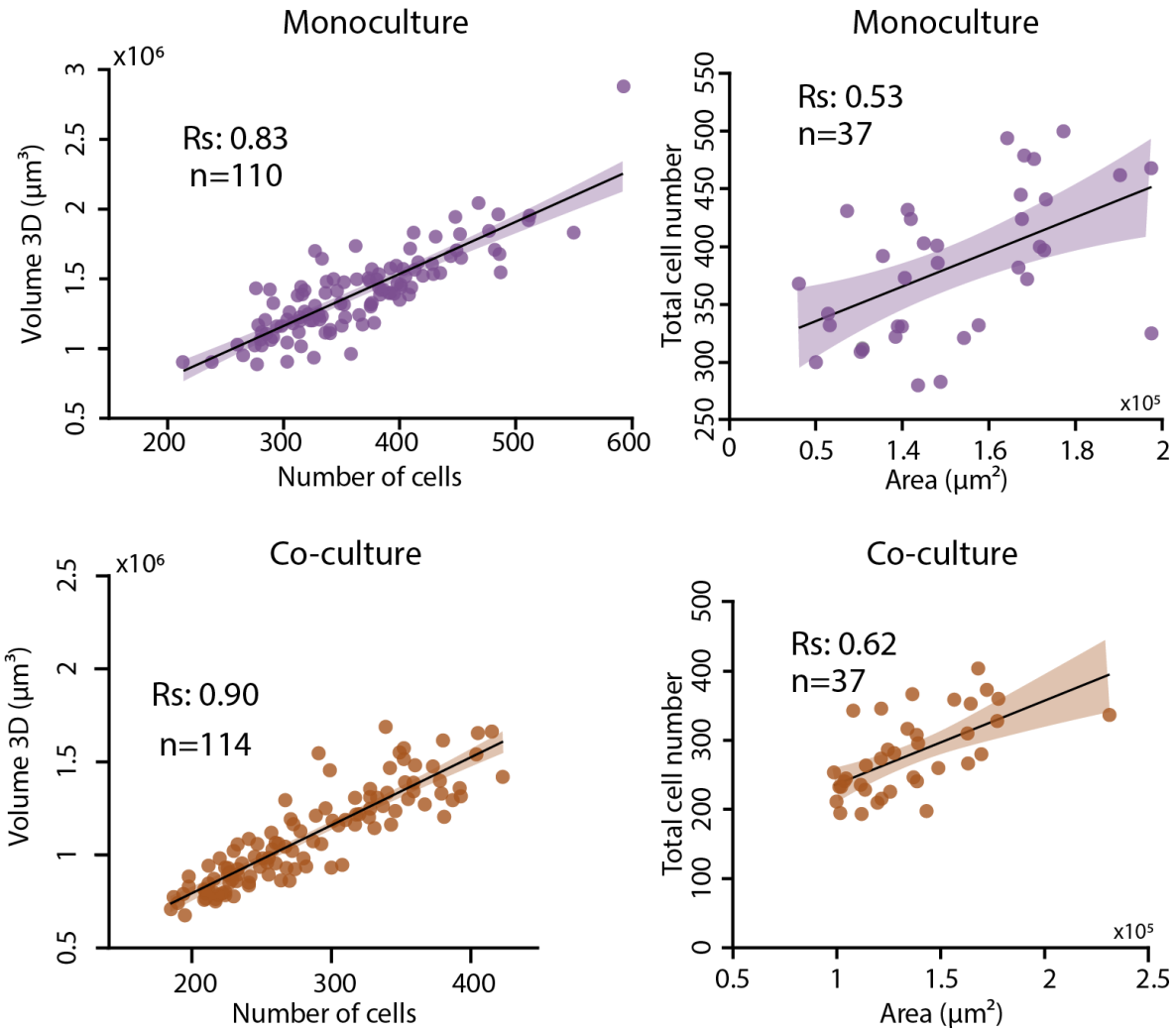

Supplementary figure 4. Correlation results of the spheroid dataset. Spearman's correlation was calculated for the Volume 3D and the number of segmented nuclei features for the whole dataset. Monoculture spheroids labelled with purple (n=110) and co-culture spheroids are labelled with orange (n=114). Only the paired spheroids (n=37) were used to calculate the Spearman's correlation between the segmented Area and the number of cells. The figure is adapted from [16].